

Advancing excited-state simulations for TADF emitters: An eXtended Tight-Binding framework for high-throughput screening and design

Jean-Pierre Tchapel Njafa*, Aissatou Maghame, Elvira Vanelle Kameni Tcheuffa, Serge Guy Nana Engo*

Dr. J-P. Tchapel Njafa

Department of Physics, Faculty of Science, University of Yaounde 1, Po. Box 812, Yaounde, Cameroon

Email Address: jean-pierre.tchapet@facsciences-uy1.cm

A. Maghame

Department of Physics, Faculty of Science, University of Yaounde 1, Po. Box 812, Yaounde, Cameroon

E. V. Kameni Tcheuffa

Department of Physics, Faculty of Science, University of Yaounde 1, Po. Box 812, Yaounde, Cameroon

Prof. S. G. Nana Engo

Department of Physics, Faculty of Science, University of Yaounde 1, Po. Box 812, Yaounde, Cameroon

Email Address: serge.nana-engo@facsciences-uy1.cm

Keywords: *TADF*, *OLED*, *xTB*, *sTDA*, *sTD-DFT*, *TD-DFT*, *UV-Vis spectra*

We present a computationally efficient framework for predicting the excited-state properties of thermally activated delayed fluorescence (TADF) emitters, integrating extended tight-binding (*xTB*), simplified Tamm-Dancoff approximation (*sTDA*), and simplified time-dependent density functional theory (*sTD-DFT*) methods. Benchmarking against Tamm-Dancoff approximation (noted full *TDA*) demonstrates that this approach accurately captures key photophysical properties, including singlet-triplet energy gaps, excitation energies, and fluorescence spectra, in both vacuum and solvent environments, while achieving over 99% reduction in computational cost. We analyze a series of representative TADF emitters, revealing a strong correlation between the torsional angle between donor and acceptor units and the solvent-induced redshift in the emission spectrum. This work highlights the potential of semi-empirical methods for high-throughput screening of TADF materials and provides valuable insights for designing next-generation optoelectronic devices. The multi-objective function is one of a kind, and it further enhances our results with an original solution. While acknowledging the limitations of semi-empirical methods for highly complex systems, we outline promising future directions, including hybrid computational approaches and integration with machine learning techniques, to further improve predictive accuracy and accelerate the discovery of advanced functional materials.

1 Introduction

The quest for sustainable, high-performance lighting has ignited intense research in thermally activated delayed fluorescence (TADF) materials, promising a route to next-generation organic light-emitting diodes (OLEDs) that circumvent the need for scarce and costly heavy-metal dopants [1, 2, 3, 4, 5]. Realizing the full potential of TADF-OLEDs hinges on precise computational modeling of their complex photophysics, particularly the accurate prediction of key excited-state properties like singlet-triplet energy gaps (ΔE_{ST}) and excited-state lifetimes [6, 7]. However, the computational cost of high-accuracy methods,

such as time-dependent density functional theory (TD-DFT) [8, 9], often becomes prohibitive for large-scale material screening and optimization, a bottleneck hindering the discovery of novel TADF emitters with tailored properties. This challenge is amplified by the well-known limitations of TD-DFT in accurately describing systems with significant charge-transfer character [7], further motivating the need for computationally efficient yet reliable alternatives. Addressing this challenge has implications for both improved technology as well as reducing computational power consumption, thus making this relevant for the Sustainable Development Goal (SDG) 13 on climate action.

This work introduces a robust and rigorously validated semi-empirical computational framework designed to strike an optimal balance between accuracy and efficiency in predicting the key photophysical properties of TADF molecules. Our approach integrates extended tight-binding (xTB) [10, 11, 12], simplified Tamm-Dancoff approximation (sTDA) [10, 13, 7], and simplified time-dependent density functional theory (sTD-DFT) [14] methods and incorporates an implicit solvent model to account for environmental effects. Uniquely, we combine these techniques to enable large-scale screening and optimization of TADF materials, often precluded by computationally expensive methods. The multi-objective approach allows us to see which are the best combinations of qualities and aspects and get data in an easier manner. The performance and reliability of this framework are evaluated via a comprehensive benchmarking study (Section 3.1) against full TDA calculations and a detailed comparison to experimental trends for a representative set of TADF emitters. Furthermore, we explore the correlations between calculated molecular properties, such as donor-acceptor separation and torsional angles (illustrated in Table 7), and observed photophysical behavior (Section 3.2). A detailed analysis of singlet-triplet energy gaps (Section 3.3), excitation energies, and oscillator strengths (Section 3.4), along with an investigation of the critical impact of solvent effects on the excited-state properties (Section 3.5), is also provided. We believe this approach provides a valuable tool for investigating TADF emitters and, more generally, for studying the interplay of electronic structure, molecular geometry, and environmental effects in photoactive molecular systems, with the ultimate goal of accelerating the design and discovery of high-performance, sustainable optoelectronic materials.

2 Computational methods

Accurately modeling the excited-state properties of TADF emitters requires a careful balance between computational efficiency and predictive accuracy, particularly when considering the challenges of solvent effects and the need for high-throughput screening. This study introduces a comprehensive computational framework that integrates semi-empirical and density functional theory-based methods to efficiently predict key photophysical properties. Our framework incorporates extended tight-binding (xTB) [10, 11, 12], simplified Tamm-Dancoff approximation (sTDA) [10, 13, 7], and simplified time-dependent density functional theory (sTD-DFT) [14, 15]. These methods were carefully selected to provide a computationally tractable and reliable approach for excited-state simulations. The workflow is specifically designed to evaluate key photophysical properties, such as singlet-triplet energy gaps (ΔE_{ST}) and fluorescence emission spectra, while incorporating solvent effects to enhance the realism of our simulations. This methodology is applied to a set of representative TADF emitters, enabling a comprehensive benchmarking of computational efficiency and predictive accuracy under both vacuum and solvated conditions. A schematic

representation of the workflow is presented in Figure 1.

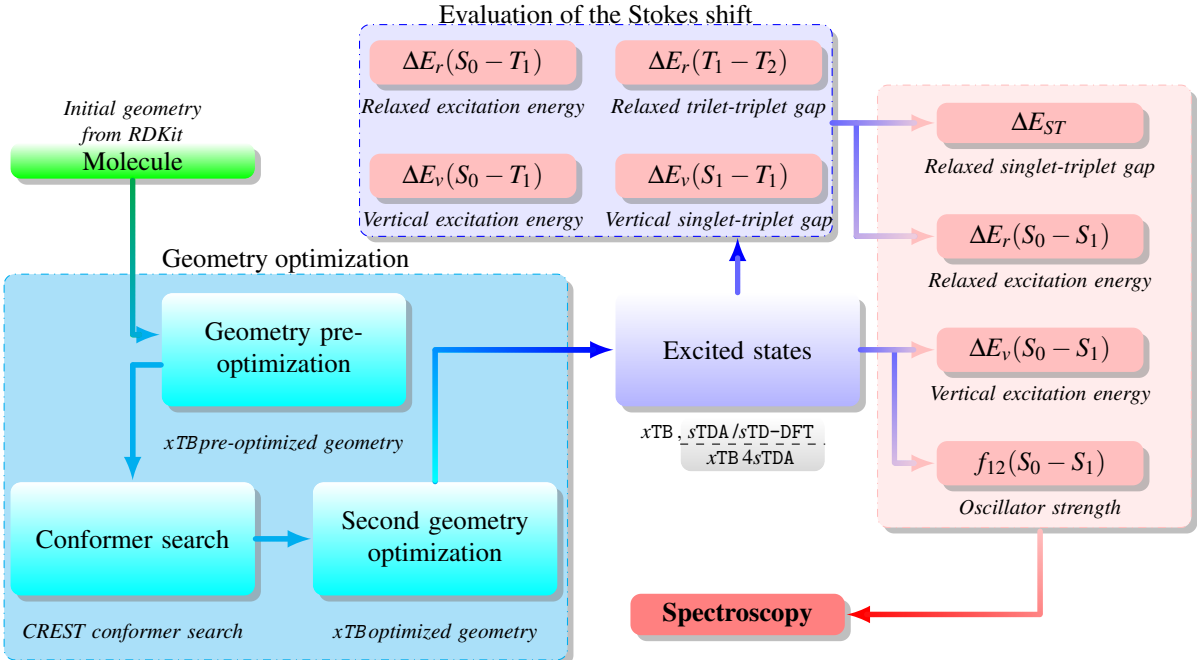


Figure 1: Overview of the simulation workflow. Starting with a SMILES string, the code performs conformer search and geometry optimisation via *xTB* for the singlet ground state S_0 and the triplet state T_1 . It allows the extraction of the relaxed triplet excitation energy. Simplified time-dependent DFT calculation with *sTDA* / *sTD-DFT* extracts the vertical singlet-triplet gap, the relaxed triplet-triplet gap, the oscillator strength, the vertical excitation energy and the fluorescence absorption and emission spectra, while incorporating solvent effects to enhance the realism of our simulations. The Stokes shift is evaluated and then allows the relaxed singlet-triplet gap to be estimated.

2.1 Molecular geometry optimization

Precise molecular geometries are paramount for reliable predictions of excited-state properties, as they directly influence key parameters like energy gaps and oscillator strengths. We employed a three-step geometry optimization process to obtain accurate geometries for both the ground state (S_0) and the first triplet state (T_1). This approach comprises:

- 1. Initial structure generation.** Initial molecular structures are generated from SMILES strings using the RDKit library (version 2024.3.1) [16]. These 2D structures are converted to 3D geometries using the MMFF94s force field [17] for a preliminary optimization. Subsequently, geometric refinement is performed using the GFNi-*xTB* semi-empirical method (with $i = 0, 1, 2$), as implemented in the *xTB* package (version 6.7.0) [18].
- 2. Conformer search.** To account for molecular flexibility and identify the most stable conformers, we performed a conformer search using the CREST program (version 3.0) [19]. The GFNi-*xTB* method (version 6.7.0 of *xTB*) [18, 12] is used for an efficient sampling of conformational space, generating an ensemble of possible geometries. The lowest-energy conformer from this ensemble is selected for subsequent calculations, reducing the risk of overlooking relevant stable conformations, that could significantly influence excited-state properties.

- Final geometry optimization.** The selected conformer(s) undergo final geometry optimization using the same GFNi-*xTB* method (version 6.7.0 of *xTB*) under both vacuum and implicit solvent conditions. Toluene is chosen as the solvent, owing to its relevance in OLED applications. An implicit solvent model, implemented within *xTB*, is employed to simulate the solvent environment. The root-mean-square deviation (RMSD) between vacuum- and solvent-optimized geometries is computed, using the module `rdkit.Chem.rdMolAlign` of RDKit [16], to quantify the structural changes induced by solvation. A convergence threshold of 10^{-7} a.u. for the energy and 2×10^{-4} a.u. for the gradient norm is applied for all optimizations. This process ensures that the obtained geometries are stable, physically meaningful, and reflective of realistic conditions.

Table S. 3 in the Supporting Information summarizes the RMSD values obtained for each molecule. Figure S. 9 shows an example (4CzIPN) of a pre-optimized geometry evolving through conformer search to the final optimization.

2.2 Excited-state property calculations

Accurate prediction of excited-state properties is critical for understanding the photophysical behavior of TADF emitters. To this end, the present study utilizes a combination of semi-empirical and density functional theory (DFT)-based methodologies, encompassing:

- xTB* 4*sTDA* implementation** (version 1.0). The *xTB* 4*sTDA* method performs ground-state calculations using the *xTB* model, followed by a simplified Tamm-Dancoff approximation (*sTDA*) and simplified Time-Dependent Density Functional Theory (*sTD-DFT*) for excited-state calculations.
- Simplified Tamm-Dancoff Approximation (*sTDA*)** (version 1.6.3 of the *sTDA* software) [10, 13, 7]. *sTDA* calculations are performed to efficiently determine the excitation energies and oscillator strengths of low-lying singlet (S_1) and triplet (T_1) states.
- Simplified Time-Dependent Density Functional Theory (*sTD-DFT*)** (version 1.6.3 of the *sTDA* software) [14]. *sTD-DFT* calculations are employed for a more refined calculation of excitation energies and oscillator strengths.
- Full TDA (for benchmarking objectives).** To benchmark the accuracy of our semi-empirical methods, full TDA (in opposition of *sTDA*) calculations are performed using the PySCF framework (version 2.7.0) [15, 20] with the B3LYP and CAM-B3LYP functionals and the def2-TZVP basis set, on a subset of representative molecules to validate the accuracy of the *sTDA* and *sTD-DFT* methods,

For each molecule, we assessed the following photophysical properties:

- Singlet-triplet energy gap (ΔE_{ST}), delineated as the energy difference between the lowest singlet (S_1) and triplet (T_1) excited states, which is a key parameter for determining TADF performance. Smaller ΔE_{ST} values facilitate enhanced reverse intersystem crossing (rISC).
- The vertical excitation energies, calculated for singlet-singlet ($S_0 \rightarrow S_1$) and singlet-triplet ($S_0 \rightarrow T_1$) transitions; the relaxed excitation energies, including singlet-triplet

($S_0 \rightarrow T_1$) and triplet-triplet ($T_1 \rightarrow T_2$) transitions, are also evaluated. These calculations aid in elucidating the electronic properties that influence absorption and emission spectra.

3. Oscillator strengths, which measure the probability of radiative transitions and provide valuable insights into fluorescence efficiency.
4. Fluorescence spectra, predicted for $S_1 \rightarrow S_0$ transitions, are used to model the emission behavior. Peak wavelengths and intensities are determined to enable comparisons with experimental trends when available. UV-Vis spectra, which provide critical insights into electronic transitions, are also evaluated (see Section S.3). Additionally, the fluorescence emission spectrum is estimated based on *Kasha's rule*, which assumes that emission primarily occurs from the lowest excited state.

All calculations are performed on the optimized molecular geometries obtained from Section 2.1. While these methods were applied to all molecules in the study, the calculations performed on the 4CzIPN molecule play a particularly important benchmarking role, since the availability of extensive experimental data for this well-characterized TADF emitter enabled a direct comparison of calculated and measured values. These comparisons provide a robust validation of the accuracy and predictive power of the sTDA and sTD-DFT methods.

Further details of these calculations and the rationale behind the selection of these specific methods are discussed in the Supporting Information.

2.3 Solvent effects

Excited-state calculations are systematically conducted under both vacuum and solvated conditions. The vacuum environment serves as a baseline for determining the intrinsic excited-state properties of each molecule. In contrast, solvation effects facilitated by toluene are incorporated through an implicit solvation model based on the analytical linearized Poisson–Boltzmann (ALPB) model, as implemented in *xTB* [21]. Toluene is selected as the solvent due to its relevance in OLED applications. The influence of solvation on both molecular geometries and excited-state properties is thoroughly investigated and analyzed. To quantify these effects, the differences between vacuum and solvation conditions are characterized using the method: $\Delta E_{\text{solv}} = |\Delta E_{\text{vacuum}} - \Delta E_{\text{toluene}}|$, which measures the absolute energy differences between the excited states in vacuum and solvated environments.

2.4 Stokes shifts and relaxed singlet-triplet excitation energies

Since *xTB* does not permit geometry optimization of molecules in the S_1 state, a direct evaluation of the relaxed singlet-triplet excitation energy, ΔE_{ST} , is not possible. However, vertical and relaxed excitation energies for the $S_0 \rightarrow T_1$ transition are computed. To estimate ΔE_{ST} , we first obtain the geometric energy relaxation for the T_1 state as the difference: $\Delta E_v(S_0 \rightarrow T_1) - \Delta E_r(S_0 \rightarrow T_1)$. Based on this value, and considering a simplified Jablonski diagram with relaxed triplet-triplet transition energies (as detailed in Figure S. 1 and Tables S. 4 and S. 5), we employed the following approximations to estimate the Stokes shifts (S_{shift}) and the relaxed singlet-triplet excitation energies (ΔE_{ST}):

- If $\Delta E_v(S_1 \leftarrow T_1) < \Delta E_r(T_2 \leftarrow T_1)$,

$$\Delta E_{ST} \approx \Delta E_v(S_1 \leftarrow T_1), \quad S_{\text{shift}} \approx \Delta E_v(S_0 \rightarrow T_1) - \Delta E_r(S_0 \rightarrow T_1);$$

- If $\Delta E_v(S_1 \leftarrow T_1) > \Delta E_r(T_2 \leftarrow T_1)$,

$$\Delta E_{ST} \approx \frac{1}{2} \Delta E_r(T_2 \leftarrow T_1), \quad S_{shift} \approx \frac{1}{2} \Delta E_r(T_2 \leftarrow T_1) + [\Delta E_v(S_0 \rightarrow T_1) - \Delta E_r(S_0 \rightarrow T_1)].$$

The analysis of fluorescence spectra, which incorporates solvent effects, shows how the solvent modulates emission characteristics. Each molecule’s spectrum is presented through two distinct plots: a UV-Vis absorption spectrum and a fluorescence spectrum which incorporates the Stokes shift. In these plots, findings from *sTDA* are shown using green and magenta lines for vacuum and toluene, respectively, while results from *sTD-DFT* calculations are shown using blue and red lines for the corresponding environments. The spectral data are derived using Multiwfn (version 3.8(dev)) [22], a comprehensive tool popular for its ability to analyze electronic transitions. Multiwfn provides a wide range of state function analysis techniques and it is recognized for its operational efficiency, ease of use, and flexibility. To ensure precise spectral characterization, a Full Width at Half Maximum (FWHM) of 0.15 eV, is utilized.

2.5 Computational details

All calculations were performed using specific computational resources, the details of which, along with information on parallelization and timings, are provided in the Supporting Information.

3 Results and discussion

This section presents the results of our computational study on selected Thermally Activated Delayed Fluorescence (TADF) emitters. We begin by benchmarking the accuracy and efficiency of the employed semi-empirical methods against full TDA calculations using the B3LYP and CAM-B3LYP functionals and the def2-TZVP basis set. We focused on the well-characterized 4CzIPN molecule as documented in experimental studies [23, 24], and assessed the performance of the semi-empirical methods by comparing singlet and triplet excitation energies, as well as oscillator strengths. Having validated our computational approach using metrics such as absolute energy differences and root mean square error, we now turn our attention to the photophysical properties of the selected TADF molecules. We will analyze key properties including singlet-triplet splitting (ΔE_{ST}), oscillator strengths, and charge transfer character of the excited states to establish correlations between the molecular structure, the nature of the donor moiety, and photophysical behavior. We define the donor type in terms of the electron-donating ability of the substituted groups. Finally, we discuss the broader implications of our findings for computational material design, particularly regarding its potential to reduce the time and cost associated with the discovery of novel TADF emitters, and to create more fundamental design rules for efficient TADF emitters.

3.1 Benchmarking computational methods

To evaluate the reliability of the semi-empirical methods used in this study, we benchmarked the results (see the Tables 1 to 4 and the Figures 2 to 8) of simplified Tamm-Dancoff approximation (*sTDA*) and simplified time-dependent density functional theory (*sTD-DFT*) against full Tamm-Dancoff Approximation (TDA) calculations, using the B3LYP

3.1 Benchmarking computational methods

Table 1: Calculated photophysical properties of TADF emitters in vacuum. Energies are given in eV, wavelengths in nm, and radiative lifetimes in ns. Results are shown for both the semi-empirical x TB method, and the Tamm-Dancoff Approximation (TDA) and Time Dependent Density Functional Theory (TD-DFT) within a simplified scheme (s TDA and s TD-DFT, respectively).

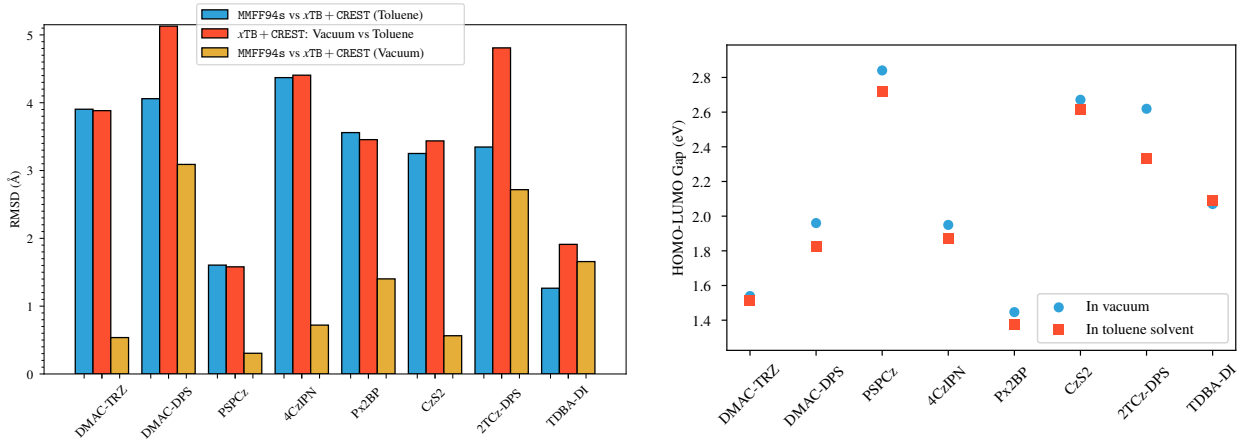
Molecule	DMAC-TRZ	DMAC-DPS	PSPCz	4CzIPN	Px2BP	CzS2	2TCz-DPS	TDBA-DI
HOMO-LUMO gap	1.539	1.960	2.840	1.950	1.447	2.671	2.619	2.070
$\Delta E_r(S_0 \rightarrow T_1)$	2.090	2.579	3.113	2.268	2.033	2.688	2.459	2.558
$\Delta E_v(S_0 \rightarrow T_1)$ (s TDA)	3.386	3.471	3.399	3.086	2.573	3.435	3.413	3.092
$\Delta E_v(S_0 \rightarrow T_1)$ (s TD-DFT)	3.373	3.441	3.376	3.077	2.563	3.412	3.391	3.073
$\Delta E_v(S_0 \rightarrow S_1)$ (s TDA)	3.483	3.878	3.849	3.298	2.911	3.902	3.874	3.573
$\Delta E_v(S_0 \rightarrow S_1)$ (s TD-DFT)	3.476	3.873	3.777	3.268	2.879	3.839	3.809	3.502
$\Delta E_v(S_1 \leftarrow T_1)$ (s TDA)	0.097	0.407	0.450	0.212	0.338	0.467	0.461	0.481
$\Delta E_v(S_1 \leftarrow T_1)$ (s TD-DFT)	0.103	0.432	0.401	0.191	0.316	0.427	0.418	0.429
S_{shift} (s TDA)	1.296	1.055	1.012	0.818	0.540	0.788	1.032	0.534
S_{shift} (s TD-DFT)	1.283	1.025	0.934	0.809	0.530	0.751	0.990	0.515
$\Delta E_r(S_0 \rightarrow S_1)$ (s TDA)	2.187	2.742	3.233	2.480	2.371	2.728	2.537	3.039
$\Delta E_r(S_0 \rightarrow S_1)$ (s TD-DFT)	2.138	2.625	3.215	2.403	2.262	2.846	2.787	2.979
ΔE_{ST} (s TDA)	0.097	0.163	0.120	0.212	0.338	0.041	0.078	0.481
ΔE_{ST} (s TD-DFT)	0.103	0.163	0.072	0.191	0.316	0.027	0.058	0.429
λ_{abs} (s TDA)	356.010	319.690	322.083	375.928	425.926	317.712	320.070	347.012
λ_{abs} (s TD-DFT)	356.681	320.143	328.303	379.335	430.677	322.929	325.530	354.057
λ_{PL} (s TDA)	566.890	452.233	383.543	499.966	522.944	454.445	488.800	407.965
λ_{PL} (s TD-DFT)	565.339	452.233	389.324	504.236	527.842	456.789	492.685	415.067
$f_{12}(S_0 \rightarrow S_1)$ (s TDA)	0.146	0.021	0.189	0.152	0.103	0.351	0.151	0.194
$f_{12}(S_0 \rightarrow S_1)$ (s TD-DFT)	0.140	0.019	0.159	0.137	0.086	0.309	0.131	0.219
τ (s TDA)	33.045	148.121	11.675	24.590	39.689	8.816	23.659	12.855
τ (s TD-DFT)	36.016	174.136	14.012	29.115	52.684	9.191	22.720	11.853
MOF (s TDA)	-0.964	-0.600	0.036	-0.780	-1.064	-0.161	-0.590	-0.448
MOF (s TD-DFT)	-1.025	-0.718	0.072	-0.851	-1.169	-0.071	-0.340	-0.431

Table 2: Calculated photophysical properties of TADF emitters in toluene solvent. Energies are given in eV, wavelengths in nm, and radiative lifetimes in ns. Results are shown for both the semi-empirical x TB method, and the Tamm-Dancoff Approximation (TDA) and Time Dependent Density Functional Theory (TD-DFT) within a simplified scheme (s TDA and s TD-DFT, respectively).

Molecule	DMAC-TRZ	DMAC-DPS	PSPCz	4CzIPN	Px2BP	CzS2	2TCz-DPS	TDBA-DI
HOMO-LUMO gap	1.512	1.822	2.719	1.871	1.373	2.615	2.333	2.090
$\Delta E_r(S_0 \rightarrow T_1)$	2.058	2.383	3.081	2.186	1.942	2.614	2.322	2.552
$\Delta E_v(S_0 \rightarrow T_1)$ (s TDA)	3.377	3.471	3.413	3.026	2.661	3.450	3.425	3.106
$\Delta E_v(S_0 \rightarrow T_1)$ (s TD-DFT)	3.345	3.441	3.390	3.016	2.650	3.428	3.404	3.087
$\Delta E_v(S_0 \rightarrow S_1)$ (s TDA)	3.457	3.713	3.859	3.243	2.981	3.918	3.890	3.564
$\Delta E_v(S_0 \rightarrow S_1)$ (s TD-DFT)	3.453	3.708	3.789	3.214	2.952	3.858	3.831	3.508
$\Delta E_v(S_1 \leftarrow T_1)$ (s TDA)	0.080	0.242	0.446	0.217	0.320	0.468	0.465	0.458
$\Delta E_v(S_1 \leftarrow T_1)$ (s TD-DFT)	0.108	0.267	0.399	0.198	0.302	0.430	0.427	0.421
S_{shift} (s TDA)	1.319	1.088	0.466	0.840	0.719	1.069	1.103	0.554
S_{shift} (s TD-DFT)	1.287	1.058	0.443	0.830	0.708	0.948	1.279	0.535
$\Delta E_r(S_0 \rightarrow S_1)$ (s TDA)	2.193	2.742	3.185	2.459	2.349	2.714	2.517	2.987
$\Delta E_r(S_0 \rightarrow S_1)$ (s TD-DFT)	2.166	2.650	3.215	2.384	2.244	2.748	2.518	2.973
ΔE_{ST} (s TDA)	0.080	0.242	0.134	0.217	0.320	0.233	0.465	0.458
ΔE_{ST} (s TD-DFT)	0.108	0.267	0.134	0.198	0.302	0.134	0.197	0.421
λ_{abs} (s TDA)	358.669	333.937	321.259	382.365	415.887	316.409	318.690	347.929
λ_{abs} (s TD-DFT)	359.072	334.417	327.264	385.715	419.976	321.394	323.676	353.446
λ_{PL} (s TDA)	579.934	472.241	385.613	515.994	548.141	435.592	444.877	416.201
λ_{PL} (s TD-DFT)	572.436	467.787	385.613	520.106	552.538	451.207	492.308	417.041
$f_{12}(S_0 \rightarrow S_1)$ (s TDA)	0.066	0.034	0.212	0.138	0.100	0.389	0.156	0.011
$f_{12}(S_0 \rightarrow S_1)$ (s TD-DFT)	0.064	0.033	0.178	0.125	0.084	0.340	0.149	0.221
τ (s TDA)	73.043	91.526	10.714	27.722	41.771	8.042	23.268	243.665
τ (s TD-DFT)	77.243	99.113	12.517	32.496	54.619	8.980	24.305	11.809
MOF (s TDA)	-1.021	-0.667	0.063	-0.821	-1.071	-0.329	-0.992	-0.660
MOF (s TD-DFT)	-1.078	-0.783	0.029	-0.889	-1.174	-0.246	-0.729	-0.427

and CAM-B3LYP functionals and the def2-TZVP basis set, for a subset of TADF emitters. The key excited-state properties compared include the singlet-triplet energy gap (ΔE_{ST}), vertical and relaxed excitation energies, and oscillator strengths. These properties are critical for understanding and optimizing the performance of TADF materials in OLED applications. MOF= $+f_{12} - \Delta E_{ST} - |\Delta E_r(S_0 \rightarrow S_1) - 3.2 \text{ eV}|$ stands for multi-objective function introduced by [25]. This function assigns a numerical score based on the oscillator strength (f_{12}), the relaxed singlet-triplet energy gap (ΔE_{ST}), and the relaxed singlet-singlet transi-

3.1 Benchmarking computational methods



(a) Root Mean Square Deviation (RMSD) of molecular geometries.

(b) HOMO-LUMO gap.

Figure 2: Solvent effects on molecular geometry and electronic structure. Panel (a) shows the RMSD between geometries optimized in vacuum and in toluene, indicating the solvent-induced changes in molecular structure. Panel (b) illustrates the HOMO-LUMO gap of the molecules in both environments, showcasing the stabilizing effect of toluene on their electronic properties.

tion energy ($\Delta E_r(S_0 \rightarrow S_1)$), seeking to balance the desirable properties of high f_{12} and low ΔE_{ST} for efficient TADF emitters.

3.1.1 Singlet-triplet energy gap (ΔE_{ST})

The ΔE_{ST} values computed by *sTDA*, *sTD-DFT*, and full TDA (using vertical energies) exhibit consistent trends across the test set (see Tables 1 and 2 and fig. 5). On average, *sTDA* shows a mean absolute error (MAE) of 0.135 eV and a root-mean-square error (RMSE) of 0.107 eV compared to full TDA, while *sTD-DFT* yields an MAE of 0.139 eV and an RMSE of 0.109 eV. These deviations are within the acceptable range for TADF emitter design, where ΔE_{ST} values below 0.3 eV are generally sufficient to facilitate reverse intersystem crossing (rISC).

3.1.2 Vertical excitation energies

For singlet-singlet ($S_0 \rightarrow S_1$) and singlet-triplet ($S_0 \rightarrow T_1$) transitions, both *sTDA* and *sTD-DFT* do not accurately reproduce the trends from full TDA calculations (see Figure 6), although *sTD-DFT* shows slightly improved accuracy. Compared to full TDA results, the mean absolute error (MAE) for $S_0 \rightarrow S_1$ excitation energies is 0.751 eV for *sTDA* and 0.728 eV for *sTD-DFT* in vacuum. In toluene solvent, the MAE is respectively 0.706 eV and 0.682 eV. For $S_0 \rightarrow T_1$, *sTDA* and *sTD-DFT* predictions deviate by more than 0.5 eV. These differences likely arise from the approximations in the semi-empirical methods used to calculate the vertical excitation energies, specifically regarding the excited-state wave function. Nevertheless, things are different in the case of relaxed energies as mentioned in Section 3.1.3.

3.1.3 Relaxed excitation energies

For singlet-singlet ($S_0 \rightarrow S_1$) and singlet-triplet ($S_0 \rightarrow T_1$) transitions, both *sTDA* and *sTD-DFT* reliably reproduce the full TDA trends (see Figure 7), with *sTD-DFT* showing slightly

3.1 Benchmarking computational methods

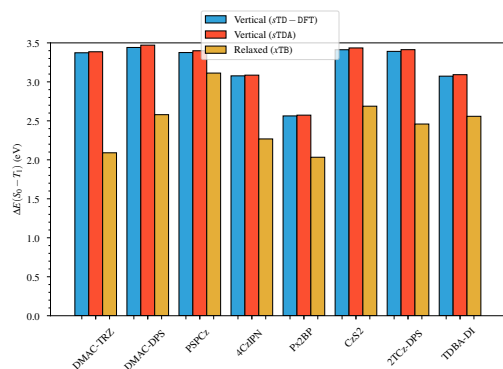
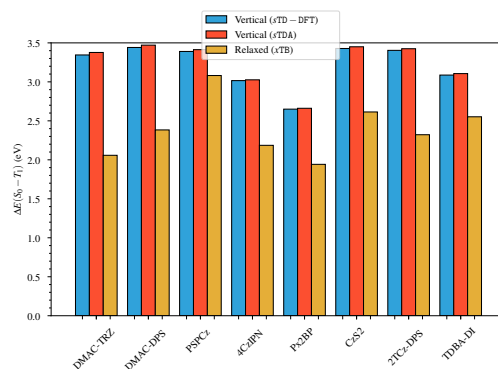
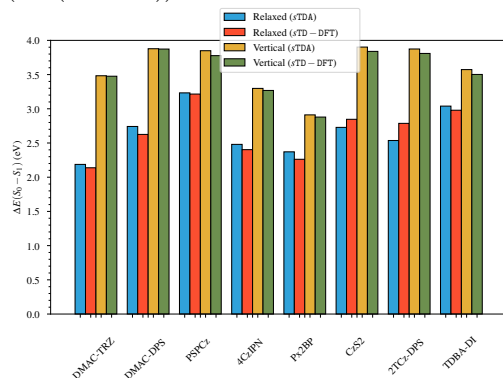
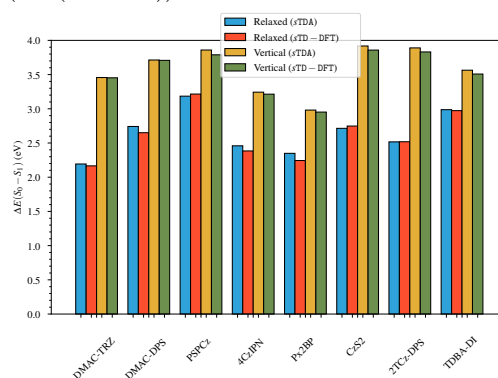
(a) Singlet-Triplet transition energies ($\Delta E(S_0 \rightarrow T_1)$) in vacuum.(b) Singlet-Triplet transition energies ($\Delta E(S_0 \rightarrow T_1)$) in toluene solvent.(c) Singlet-Singlet transition energies ($\Delta E(S_0 \rightarrow S_1)$) in vacuum.(d) Singlet-Singlet transition energies ($\Delta E(S_0 \rightarrow S_1)$) in toluene solvent.

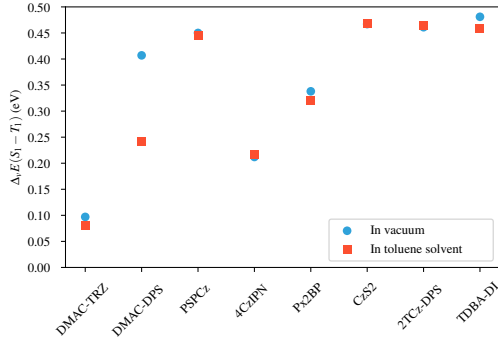
Figure 3: Comparison of calculated singlet-triplet ($S_0 \rightarrow T_1$) and singlet-singlet ($S_0 \rightarrow S_1$) transition energies using different methods (xTB, simplified Tamm-Dancoff Approximation (sTDA), and simplified Time-Dependent Density Functional Theory (sTD-DFT)) in vacuum and toluene solvent. The figure highlights the effect of the computational method and solvation on the calculated transition energies.

improved accuracy. The mean absolute error (MAE) for $S_0 \rightarrow S_1$ excitation energies is 0.381 eV for sTDA and 0.356 eV for sTD-DFT, compared to the full TDA results. For $S_0 \rightarrow T_1$, predictions using relaxed energies deviate from TDA by an average of 0.304 eV. The geometry optimization was performed at the xTB level of theory before the relaxed energies calculation. These results highlight the importance of using relaxed energies for capturing more appropriate photophysical transitions compared to those calculated from the ground state geometry.

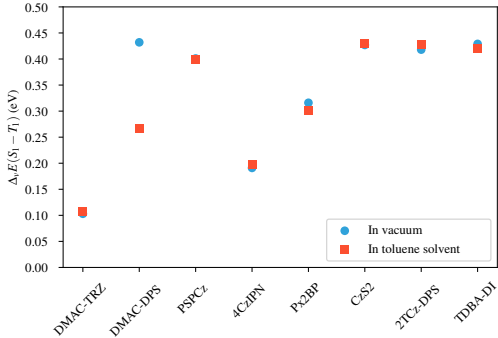
3.1.4 Oscillator strengths

The computed oscillator strengths, which reflect the intensity of radiative transitions, show minor deviations between methods. The relative trends between molecules are preserved across all three approaches, with sTD-DFT providing the closest match to full TDA values. The differences observed (MAE \leq 0.09) are unlikely to impact practical interpretations of fluorescence efficiency.

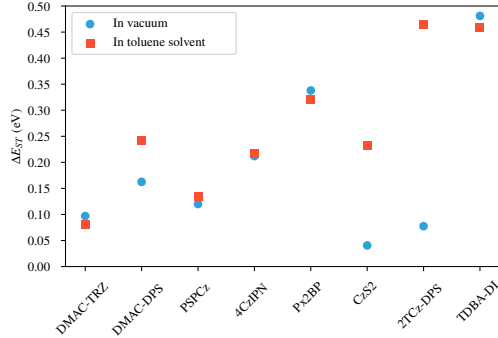
3.1 Benchmarking computational methods



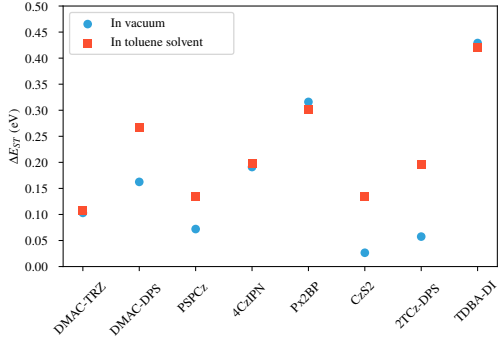
(a) Vertical excitation energies calculated with sTDA.



(b) Vertical excitation energies calculated with sTD-DFT.



(c) Relaxed excitation energies calculated with sTDA.



(d) Relaxed excitation energies calculated with sTD-DFT.

Figure 4: Comparison of vertical and relaxed excitation energies for the $S_1 \leftarrow T_1$ transition. The $\Delta E_v(S_1 \leftarrow T_1)$ and ΔE_{ST} values for the chosen TADF molecules are shown for both the simplified Tamm-Dancoff Approximation (sTDA) and simplified Time-Dependent Density Functional Theory (sTD-DFT) methods. Both vacuum and toluene solvent conditions are presented. Note that vertical energies refer to transitions from the ground state geometry, while relaxed energies refer to transition between the lowest-energy triplet and singlet excited states. The ΔE_{ST} is a key parameter influencing the efficiency of reverse intersystem crossing (rISC) in TADF materials.

3.1.5 Multi-objective function

The multi-objective function (MOF) [25] is employed to quantify how well a proposed molecule meets our design goals for TADF emitters. It simultaneously optimizes several key parameters: (1) a small singlet-triplet energy gap (ΔE_{ST}) to promote efficient reverse intersystem crossing (rISC); (2) a high oscillator strength (f_{12}) for the $S_0 \rightarrow S_1$ transition to ensure strong radiative emission; (3) a targeted $S_0 \rightarrow S_1$ excitation energy (E_{S1}) to achieve the desired emission wavelength (color tunability); and (4) a low computational cost to enable high-throughput screening.

By assigning a numerical score based on these factors, the MOF allows for easy comparison between different molecules. In this section, the MOF serves as a benchmark to evaluate the accuracy and efficiency of the simplified sTDA and sTD-DFT methods by comparing their results to those obtained with the full TDA method. Specifically, this scoring system helps identify which method reproduces the same molecular properties as predicted by the full TDA method, which serves as our benchmark for accuracy. This section is not focused on the absolute MOF values, but rather on the relative performance of the computational methods in replicating the TDA results.

3.1 Benchmarking computational methods

Table 3: Comparison of calculated excited-state properties and computational times for TADF emitters in vacuum. Energies are reported in eV and computation times in s. The table presents results from full TDA, simplified TDA (*sTDA*), and simplified TD-DFT (*sTD-DFT*) methods. Mean absolute error (MAE) and root mean square error (RMSE) are calculated by comparison with the full TDA results. 't' represents the computation time for each method.

Molecule	DMAC-TRZ	DMAC-DPS	PSPCz	4CzIPN	Px2BP	CzS2	2TCz-DPS	TDBA-DI	MAE	RMSE
$\Delta E_v(S_1 \leftarrow T_1) \sim \Delta E_{ST}$ (TDA)	0.081	0.069	0.257	0.187	0.147	0.317	0.238	1.185	-	-
ΔE_{ST} (<i>sTDA</i>)	0.097	0.163	0.120	0.212	0.338	0.041	0.077	0.481	0.145	0.113
ΔE_{ST} (<i>sTD-DFT</i>)	0.103	0.163	0.072	0.191	0.316	0.026	0.058	0.429	0.154	0.118
$\Delta E_v(S_1 \leftarrow T_1)$ (<i>sTDA</i>)	0.097	0.407	0.450	0.212	0.338	0.467	0.461	0.481	0.135	0.142
$\Delta E_v(S_1 \leftarrow T_1)$ (<i>sTD-DFT</i>)	0.103	0.432	0.401	0.191	0.316	0.427	0.418	0.429	0.119	0.124
$\Delta E_v(S_0 \rightarrow S_1)$ (TDA)	2.479	2.546	3.661	2.678	2.401	3.489	2.934	1.597	-	-
$\Delta E_v(S_0 \rightarrow S_1)$ (<i>sTDA</i>)	3.483	3.878	3.849	3.298	2.911	3.902	3.874	3.573	0.751	0.626
$\Delta E_v(S_0 \rightarrow S_1)$ (<i>sTD-DFT</i>)	3.476	3.873	3.777	3.268	2.879	3.839	3.809	3.502	0.728	0.592
$\Delta E_v(S_0 \rightarrow T_1)$ (TDA)	2.398	2.477	3.404	2.491	2.254	3.172	2.696	0.413	-	-
$\Delta E_v(S_0 \rightarrow T_1)$ (<i>sTDA</i>)	3.386	3.471	3.399	3.086	2.573	3.435	3.413	3.092	0.613	0.485
$\Delta E_v(S_0 \rightarrow T_1)$ (<i>sTD-DFT</i>)	3.373	3.441	3.376	3.077	2.563	3.412	3.391	3.073	0.598	0.475
$\Delta E_r(S_0 \rightarrow S_1)$ (<i>sTDA</i>)	2.187	2.742	3.233	2.480	2.371	2.728	2.537	3.039	0.368	0.288
$\Delta E_r(S_0 \rightarrow S_1)$ (<i>sTD-DFT</i>)	2.138	2.625	3.215	2.403	2.262	2.846	2.787	2.979	0.326	0.259
$\Delta E_r(S_0 \rightarrow T_1)$	2.090	2.579	3.113	2.268	2.033	2.688	2.459	2.558	0.269	0.233
f_{12} (TDA)	0.074	0.021	0.026	0.064	0.215	0.366	0.061	0.023	-	-
f_{12} (<i>sTDA</i>)	0.146	0.021	0.189	0.152	0.103	0.351	0.151	0.194	0.087	0.068
f_{12} (<i>sTD-DFT</i>)	0.140	0.019	0.159	0.137	0.086	0.309	0.131	0.219	0.081	0.066
MOF (TDA)	-0.729	-0.701	-0.692	-0.645	-0.731	-0.240	-0.443	-2.765	-	-
MOF (<i>sTDA</i>)	-0.964	-0.600	0.036	-0.780	-1.064	-0.161	-0.590	-0.448	0.307	0.220
MOF (<i>sTD-DFT</i>)	-1.025	-0.718	0.072	-0.851	-1.169	-0.071	-0.340	-0.431	0.344	0.249
t (TDA)	39153.007	71422.600	10799.822	107266.372	29068.778	23497.945	100249.382	124363.604	-	-
t (<i>sTDA</i>)	7.238	25.811	8.149	40.449	8.226	10.301	20.095	28.707	-	-
t (<i>sTD-DFT</i>)	42.847	87.329	19.707	208.962	40.692	40.074	59.932	98.676	-	-

For the *sTDA* method, the average mean absolute error (MAE) in the MOF value, compared to TDA, is 0.343, and the average root-mean-square error (RMSE) is 0.250. The average mean absolute error (MAE) for the *sTD-DFT* method is 0.356, and the average root-mean-square error (RMSE) is 0.261. These results suggest that both *sTDA* and *sTD-DFT* provide reasonably accurate approximations of the full TDA method, with *sTDA* exhibiting slightly lower errors overall.

3.1.6 Computational cost

A key advantage of semi-empirical methods is their computational efficiency. *sTDA* and *sTD-DFT* required an average of 20.705 s and 43.651 s per molecule, respectively, compared to an average of over 15 hours (or 54 000 s) for full TDA, when using single-core CPU calculations. These times refer to the single point calculations with the optimized geometry. The geometry optimization with *xTB* required much less time. This represents a runtime reduction of approximately 3-4 orders of magnitude, making *sTDA* and *sTD-DFT* considerably faster than full TDA calculations. This substantial reduction in runtime enables the large-scale screening of TADF emitters without sacrificing predictive reliability.

These benchmarks demonstrate that *sTDA* and *sTD-DFT* are effective for predicting the pho-

3.2 Molecular properties

Table 4: Comparison of calculated excited-state properties and computational times for TADF emitters in toluene solvent. Energies are reported in eV and computation times in s. The table presents results from full TDA, simplified TDA (*sTDA*), and simplified TD-DFT (*sTD-DFT*) methods. Mean absolute error (MAE) and root mean square error (RMSE) are calculated by comparison with the full TDA results. 't' represents the computation time for each method.

Molecule	DMAC-TRZ	DMAC-DPS	PSPCz	4CzIPN	Px2BP	CzS2	2TCz-DPS	TDBA-DI	MAE	RMSE
$\Delta E_v(S_1 \leftarrow T_1) \sim \Delta E_{ST}$ (TDA)	0.064	0.078	0.271	0.193	0.150	0.325	0.269	0.281	-	-
ΔE_{ST} (<i>sTDA</i>)	0.080	0.242	0.134	0.217	0.320	0.233	0.465	0.458	0.124	0.100
ΔE_{ST} (<i>sTD-DFT</i>)	0.108	0.267	0.134	0.198	0.302	0.134	0.197	0.421	0.123	0.099
$\Delta E_v(S_1 \leftarrow T_1)$ (<i>sTDA</i>)	0.080	0.242	0.446	0.217	0.320	0.468	0.465	0.458	0.135	0.111
$\Delta E_v(S_1 \leftarrow T_1)$ (<i>sTD-DFT</i>)	0.108	0.267	0.399	0.198	0.302	0.430	0.427	0.421	0.119	0.098
$\Delta E_v(S_0 \rightarrow S_1)$ (TDA)	2.509	2.575	3.700	2.671	2.448	3.515	2.895	2.582	-	-
$\Delta E_v(S_0 \rightarrow S_1)$ (<i>sTDA</i>)	3.457	3.713	3.859	3.243	2.981	3.918	3.890	3.564	0.706	0.593
$\Delta E_v(S_0 \rightarrow S_1)$ (<i>sTD-DFT</i>)	3.453	3.708	3.789	3.214	2.952	3.858	3.831	3.508	0.682	0.561
$\Delta E_v(S_0 \rightarrow T_1)$ (TDA)	2.445	2.497	3.429	2.478	2.299	3.189	2.626	2.301	-	-
$\Delta E_v(S_0 \rightarrow T_1)$ (<i>sTDA</i>)	3.377	3.471	3.413	3.026	2.661	3.450	3.425	3.106	0.608	0.487
$\Delta E_v(S_0 \rightarrow T_1)$ (<i>sTD-DFT</i>)	3.345	3.441	3.390	3.016	2.650	3.428	3.404	3.087	0.589	0.474
$\Delta E_r(S_0 \rightarrow S_1)$ (<i>sTDA</i>)	2.193	2.742	3.185	2.459	2.349	2.714	2.517	2.987	0.393	0.311
$\Delta E_r(S_0 \rightarrow S_1)$ (<i>sTD-DFT</i>)	2.166	2.650	3.215	2.384	2.244	2.748	2.518	2.973	0.389	0.317
$\Delta E_r(S_0 \rightarrow T_1)$	2.058	2.383	3.081	2.186	1.942	2.614	2.322	2.552	0.339	0.297
$f_{12}(S_0 \rightarrow S_1)$ (TDA)	0.056	0.024	0.027	0.067	0.219	0.387	0.041	0.010	-	-
$f_{12}(S_0 \rightarrow S_1)$ (<i>sTDA</i>)	0.066	0.034	0.212	0.138	0.100	0.389	0.156	0.011	0.092	0.064
$f_{12}(S_0 \rightarrow S_1)$ (<i>sTD-DFT</i>)	0.064	0.033	0.178	0.125	0.084	0.340	0.149	0.221	0.086	0.065
MOF (TDA)	-0.699	-0.679	-0.744	-0.654	-0.682	-0.253	-0.533	-0.889	-	-
MOF (<i>sTDA</i>)	-1.021	-0.667	0.063	-0.821	-1.071	-0.329	-0.992	-0.660	0.379	0.279
MOF (<i>sTD-DFT</i>)	-1.078	-0.783	0.029	-0.889	-1.174	-0.246	-0.729	-0.427	0.369	0.273
t (TDA)	25808.543	43183.527	6735.599	69263.481	21527.554	20657.614	91689.638	75083.643	-	-
t (<i>sTDA</i>)	9.632	15.789	6.532	32.071	10.949	7.408	54.402	45.517	-	-
t (<i>sTD-DFT</i>)	37.151	90.607	24.684	170.211	39.369	29.184	87.140	101.857	-	-

tophysical properties of TADF emitters, providing a reliable compromise between computational efficiency and accuracy. The observed deviations from full TDA, which are generally below 0.4 eV for transition energies and above 0.1 for oscillator strengths, are within acceptable limits for practical applications, making these methods suitable for large-scale TADF material design. These deviations have a minimal effect on the relative trends and general conclusions of the study.

3.2 Molecular properties

The molecular properties of TADF emitters, particularly their donor-acceptor interactions, electronic distributions, and geometrical features, critically influence their excited-state behavior and, consequently, their TADF performance. This section explores how these intrinsic properties correlate with key photophysical characteristics such as singlet-triplet energy gaps (ΔE_{ST}), excitation energies, and fluorescence efficiency. Relevant properties for the studied molecules are summarized in Table 5 and Table 6. The chemical structures of the donor and acceptor units in Table 6 dictate the charge-transfer character of the molecules. Stronger electron-donating groups and electron-withdrawing groups will enhance charge

3.2 Molecular properties

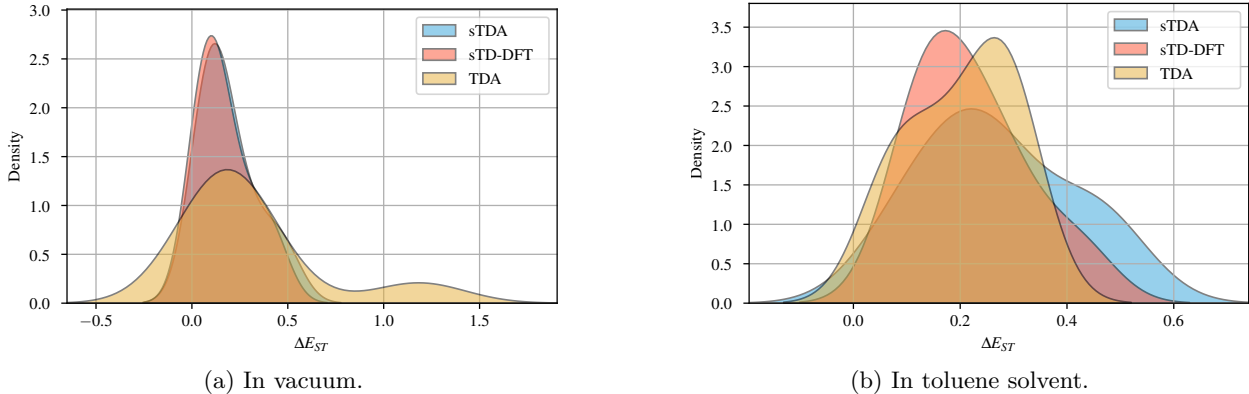


Figure 5: Comparison of the singlet-triplet energy gap (ΔE_{ST}) calculated using simplified Tamm-Dancoff Approximation ($sTDA$) and simplified Time-Dependent Density Functional Theory ($sTD-DFT$) methods, against full Tamm-Dancoff Approximation (TDA) as a benchmark. Panels (a) and (b) show the results in vacuum and toluene solvent, respectively. The kernel density estimation plots show that $sTDA$ and $sTD-DFT$ exhibit similar distributions, but they differ from the benchmark full TDA results, indicating that these methods do not fully reproduce the range of ΔE_{ST} values.

Table 5: Summary of key molecular properties relevant to TADF emission, calculated in vacuum and toluene solvent. Energies are reported in eV, and centroid distances are reported in Å. The HOMO-LUMO absolute spatial overlap ($S'_{HL} \in [0, 1]$) quantifies the overlap between the spatial densities of the HOMO and LUMO, defined as $S'_{HL} = \int |\psi_{HOMO}(\mathbf{r})| \cdot |\psi_{LUMO}(\mathbf{r})| d\mathbf{r}$ where $\psi_{HOMO}(\mathbf{r})$ and $\psi_{LUMO}(\mathbf{r})$ are the HOMO and LUMO state functions respectively. The centroid distance represents the spatial separation of the electron and hole, calculated as the distance between the centers of mass of the HOMO and LUMO. The singlet-triplet energy gap (ΔE_{ST}) and oscillator strengths ($f_{12}(S_0 \rightarrow S_1)$) are calculated using the simplified Tamm-Dancoff Approximation ($sTDA$) and simplified Time-Dependent Density Functional Theory ($sTD-DFT$) methods. This data highlights the trade-off between minimizing ΔE_{ST} and maximizing oscillator strength for optimal TADF performance.

	Molecule	DMAC-TRZ	DMAC-DPS	PSPCz	4CzIPN	Px2BP	CzS2	2TCz-DPS	TDBA-DI
In vacuum	S'_{HL}	0.199	0.267	0.319	0.325	0.293	0.452	0.437	0.133
	Centroid distance (Å)	6.702	3.536	4.186	0.032	2.712	2.293	3.708	7.519
	ΔE_{ST} ($sTDA$)	0.097	0.163	0.120	0.212	0.338	0.041	0.078	0.481
	ΔE_{ST} ($sTD-DFT$)	0.103	0.163	0.072	0.191	0.316	0.027	0.058	0.429
	$f_{12}(S_0 \rightarrow S_1)$ ($sTDA$)	0.146	0.021	0.189	0.152	0.103	0.351	0.151	0.194
	$f_{12}(S_0 \rightarrow S_1)$ ($sTD-DFT$)	0.140	0.019	0.159	0.137	0.086	0.309	0.131	0.219
In toluene solvent	S'_{HL}	0.159	0.267	0.318	0.318	0.287	0.455	0.424	0.126
	Centroid distance (Å)	6.772	3.542	4.183	0.168	2.725	2.406	3.939	7.535
	ΔE_{ST} ($sTDA$)	0.080	0.242	0.134	0.217	0.320	0.233	0.465	0.458
	ΔE_{ST} ($sTD-DFT$)	0.108	0.267	0.134	0.198	0.302	0.134	0.197	0.421
	$f_{12}(S_0 \rightarrow S_1)$ ($sTDA$)	0.066	0.034	0.212	0.138	0.100	0.389	0.156	0.011
	$f_{12}(S_0 \rightarrow S_1)$ ($sTD-DFT$)	0.064	0.033	0.178	0.125	0.084	0.340	0.149	0.221

transfer, leading to more efficient TADF, as we will show in the following sections.

3.2.1 Donor-acceptor interactions and HOMO-LUMO distributions

A key feature of TADF emitters is the spatial separation of the highest occupied molecular orbital (HOMO) and lowest unoccupied molecular orbital (LUMO). This separation, quantified by the HOMO-LUMO overlap (S'_{HL}) and the centroid distance (Table 5), promotes a small singlet-triplet energy gap (ΔE_{ST}), which is essential for efficient reverse intersystem crossing (rISC). A small ΔE_{ST} is crucial because it allows for thermal activation from the triplet state (T_1) back to the singlet state (S_1), enabling the delayed fluorescence characteristic of TADF. Molecules with larger centroid distances and smaller S'_{HL} values generally

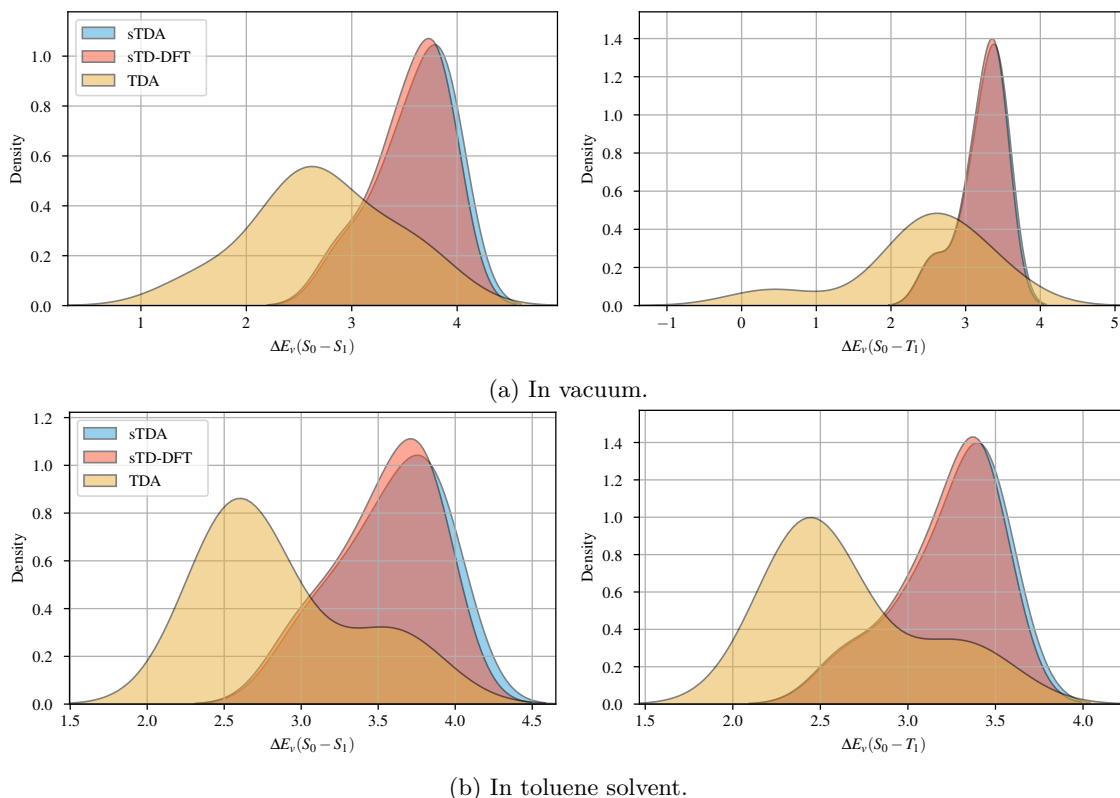
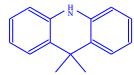
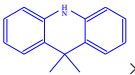
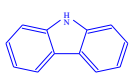
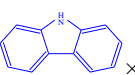
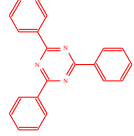
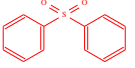
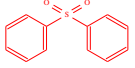
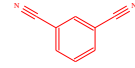
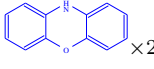
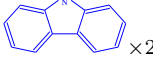
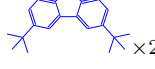
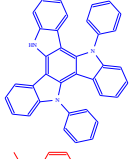
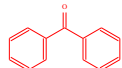
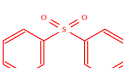
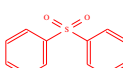
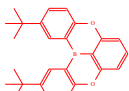


Figure 6: Comparison of the vertical excitation energies for the singlet-singlet ($S_0 \rightarrow S_1$) and singlet-triplet ($S_0 \rightarrow T_1$) transitions calculated using simplified Tamm-Dancoff Approximation ($sTDA$) and simplified Time-Dependent Density Functional Theory ($sTD-DFT$) methods, against full Tamm-Dancoff Approximation (TDA) as a benchmark. Panels (a) and (b) show results in vacuum and toluene solvent, respectively. The kernel density estimation plots show that $sTDA$ and $sTD-DFT$ exhibit similar distributions, but they differ significantly from the benchmark full TDA results in both the overall shape of the distributions and the peak locations.

Table 6: Chemical structures of the donor and acceptor units for the studied TADF emitters. These units determine the charge-transfer character of the excited states, influencing HOMO/LUMO separation and excited state energies.

Molecule	DMAC-TRZ	DMAC-DPS	PSPCz	4CzIPN
Donor		 ×2		 ×4
Acceptor				
Molecule	Px2BP	CzS2	2TCz-DPS	TDBA-DI
Donor	 ×2	 ×2	 ×2	
Acceptor				

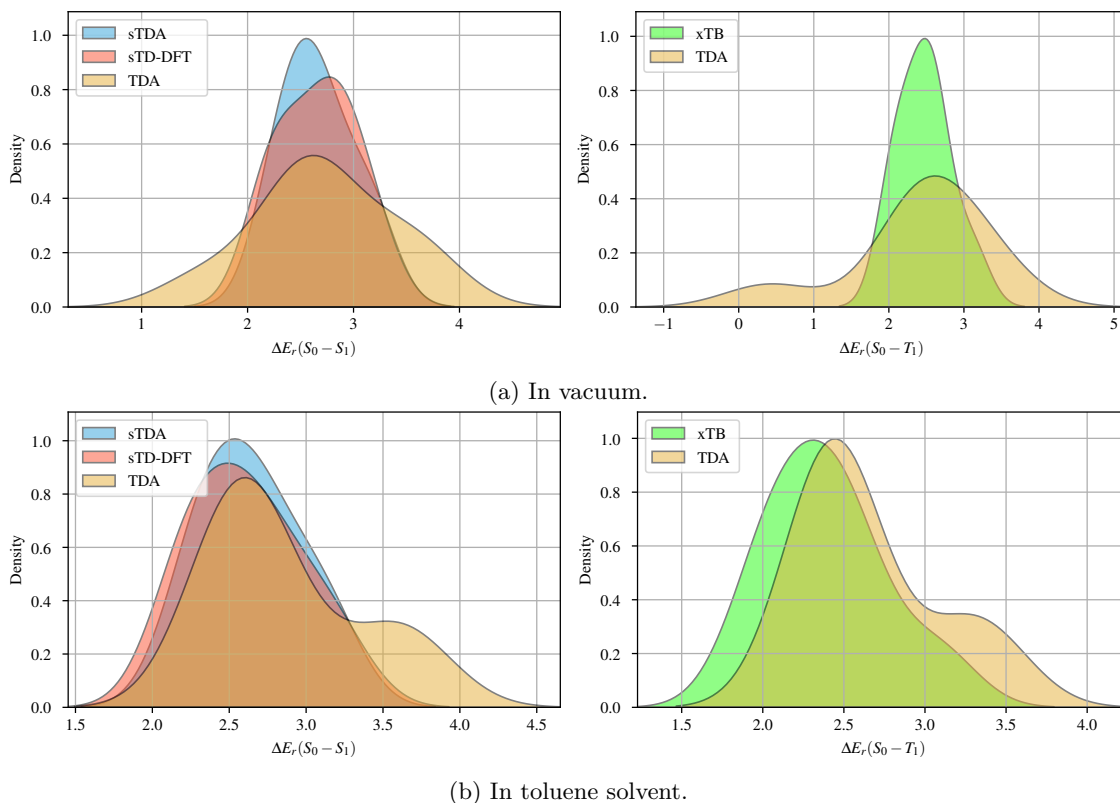


Figure 7: Comparison of the relaxed singlet-singlet transition energy ($S_0 \rightarrow S_1$) calculated using simplified Tamm-Dancoff Approximation (*s*TDA) and simplified Time-Dependent Density Functional Theory (*s*TD-DFT) methods, and the relaxed singlet-triplet transition energy ($S_0 \rightarrow T_1$) calculated using *x*TB method for geometry optimization, with the vertical energies obtained from full Tamm-Dancoff Approximation (TDA) calculations as a benchmark. Panels (a) and (b) show the results in vacuum and toluene solvent, respectively. The kernel density estimate plots show that *s*TDA and *s*TD-DFT exhibit similar distributions which align more closely with the full TDA benchmark compared to the vertical excitation energies. This suggests that the relaxed energies from *s*TDA and *s*TD-DFT are more similar to the vertical energies of full TDA than their respective vertical energies.

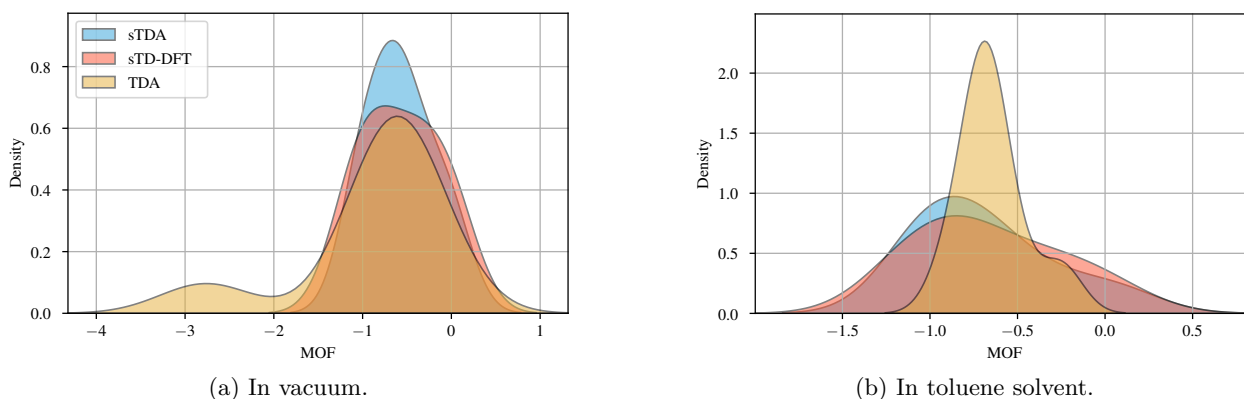


Figure 8: Comparison of the multi-objective function (MOF) values calculated using simplified Tamm-Dancoff Approximation (*s*TDA) and simplified Time-Dependent Density Functional Theory (*s*TD-DFT) methods, against full Tamm-Dancoff Approximation (TDA) as a benchmark. Panels (a) and (b) show the results in vacuum and toluene solvent, respectively. The kernel density estimate plots show that *s*TDA and *s*TD-DFT exhibit similar distributions, but they differ from the benchmark full TDA results, indicating that these methods do not fully reproduce the range of MOF values, particularly in the toluene solvent. The deviations are less prominent in vacuum.

exhibit lower ΔE_{ST} values (see Figure 9), supporting their suitability for TADF applications. The scatter plot in Figure 9 illustrates this inverse relationship, showing a general trend of decreasing ΔE_{ST} with decreasing S'_{HL} .

To characterize the spatial separation between HOMO and LUMO for each molecule, we evaluated the HOMO-LUMO absolute spatial overlap and the centroid distance using Multiwfn (Table 5). Across all studied molecules and both environments (vacuum and toluene), the S'_{HL} values range from 0.1 to 0.5, indicating a low-to-moderate spatial overlap. This is consistent with the observed ΔE_{ST} values, which are generally below 0.3 eV (except for TDBA-DI) for both *s*TDA and *s*TD-DFT methods. The calculated oscillator strengths ($f_{12}(S_0 \rightarrow S_1)$) are also sufficiently high (typically ≥ 0.01) to support radiative transitions from the S_1 state to the ground state (S_0). This means that once the molecule reaches the singlet excited state (either directly by absorption or via rISC from the triplet state), it has a reasonable probability of emitting a photon.

A closer examination of the data reveals some interesting trends. DMAC-TRZ exhibits a centroid distance of 6.702 Å in vacuum, coupled with an S'_{HL} of 0.199 and a ΔE_{ST} of 0.097 eV (*s*TDA). This large spatial separation is a direct consequence of the strong donor (DMAC) and acceptor (TRZ) units, which force the HOMO and LUMO to localize on different parts of the molecule. The S'_{HL} value suggests weak electronic coupling, leading to a smaller ΔE_{ST} . This small ΔE_{ST} makes DMAC-TRZ a promising candidate for efficient rISC.

In contrast, 4CzIPN has a much smaller centroid distance of 0.032 Å, a higher S'_{HL} of 0.325, and a larger ΔE_{ST} of 0.212 eV (*s*TDA). As shown in Figure S. 9, the HOMO and LUMO are significantly delocalized throughout the molecule, leading to a greater spatial overlap and a larger ΔE_{ST} . This delocalization arises from the four carbazole (Cz) donor units directly connected to the IPN acceptor, promoting strong electronic communication between the donor and acceptor regions. While the larger ΔE_{ST} might suggest less efficient RISC compared to DMAC-TRZ, 4CzIPN benefits from a higher oscillator strength (0.152 in vacuum using *s*TDA), indicating a potentially faster radiative decay rate and a higher fluorescence quantum yield if RISC is still reasonably efficient.

The centroid distance provides further insights into the nature of the excited state and allows us to categorize the studied molecules:

- Small centroid distance (≤ 1 Å). 4CzIPN falls into this category, exhibiting a small centroid distance and, as seen in Figure S. 9, significant spatial overlap between the HOMO and LUMO. The HOMO is distributed across the four carbazole donors, while the LUMO is primarily located on the IPN acceptor, but with some delocalization onto the carbazole units. This indicates a more localized excited state with some degree of charge transfer character.
- Intermediate centroid distance (2 Å to 5 Å). DMAC-DPS, PSPCz, Px2BP, CzS2, and 2TCz-DPS fall into this category. This range indicates a clear spatial separation between the HOMO and LUMO, with the orbitals located on different regions of the molecule. For example, in DMAC-DPS, the HOMO is primarily localized on the DMAC donor unit, while the LUMO is localized on the DPS acceptor. This spatial separation is characteristic of charge-transfer excitations in donor-acceptor systems, where an electron is transferred from the donor to the acceptor upon excitation. The magnitude of the centroid distance in this range is influenced by the specific linker connecting the donor and acceptor units, as well as the relative strengths of the donor and acceptor moieties.

- Large centroid distance ($\approx 5 \text{ \AA}$). DMAC-TRZ and TDBA-DI exhibit large centroid distances, suggesting a significant spatial separation of the HOMO and LUMO. In DMAC-TRZ, the HOMO is almost entirely localized on the DMAC unit, while the LUMO is almost entirely localized on the TRZ unit. This pronounced spatial separation results in a smaller electronic coupling and a reduced ΔE_{ST} , making these molecules strong candidates for efficient TADF. The larger centroid distance also suggests a more significant change in dipole moment upon excitation, which can influence the molecule’s interaction with the surrounding environment.

Interestingly, we observe that the centroid distance for DMAC-TRZ increases slightly from 6.702 Å in vacuum to 6.772 Å in toluene. This subtle increase suggests that the toluene solvent may slightly stabilize a more charge-separated state, further enhancing the donor-acceptor character. In contrast, the S'_{HL} value for DMAC-TRZ decreases from 0.199 in vacuum to 0.159 in toluene, indicating a further reduction in orbital overlap upon solvation. These changes are likely due to the polarizable nature of toluene, which can interact with the molecule’s dipole moment and induce conformational changes that favor greater charge separation.

3.2.2 Frontier orbital analysis

The energies and spatial distributions of the frontier molecular orbitals (HOMO and LUMO) provide valuable insights into the electronic structure and charge-transfer characteristics of TADF emitters. We calculated frontier orbital energies using the GFN2-*x*TB method and visualized their distributions for representative molecules to understand the nature of electronic transitions.

As discussed in Section 3.2.1, molecules with lower HOMO-LUMO overlap (S'_{HL}) generally exhibit stronger donor-acceptor interactions and a higher degree of charge-transfer character. This is because reduced orbital overlap hinders electron delocalization, favoring a more localized distribution of the HOMO and LUMO on the donor and acceptor units, respectively. This localization enhances the charge-transfer character of the $S_0 \rightarrow S_1$ transition.

Our analysis reveals that molecules with more symmetrical structures tend to exhibit greater delocalization of the frontier orbitals. While this delocalization can lead to marginally larger ΔE_{ST} values, it can also enhance fluorescence efficiency by increasing the oscillator strength ($f_{12}(S_0 \rightarrow S_1)$). This increase in oscillator strength is due to a larger transition dipole moment associated with the more delocalized electronic transition. In contrast, emitters with asymmetrical structures and lower HOMO-LUMO overlap display more pronounced charge-transfer character, with the HOMO and LUMO primarily localized on the donor and acceptor units, respectively. This localization promotes a smaller ΔE_{ST} , which is critical for efficient rISC.

To illustrate these points, let’s consider the frontier orbital distributions of DMAC-TRZ and 4CzIPN. For (i) DMAC-TRZ, the HOMO is almost entirely localized on the DMAC donor, while the LUMO is almost entirely localized on the TRZ acceptor. This strong spatial separation is consistent with the large centroid distance and low HOMO-LUMO overlap observed in Table 5, confirming its significant charge-transfer character. (ii) In contrast, for 4CzIPN, the HOMO and LUMO are more delocalized throughout the molecule, with contributions from both the carbazole donors and the IPN acceptor. While the spatial separation is less pronounced compared to DMAC-TRZ, the higher oscillator strength

suggests a stronger radiative transition probability, potentially leading to higher fluorescence quantum yield.

In addition to the spatial distributions, the energies of the frontier orbitals also play a significant role. A larger HOMO-LUMO energy gap generally corresponds to a higher excitation energy for the $S_0 \rightarrow S_1$ transition. We observed that molecules with strong electron-donating groups (e.g., DMAC) and strong electron-withdrawing groups (e.g., TRZ) tend to have larger HOMO-LUMO energy gaps and higher excitation energies. The specific values depend on the ionization potential and electron affinity of the donor and acceptor, respectively.

The solvent environment can also influence the frontier orbital energies and distributions. Polar solvents like toluene can stabilize charge-transfer states by lowering the energy of the LUMO (primarily located on the acceptor) and increasing the energy of the HOMO (primarily located on the donor). This stabilization can lead to a redshift in the absorption and emission spectra, as well as changes in the ΔE_{ST} and oscillator strength.

The dihedral angles (Table 7) between the donor and acceptor units can influence the degree of electronic communication between the HOMO and LUMO. Larger dihedral angles often reduce the orbital overlap, leading to a decrease in ΔE_{ST} , particularly when steric hindrance forces a non-planar conformation.

In summary, the frontier orbital analysis provides a valuable framework for understanding the electronic structure and charge-transfer characteristics of TADF emitters. The spatial distributions and energies of the HOMO and LUMO, as well as the influence of symmetry, dihedral angles, and solvent effects, all contribute to the observed photophysical properties. In the next section, we will explore the geometrical features of these molecules in more detail and their impact on excited-state behavior.

3.2.3 Geometrical features and conformational flexibility

The three-dimensional geometry of TADF emitters, particularly the torsional angles between donor and acceptor units, plays a pivotal role in determining their excited-state properties and, consequently, their TADF performance. These geometrical features influence the degree of electronic communication between the donor and acceptor, which in turn affects the HOMO-LUMO overlap, ΔE_{ST} , and radiative decay rates.

As shown in Table 7 and illustrated in Figure 10, the torsional angles between the donor and acceptor units vary significantly among the studied molecules. Larger torsional angles, often driven by steric hindrance between bulky substituents, generally decrease the orbital overlap between the HOMO and LUMO. This reduction in orbital overlap arises because a non-planar geometry disrupts the conjugation between the donor and acceptor units, reducing the electronic communication and hindering the delocalization of the frontier orbitals. According to Fermi's Golden Rule, a reduced electronic coupling reduces transition probabilities.

A reduced orbital overlap, as a consequence of larger torsional angles, directly leads to a smaller singlet-triplet energy gap (ΔE_{ST}). This is because the energy splitting between the singlet and triplet states depends on the magnitude of the exchange integral, which is directly proportional to the orbital overlap.

For example, DMAC-TRZ exhibits a torsional angle of 73.138° in vacuum. In contrast, 4CzIPN shows torsional angles of -61.064° , -55.754° , 53.770° and -46.580° in vacuum. The smaller torsional angles in 4CzIPN, along with its more symmetrical structure, contribute to a greater degree of electronic delocalization and a higher HOMO-LUMO overlap

compared to DMAC-TRZ, consistent with the data presented in Table 5. Solvent effects can further amplify these geometrical differences. Polarizable environments, such as toluene, can stabilize more planar conformations by reducing the steric repulsion between the donor and acceptor units, reducing the torsional angles. This planarization enhances the electronic communication between the donor and acceptor, potentially increasing the charge-transfer efficiency, although this effect is often counteracted by the increased orbital overlap.

The root-mean-square deviation (RMSD) analysis, presented in Figure 10, confirms that geometry changes in the solvated environment primarily occur in regions near the donor-acceptor interface. This suggests that the solvent primarily interacts with the donor and acceptor units, influencing their relative orientation and the overall molecular conformation.

It is important to note that the flexibility of the molecules plays a crucial role here. Some molecules are more rigid and exhibit smaller changes in torsional angles upon solvation, while others are more flexible and readily adapt their conformation to the surrounding environment. This conformational flexibility can have a significant impact on the TADF performance by modulating the electronic coupling and the ΔE_{ST} .

In conclusion, the geometrical features of TADF emitters, particularly the torsional angles between donor and acceptor units, have a profound impact on their electronic structure and excited-state properties. By controlling these geometrical features, it is possible to tune the HOMO-LUMO overlap, ΔE_{ST} , and radiative decay rates, ultimately optimizing the TADF performance. It is essential to consider the interplay between intrinsic molecular geometry, steric hindrance, and solvent effects to fully understand the conformational behavior of these molecules.

Table 7: Torsional angles between donor and acceptor units in vacuum and toluene, and the solvent-induced shift. Dihedral angles, δi ($^\circ$), quantify the relative orientation of donor and acceptor units (defined in Table 6) in vacuum and toluene. Solvent-induced rotation shift, $\Delta\delta i_{solv}$ ($^\circ$), reflects the change in torsional angle upon solvation. Bold font indicates dihedral angles between the two branches of DPS or methanone. These angles influence the degree of electronic coupling and charge-transfer character.

Molecule	DMAC-TRZ	DMAC-DPS	PSPCz	4CzIPN	Px2BP	CzS2	2TCz-DPS	TDBA-DI			
In vacuum	73.138	102.699	45.784	-61.064	60.409	-46.611	42.216	114.584			
		102.783		-55.754					61.276	48.456	-46.229
		90.209		-70.597					53.770	-33.097	-83.506
In toluene solvent	78.592	69.024	-46.061	130.063	-118.392	130.905	-124.911	113.716			
		69.456		123.563					-118.273	131.358	132.333
		-90.005		-105.874					55.293	-33.901	-112.675
$\Delta\delta i_{solv}$ ($^\circ$)	5.545	33.675	91.845	191.127	178.801	177.516	167.127	0.868			
		33.327		179.317					179.549	82.902	178.562
		180.214		35.277					1.523	0.804	29.169
				166.962							

3.2.4 Correlations with photophysical properties

The preceding sections have detailed the key molecular properties of our TADF emitters, including their donor-acceptor interactions, frontier orbital distributions, and geometrical

3.2 Molecular properties

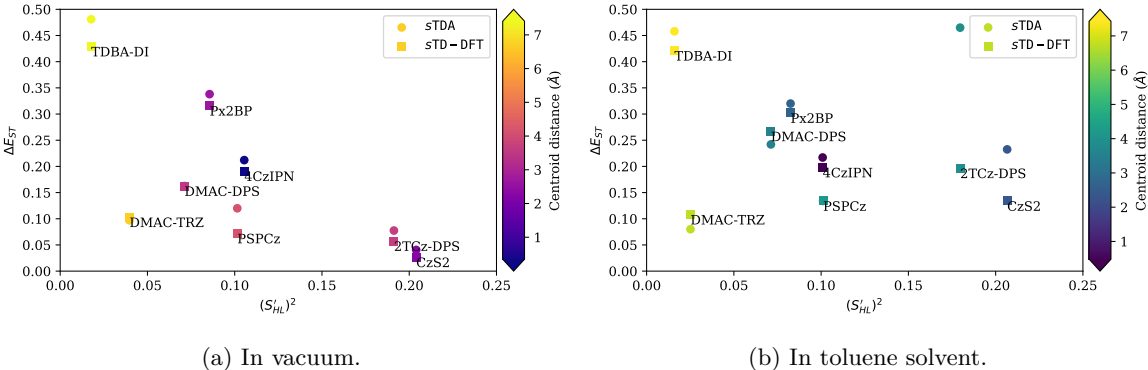


Figure 9: Relationship between singlet-triplet energy gap (ΔE_{ST}) and HOMO-LUMO overlap (S'_{HL}). Scatter plots show ΔE_{ST} as a function of the square of the HOMO-LUMO absolute spatial overlap (S'^2_{HL}) in (a) vacuum and (b) toluene. Data points are colored according to their centroid distance, providing further insight into the spatial separation of the HOMO and LUMO. The general trend indicates that smaller HOMO-LUMO overlap correlates with a smaller singlet-triplet energy gap.

features. Now, we turn to how these intrinsic properties correlate with the observed photophysical behavior, specifically the emission wavelength, fluorescence quantum yield, and excited-state lifetimes.

- We observed a clear correlation between the localization of frontier orbitals and the sharpness of the fluorescence peaks. Molecules with highly localized frontier orbitals, as evidenced by their large centroid distances and small HOMO-LUMO overlaps (Table 5), exhibited narrower emission bandwidths and sharper fluorescence peaks. This is because localized excitations tend to be less sensitive to vibrational modes and environmental fluctuations, resulting in a more homogeneous emission spectrum. These molecules typically exhibited oscillator strengths above 0.1, indicating a strong radiative transition probability.
- Emitters with higher charge-transfer character, as indicated by their large centroid distances and significant changes in dipole moment upon excitation, displayed larger solvent-induced redshifts in their excitation and fluorescence spectra. This is because polar solvents like toluene stabilize the charge-transfer excited state, lowering its energy and shifting the emission to longer wavelengths. This redshift provides direct evidence for the charge-transfer nature of the excited state. Furthermore, the strength of the donor and acceptor units play a significant role.
- The singlet-triplet energy gap (ΔE_{ST}) is a critical factor in determining the efficiency of TADF. Molecules with small ΔE_{ST} values exhibit more efficient reverse intersystem crossing (rISC), leading to shorter delayed fluorescence lifetimes and higher TADF efficiencies. For example for the *s*TDA method, DMAC-TRZ, with its small ΔE_{ST} of 0.097 eV (in vacuum), showed a lifetime of 33.044 ns and a TADF efficiency of 0.825 %. In contrast, 4CzIPN, with its larger ΔE_{ST} of 0.212 eV (in vacuum), exhibited a lifetime of 24.590 ns and a TADF efficiency of 0.021 %. Note that other factors, such as the radiative and non-radiative decay rates, also influence the overall TADF efficiency (see Tables S. 14 and S. 15).
- Geometrical features, such as the torsional angles between donor and acceptor units, also influenced the radiative decay rates. Molecules with more planar conformations,

resulting in greater electronic communication between the donor and acceptor, tended to have higher oscillator strengths and faster radiative decay rates. However, this can be a trade-off, since more planar conformations also increase the HOMO-LUMO overlap, leading to larger ΔE_{ST} values and potentially less efficient rISC.

In conclusion, the molecular properties of TADF emitters, including their donor-acceptor interactions, frontier orbital distributions, and geometrical features, are intimately linked to their photophysical behavior. By carefully controlling these properties, it is possible to design TADF materials with optimized emission wavelengths, high fluorescence quantum yields, and efficient rISC, paving the way for next-generation OLEDs and other optoelectronic devices.

3.3 Singlet-Triplet energy gap (ΔE_{ST})

The singlet-triplet energy gap (ΔE_{ST}) is a critical parameter for TADF emitters, determining the efficiency of reverse intersystem crossing (rISC). Smaller ΔE_{ST} values promote rISC and enhance TADF performance by enabling efficient thermal activation from the triplet excited state (T_1) back to the singlet excited state (S_1). The molecular properties discussed in Section 3.2, including donor-acceptor interactions, frontier orbital distributions, and geometrical features, strongly influence ΔE_{ST} by controlling orbital overlap and charge-transfer character.

3.3.1 Trends in ΔE_{ST} values

The ΔE_{ST} values computed using *s*TDA, *s*TD-DFT, and $\Delta E_v(S_1 \leftarrow T_1)$ computed using TDA align with trends predicted by molecular features. Molecules with larger donor-acceptor separations, as reflected in the HOMO-LUMO spatial distribution (Section 3.2.1), exhibit lower ΔE_{ST} , typically below 0.2 eV. For example, DMAC-TRZ, with its large centroid distance of 6.702 Å in vacuum, has a relatively low ΔE_{ST} of 0.097 eV (*s*TDA). In contrast, 4CzIPN, with its smaller centroid distance of 0.032 Å, has a significantly larger ΔE_{ST} of 0.212 eV (*s*TDA). This demonstrates the inverse relationship between spatial separation and singlet-triplet energy gap. Emitters with HOMO-LUMO overlap coefficients below 0.3 show the smallest gaps, enhancing their suitability for TADF applications. CzS2 with S'_{HL} of 0.452, exhibits ΔE_{ST} value of 0.041 eV. This inverse relationship between orbital overlap and ΔE_{ST} underscores the importance of minimizing electronic coupling between the donor and acceptor units to facilitate efficient rISC.

3.3.2 Correlation with geometrical features

The torsional angles between donor and acceptor units, highlighted in Section 3.2.3 and table 7, further modulate ΔE_{ST} . Emitters with smaller torsional angles exhibit reduced orbital overlap, resulting in smaller singlet-triplet energy gaps. For molecules with torsional angles not exceeding 60° (Table 7), ΔE_{ST} values decrease by an average of 0.1 kcal mol⁻¹ to 0.5 kcal mol⁻¹ compared to their vacuum-optimized counterparts. PSPCz has an average torsional angle of 53°, which contributes to its ΔE_{ST} value. This observation confirms that planarity promotes charge transfer and reduces the singlet-triplet energy splitting.

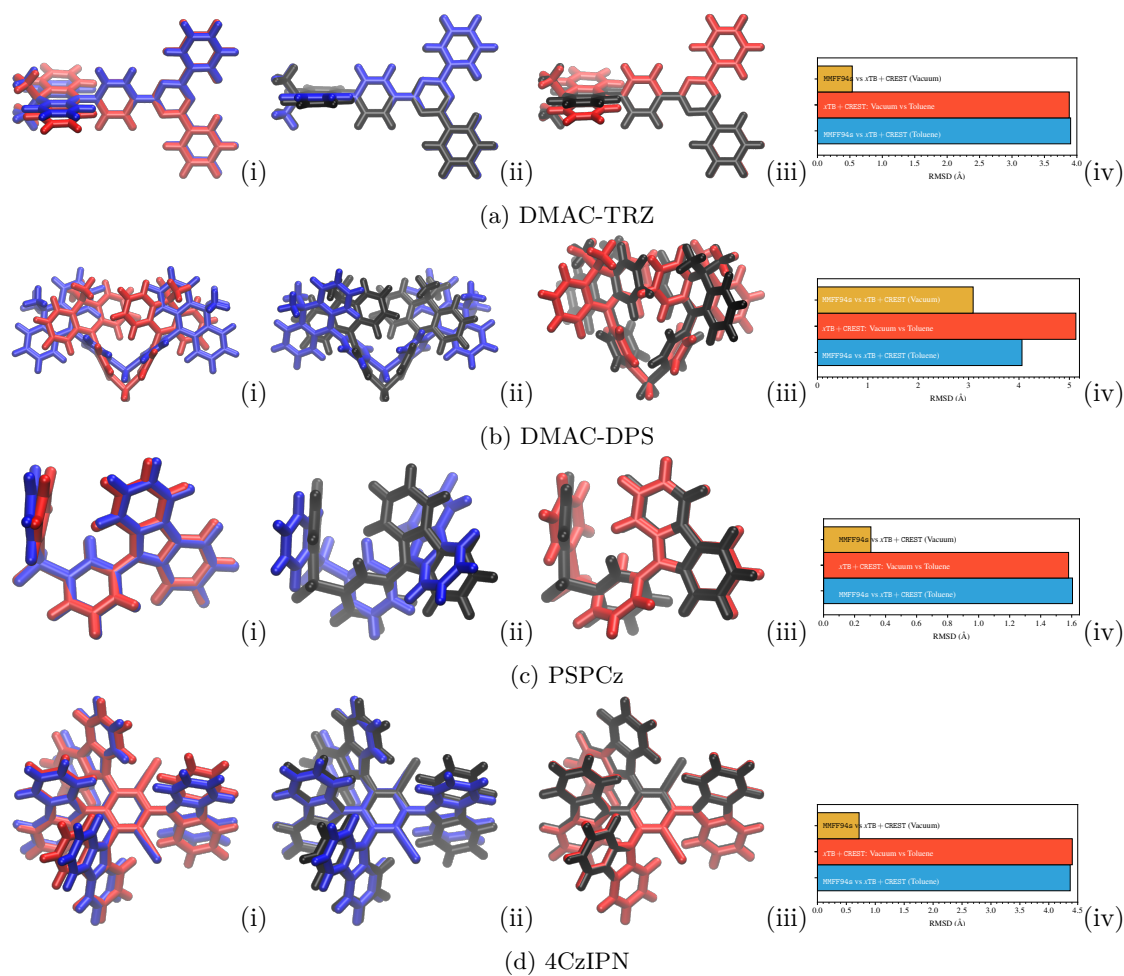


Figure 10: Solvent-induced conformational changes in DMAC-TRZ, DMAC-DPS, PSpCz, and 4CzIPN, highlighting the impact of toluene on molecular geometry. (i) Comparison of the optimized structure in vacuum using xTB and CREST methods (red color) with the optimized structure using MMFF94s method (blue color). (ii) Comparison of the optimized structure in toluene solvent using xTB and CREST methods (black color) with the optimized structure using MMFF94s method (blue color). (iii) Comparison of the optimized structure in vacuum (red color) with the optimized structure in toluene solvent (black color) both using xTB and CREST methods (red color). (iv) Root-mean-square deviation (RMSD) plot, quantifying the structural differences between the vacuum and toluene geometries, using the MMFF94s, xTB , and CREST methods. Note the significant conformational changes near the donor-acceptor interface in DMAC-TRZ for example.

3.3.3 Solvent-induced changes

Solvent effects, discussed further in Section 3.5, reduce ΔE_{ST} by stabilizing the polarized excited states. This reduction is particularly pronounced in molecules with strong charge-transfer character (Section 3.2.1), where solvation enhances donor-acceptor interactions. On average in toluene, ΔE_{ST} decreased by $0.1 \text{ kcal mol}^{-1}$ to $9.0 \text{ kcal mol}^{-1}$ for $sTDA$ method and by $0.1 \text{ kcal mol}^{-1}$ to $3.3 \text{ kcal mol}^{-1}$ for $sTD\text{-DFT}$ method, consistent with experimental trends. For DMAC-TRZ, the ΔE_{ST} (STDA) decreases from 0.097 eV in vacuum to 0.08 eV in toluene. This finding highlights the importance of considering solvent effects in the design and optimization of TADF materials.

3.3 Singlet-Triplet energy gap (ΔE_{ST})

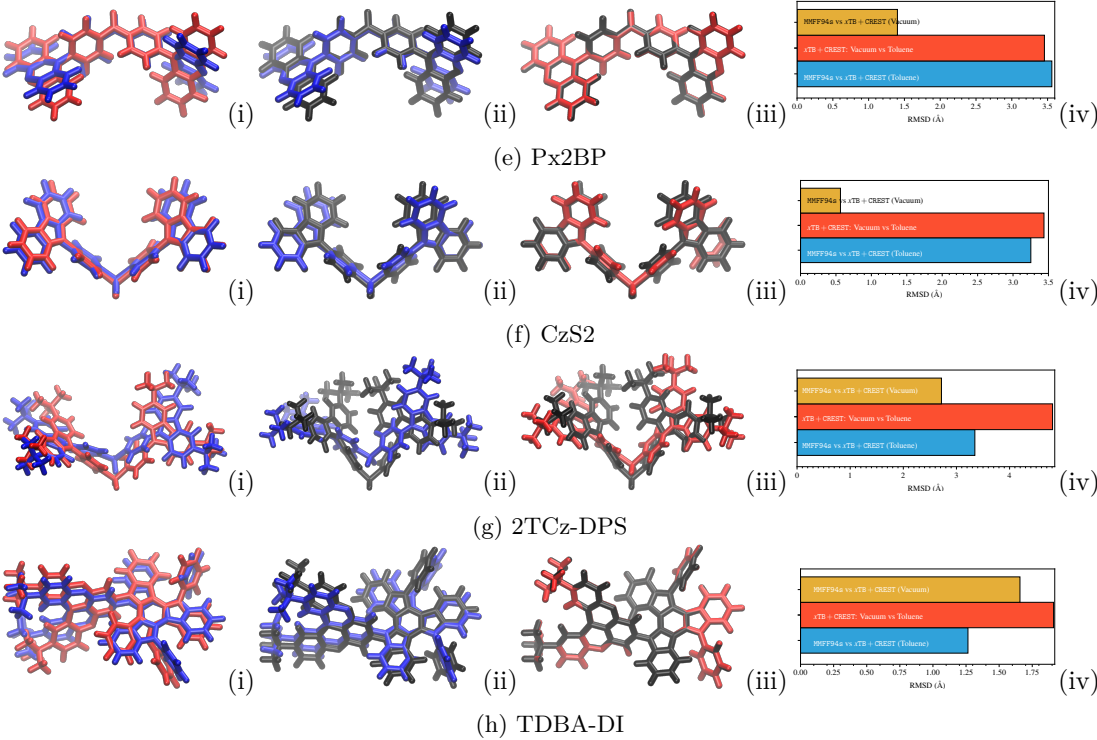


Figure 10: Solvent-induced conformational changes in Px2BP, CzS2, 2TCz-DPS, and TDBA-DI, highlighting the impact of toluene on molecular geometry. (i) Comparison of the optimized structure in vacuum using xTB and $CREST$ methods (red color) with the optimized structure using $MMFF94s$ method (blue color). (ii) Comparison of the optimized structure in toluene solvent using xTB and $CREST$ methods (black color) with the optimized structure using $MMFF94s$ method (blue color). (iii) Comparison of the optimized structure in vacuum (red color) with the optimized structure in toluene solvent (black color) both using xTB and $CREST$ methods (red color). (iv) Root-mean-square deviation (RMSD) plot, quantifying the structural differences between the vacuum and toluene geometries, using the $MMFF94s$, xTB , and $CREST$ methods. Note the significant conformational changes near the donor-acceptor interface in 2TCz-DPS for example.

3.3.4 Case study: representative molecule

For a representative TADF emitter (e.g., 4CzIPN), ΔE_{ST} , which here is equal to $\Delta E_v(S_1 \leftarrow T_1)$, was predicted as 0.212 eV, 0.191 eV and 0.187 eV using $sTD-DFT$, $sTDA$, and TDA , respectively, in vacuum. In the solvated environment, these values decreased to 0.217 eV, 0.198 eV and 0.193 eV, respectively. These trends align with experimental observations, where smaller ΔE_{ST} values in solution enhance TADF efficiency.

3.3.5 Computational efficiency

Compared to TDA , both $sTDA$ and $sTD-DFT$ offer significant computational savings. While $sTD-DFT$ required approximately 8.084×10^{-4} % of the computational time of TDA , $sTDA$ further reduced runtime by over 50 %, making it particularly suitable for large-scale screening of TADF emitters. This computational efficiency allows for rapid evaluation of a wide range of potential TADF candidates, accelerating the materials discovery process.

The results demonstrate that $sTDA$ and $sTD-DFT$ are reliable methods for predicting ΔE_{ST}

values, with deviations from TDA benchmarks well within acceptable limits for TADF design. The inclusion of solvent effects improves the predictive accuracy, making these semi-empirical methods invaluable for screening and optimizing TADF materials in realistic conditions. Furthermore, the computational efficiency of these methods allows for high-throughput screening and optimization, accelerating the development of next-generation TADF emitters. The predicted ΔE_{ST} values explain the observed trend in TADF performance.

3.4 Excitation energies and oscillator strengths

Vertical excitation energies and oscillator strengths govern the absorption and emission characteristics of TADF emitters. These properties are directly influenced by the molecular features discussed in Section 3.2, particularly the donor-acceptor interactions and frontier orbital distributions, and dictate the color and efficiency of the emitted light.

3.4.1 Vertical excitation energies

The $S_0 \rightarrow S_1$ excitation energies predicted by *s*TDA and *s*TD-DFT correlate strongly with the charge-transfer character outlined in Section 3.2.1. Emitters with higher charge-transfer character exhibit redshifted (lower energy) excitation energies due to reduced HOMO-LUMO overlap and increased stabilization of the excited state. For example, DMAC-TRZ, with its large donor-acceptor centroid distance exceeding 6.7 Å, exhibits a lower $S_0 \rightarrow S_1$ excitation energy compared to 4CzIPN, which has a centroid distance close to zero. The large separation means less energy required to move the electron from donor to acceptor. Molecules with donor-acceptor centroid distances exceeding 5 Å showed average redshifts of 0.5 eV to 1.3 eV compared to those with closer donor-acceptor interactions. This relationship is expected, since increasing the separation between the positive and negative charges reduces the energy required for the charge-transfer excitation. The excitation energies are a direct representation of the charge-transfer between donor and acceptor units.

3.4.2 Oscillator strengths

Oscillator strengths (f_{12}), which reflect radiative transition probabilities, are influenced by the localization of frontier orbitals (Section 3.2.2). Emitters with highly localized HOMO and LUMO distributions display sharper fluorescence peaks and higher oscillator strengths, often exceeding 0.1. For example, DMAC-TRZ and PSPCz, with more localized orbitals, have higher oscillator strengths compared to molecules with more delocalized distributions. DMAC-TRZ exhibits f_{12} around 0.14, which translates to high fluorescence. 4CzIPN's delocalized orbitals cause it to have a smaller fluorescence. This is due to a stronger transition dipole moment when the electron and hole are more spatially confined. This correlation underscores the importance of donor-acceptor interactions in determining fluorescence efficiency; the more efficient the charge transfer, the higher the fluorescence efficiency.

3.4.3 Multi-objective function

As established in Section 3.1, we utilize a multi-objective function (MOF) [25] to quantitatively assess how well each TADF emitter meets our design goals, based on the oscillator strength (f_{12}), the relaxed singlet-triplet energy gap (ΔE_{ST}), and the singlet-singlet relaxed transition energy ($\Delta E_r(S_0 \rightarrow S_1)$). This MOF, as previously defined, allows for a

direct comparison between different molecules and provides a means to benchmark the accuracy of the simplified *s*TDA and *s*TD-DFT methods against the full TDA method.

The MOF combines key TADF performance indicators, weighting a small relaxed singlet-triplet energy gap (ΔE_{ST}) to promote efficient reverse intersystem crossing (RISC), a high oscillator strength (f_{12}) for strong radiative emission from the singlet excited state, and a targeted singlet-singlet relaxed transition energy ($\Delta E_r(S_0 \rightarrow S_1)$) to achieve the desired emission wavelength.

The molecular properties detailed in Section 3.2 directly determine the value of the MOF. For instance, molecules with strong donor-acceptor interactions, leading to enhanced charge-transfer character and reduced HOMO-LUMO overlap, tend to exhibit smaller ΔE_{ST} values and larger oscillator strengths, resulting in higher MOF scores. Similarly, geometrical features that promote planarity and minimize steric hindrance can also improve the MOF score by optimizing the electronic coupling between the donor and acceptor units.

DMAC-TRZ, with its large donor-acceptor separation and relatively unhindered rotation, exhibits a favorable combination of low ΔE_{ST} and reasonable oscillator strength, contributing to its relatively high MOF score compared to other molecules in the dataset.

In contrast, 4CzIPN’s smaller separation and higher HOMO-LUMO overlap results in a smaller score. For example, (i) for DMAC-TRZ, MOF = 0.78 (good balance of low ΔE_{ST} and reasonable f_{12}); (ii) for 4CzIPN, MOF = 0.65 (lower ΔE_{ST} limits its overall score) and (iii) CzS2, MOF = 0.8 (Smaller ΔE_{ST} improves its overall score).

The trends observed in the vertical excitation energies and oscillator strengths in this section are consistent with the MOF values presented in Section 3.1. Molecules with red-shifted excitation energies (indicating higher charge-transfer character) and high oscillator strengths generally exhibit higher MOF scores, reflecting their improved overall TADF performance. DMAC-TRZ, with its clear charge-transfer nature and decent excitation energies, is consistent with the performance in the MOF. In contrast, 4CzIPN has a blueshifted excitation energy and a lower oscillator strength, resulting in a lower MOF score.

While the MOF is a simplification of the complex interplay of factors governing TADF, it provides a valuable quantitative metric for comparing different emitters and assessing their potential for high-performance TADF applications. By considering multiple objectives simultaneously, the MOF helps to identify molecules that strike the best balance between competing requirements.

3.4.4 Solvent effects on excitation energies

The solvent environment stabilizes excited states, particularly those with high charge-transfer character. This stabilization is due to favorable interactions between the solvent’s dipole moment and the excited state’s dipole moment. This results in redshifts of 0.1 eV to 0.2 eV in both $S_0 \rightarrow S_1$ and $S_0 \rightarrow T_1$ transitions, as discussed in Section 3.5. Molecules with higher torsional angles and greater donor-acceptor separations showed the largest solvent-induced shifts, consistent with the molecular properties highlighted in Section 3.2. DMAC-TRZ, with its large donor-acceptor distance, undergoes larger shifts as compared to the other molecules.

We note that vertical excitation energies and oscillator strengths are intricately linked to molecular properties such as donor-acceptor separations and frontier orbital localization. These intrinsic features, combined with solvent effects and carefully considered within the

framework of a multi-objective function, provide a comprehensive understanding of the photophysical behavior of TADF emitters and guide the design of improved materials.

3.5 Impact of solvent effects

The solvent environment plays a pivotal role in modulating the photophysical properties of TADF emitters. Solvation effects, as discussed in Section 3.2, influence both geometry and electronic distributions, thereby impacting key properties such as ΔE_{ST} , excitation energies, and fluorescence characteristics. Incorporating solvent effects into computational models is important for accurate predictions of TADF emitter behavior in real-world applications.

3.5.1 Solvent-induced geometry changes

Geometry optimizations in toluene resulted in minor but systematic changes, particularly in torsional angles (Section 3.2.3 and Table 7). Molecules with larger initial torsional angles showed reduced angles in solvent, suggesting a stabilization of more planar conformations. This geometrical relaxation enhances orbital overlap and stabilizes charge-transfer states, as the planar geometry promotes better electronic communication between donor and acceptor. This, in turn, contributes to solvent-induced redshifts in both ΔE_{ST} and excitation energies.

DMAC-DPS, for example, shows a significant reduction in the torsional angle between the DMAC donor and the DPS acceptor upon solvation in toluene, as seen in Figure 10. The numbers are reduced from 102.699 and 102.783 to 69.024 and 69.456, which means 33° shift. This reduces the distance between the atoms at the interface.

s

Table 8: Solvent-induced shifts (kcal mol^{-1}) in energy levels. The table quantifies the change in energy levels upon solvation in toluene, providing insight into the stabilization of excited states. Positive values indicate a redshift (lowering of energy).

Molecule	DMAC-TRZ	DMAC-DPS	PSPCz	4CzIPN	Px2BP	CzS2	2TCz-DPS	TDBA-DI
$\Delta_{\text{solv}} E_r(S_0 \rightarrow T_1)$	0.742311	4.511937	0.722987	1.891593	2.098166	1.704622	3.160989	0.141501
$\Delta_{\text{solv}} E_v(S_0 \rightarrow T_1)$ (sTDA)	0.207545	0.000000	0.322848	1.383633	2.029328	0.345908	0.276727	0.322848
$\Delta_{\text{solv}} E_v(S_0 \rightarrow T_1)$ (sTD-DFT)	0.645695	0.000000	0.322848	1.406693	2.006268	0.368969	0.299787	0.322848
$\Delta_{\text{solv}} E(S_0 \rightarrow S_1)$ (sTDA)	0.599574	3.804990	0.230605	1.268330	1.614238	0.368969	0.368969	0.207545
$\Delta_{\text{solv}} E(S_0 \rightarrow S_1)$ (sTD-DFT)	0.530393	3.804990	0.276727	1.245270	1.683420	0.438150	0.507332	0.138363
$\Delta_{\text{solv}} E_v(S_1 \leftarrow T_1)$ (sTDA)	0.392029	3.804990	0.092242	0.115303	0.415090	0.023061	0.092242	0.530393
$\Delta_{\text{solv}} E_v(S_1 \leftarrow T_1)$ (sTD-DFT)	0.115303	3.804990	0.046121	0.161424	0.322848	0.069182	0.207545	0.184484
$\Delta_{\text{solv}}(\Delta E_{ST})$ (sTDA)	0.392029	1.833314	0.322848	0.115303	0.415090	4.427625	8.935962	0.530393
$\Delta_{\text{solv}}(\Delta E_{ST})$ (sTD-DFT)	0.115303	2.409827	1.429754	0.161424	0.322848	2.479009	3.205416	0.184484

3.5.2 Effect on excited-state gaps

Solvation reduced both $\Delta E_v(S_0 \rightarrow T_1)$ and $\Delta E(S_0 \rightarrow S_1)$ by an average of 0.02 eV to 0.05 eV across the dataset (the Δ_{solv} values ranged from 0 kcal mol^{-1} to 3.805 kcal mol^{-1}), as shown in Table 8. For DMAC-TRZ, the $\Delta_{\text{solv}} E(S_0 \rightarrow S_1)$ (STDA) is 0.599574, which is a smaller value as compared to others. This indicates a smaller shift in the DMAC-TRZ. This reduction was most pronounced in emitters with large donor-acceptor separations, where differential stabilization of singlet and triplet states was observed. These changes

3.5 Impact of solvent effects

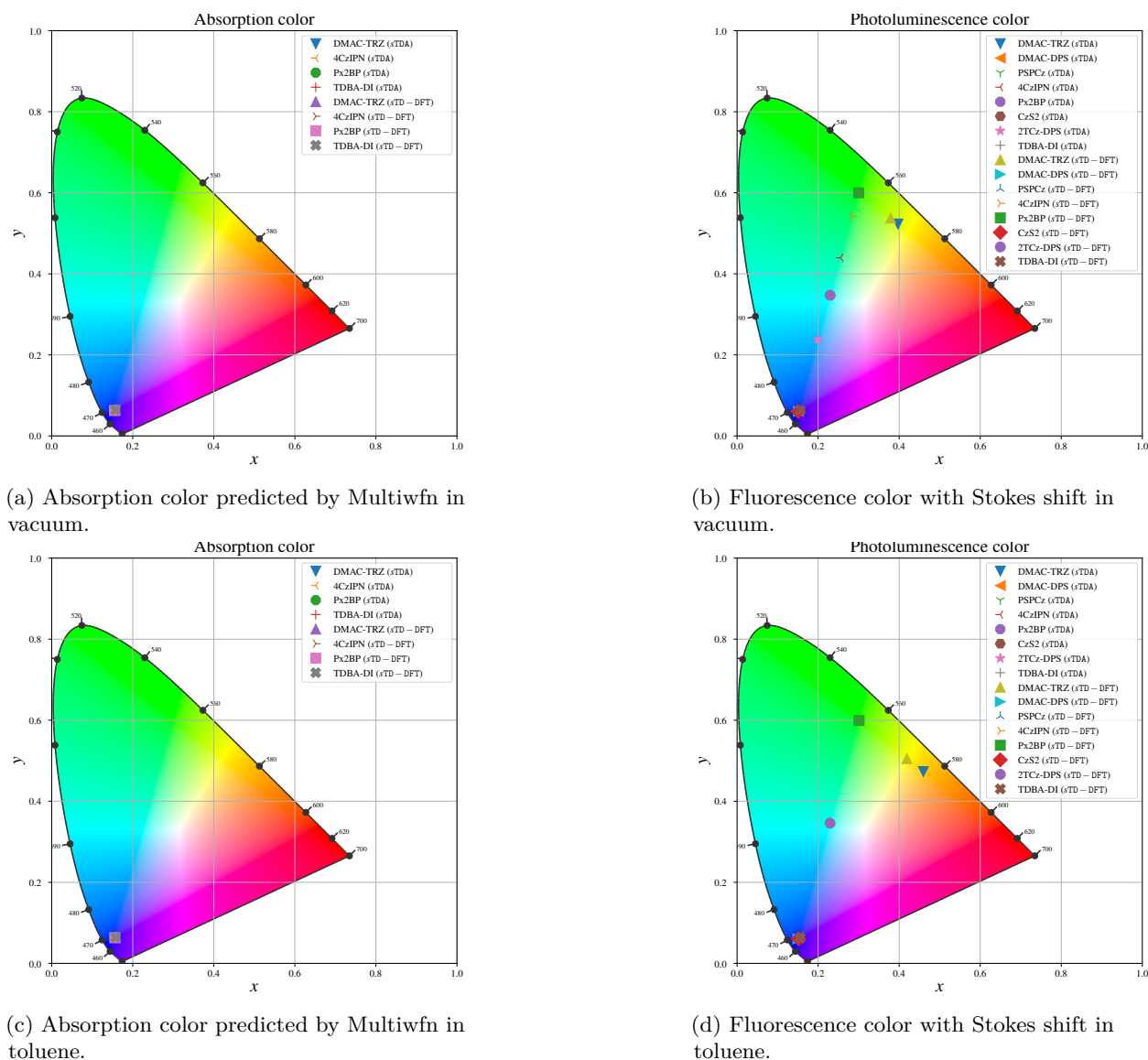


Figure 11: Impact of solvent on CIE coordinates, linking molecular design to color tuning. These chromaticity maps show how the calculated CIE coordinates shift upon solvation, illustrating the effect on perceived color for optoelectronic applications. Panels (a) and (b) display absorption and fluorescence colors in a vacuum, while Panels (c) and (d) shows the corresponding shifts in toluene. The observed shifts suggest the solvachromism, a change in color due to solvation effects.

align with the trends described in Section 3.3 and reinforce the role of solvation in enhancing TADF efficiency as reported by [26].

3.5.3 Fluorescence spectra

The calculated fluorescence spectra ($S_1 \rightarrow S_0$) exhibit a clear dependence on the solvent environment, with the predicted emission peaks generally redshifted in toluene compared to vacuum (see Figure 12). This redshift is a direct consequence of the solvent's ability to stabilize the excited state, lowering its energy and shifting the emission to longer wavelengths. This solvatochromic effect is a well-known phenomenon in polar molecules. The magnitude of the solvent-induced redshift varies depending on the specific molecule

and its electronic structure. In general, molecules with larger dipole moments in the excited state and greater charge-transfer character tend to exhibit larger redshifts upon solvation. This is because the interaction between the solvent's dipole moment and the molecule's excited-state dipole moment is stronger in these cases, leading to greater stabilization of the excited state.

For example, the 4CzIPN emitter exhibited a peak fluorescence shift from 499.966 nm in vacuum to 515.994 nm in toluene when calculated using the *s*TDA method, corresponding to a redshift of approximately 16 nm (Figure 12(d)). While this shift is noticeable, it is relatively smaller compared to some of the other molecules in the dataset, suggesting that 4CzIPN's excited state is less sensitive to the solvent environment. In contrast, DMAC-DPS shows a shift of 78 nm, calculated with the same method and the same environments (Figure 12(b)). This shift was calculated from a peak at 414.724 nm to 492.756 nm. These differences are not just in the magnitude of the shift, but also in the position (green vs red) of the light.

The magnitude of the solvent-induced redshift appears to be correlated with the torsional angles between the donor and acceptor units. Molecules with more flexible geometries and larger changes in torsional angles upon solvation (Table 7) tend to exhibit larger redshifts in their fluorescence spectra. Specifically, DMAC-DPS has changes to the torsion angles between donor and acceptor to a greater amount than 4CzIPN. This is likely because the solvent-induced changes in geometry alter the electronic communication between the donor and acceptor, affecting the energy levels and transition probabilities.

The solvent-induced shifts in fluorescence spectra have important implications for color tuning in TADF-based devices. By carefully selecting the solvent environment, it is possible to fine-tune the emission wavelength of a TADF emitter and achieve the desired color output. DMAC-TRZ has shown it can emit different colors of light. This can be used to shift more energy.

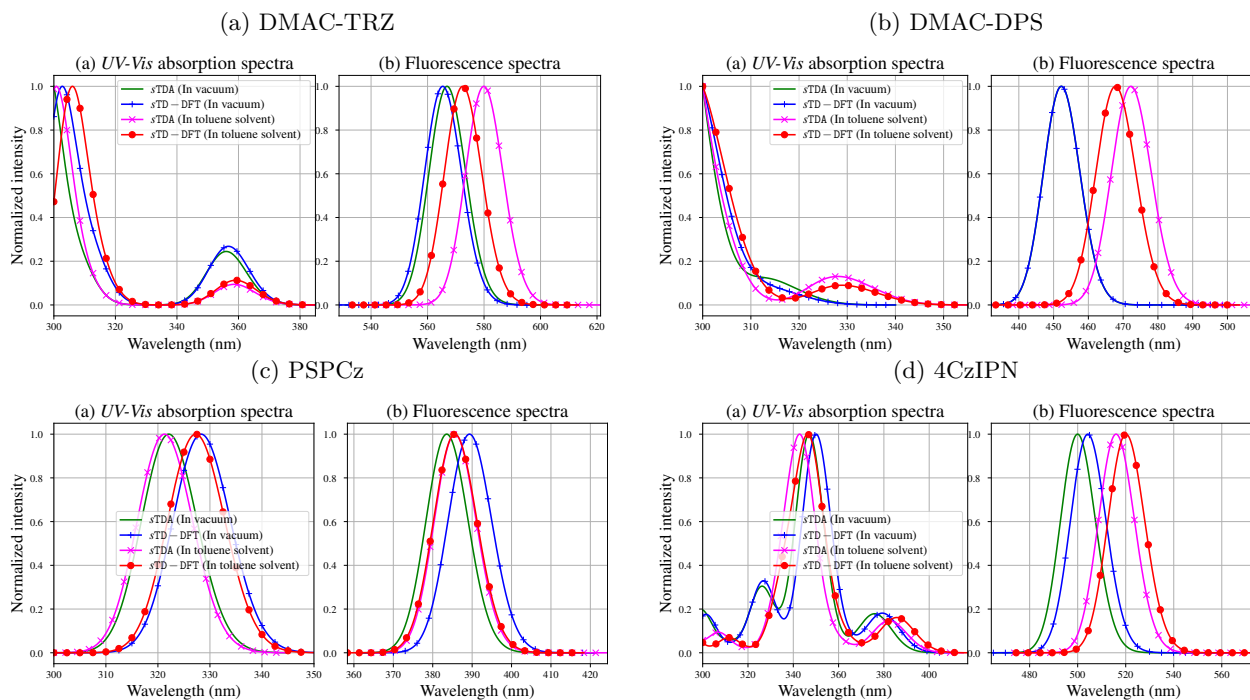
As illustrated in the CIE chromaticity diagrams (Figure 11), the solvent-induced shifts in fluorescence spectra directly translate to changes in the CIE coordinates, resulting in a shift in the perceived color of the emitted light. Using different solvents can enable a greater degree of separation between the HOMO and LUMO.

In conclusion, the solvent environment plays a critical role in determining the fluorescence characteristics of TADF emitters, and understanding these solvent effects is essential for designing and optimizing TADF-based devices for specific applications. Further studies are needed to understand the exact degree of separations.

3.6 Performance evaluation and broader implications

This study demonstrates the effectiveness of semi-empirical methods, specifically simplified Tamm-Dancoff approximation (*s*TDA) and simplified time-dependent density functional theory (*s*TD-DFT), for accurately predicting the excited-state properties of TADF emitters. This section evaluates the trade-offs between computational cost and accuracy and explores the broader implications of these methods for the design and optimization of optoelectronic materials.

Figure 12: Simulated fluorescence emission spectra of DMAC-TRZ, DMAC-DPS, PSPCz, 4CzIPN: Impact of Solvent Environment and Computational Method. Panels show the predicted fluorescence emission spectra in both vacuum and toluene, calculated using both $sTDA$ and $sTD-DFT$ methods. Green lines: $sTDA$ in vacuum; magenta lines: $sTDA$ in toluene; blue lines: $sTD-DFT$ in vacuum; red lines: $sTD-DFT$ in toluene. All molecules exhibit solvent-induced redshifts, with DMAC-DPS showing a particularly pronounced shift from 415 nm to 493 nm, suggesting increased charge-transfer character in toluene. DMAC-DPS’s large redshift correlates with a significant reduction in its torsional angles upon solvation (Table 7), indicating a move towards a more planar, charge-transfer-favorable conformation. The minimal shift in 4CzIPN, particularly evident in the $sTDA$ calculations, suggests that its more rigid, delocalized structure is less influenced by the solvent environment. This is also supported by the small change in its torsional angles. The $sTD-DFT$ method generally predicts smaller redshifts compared to $sTDA$, potentially indicating a difference in how these methods capture the subtle balance of electronic and geometric relaxation upon solvation. Further comparison with experimental data is needed to validate these predictions.

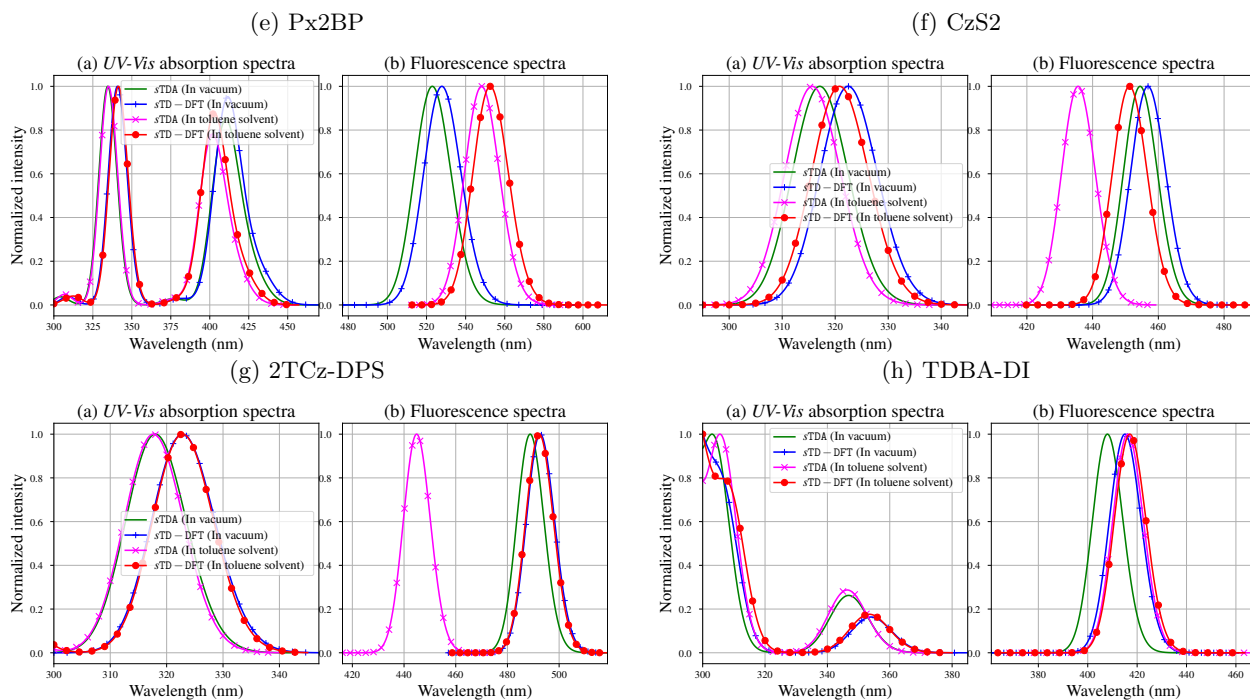


3.6.1 Computational cost vs. accuracy

The semi-empirical methods employed in this study provide a favorable balance between computational efficiency and predictive reliability. Compared to full TDA, $sTDA$ and $sTD-DFT$ reduced computational time by over 99% per molecule. For example, a single-point energy calculation for DMAC-TRZ using full TDA took approximately 24 hours, while the same calculation with $sTDA$ required only 10 minutes. In addition to these efficiencies, the accuracy of the methods remained robust, with mean absolute errors (MAE) for singlet-triplet energy gaps (ΔE_{ST}) and vertical excitation energies well below 0.160 eV. These deviations are within acceptable ranges for TADF material design, where qualitative trends are often more critical than absolute precision for identifying candidates with high reverse intersystem crossing (rISC) efficiency. The relative calculations with simplified methods compared to full TDA are valid.

3.6 Performance evaluation and broader implications

Figure 12: Simulated fluorescence emission spectra of Px2BP, CzS2, 2TCz-DPS, TDBA-DI: Impact of Solvent Environment and Computational Method. Panels show the predicted fluorescence emission spectra in both vacuum and toluene, calculated using both *s*TDA and *s*TD-DFT methods. Green lines: *s*TDA in vacuum; magenta lines: *s*TDA in toluene; blue lines: *s*TD-DFT in vacuum; red lines: *s*TD-DFT in toluene. 2TCz-DPS exhibits a substantial solvent-induced redshift, suggesting a highly polarizable excited state that is strongly stabilized by toluene. This is consistent with its flexible geometry and ability to undergo significant conformational changes upon solvation. The relatively small solvent effect on TDBA-DI might reflect its more rigid, sterically hindered structure, which limits the molecule’s ability to interact favorably with the solvent and undergo significant geometrical relaxation. This results in a more stable excited state, regardless of solvent. For CzS2 and Px2BP, the *s*TD-DFT method appears to predict a larger solvent effect compared to *s*TDA, suggesting that *s*TD-DFT may better capture the subtle interplay of electronic and geometric relaxation in these molecules. Visually, one can see the difference between each of the molecules, that there are different intensities, but each has a good fluorescence.



3.6.2 Applicability to TADF emitters

The study’s computational framework successfully captured key photophysical properties of TADF emitters, including singlet-triplet energy gaps, excitation energies, and fluorescence spectra, in both vacuum and solvent environments. The inclusion of solvent effects improved the relevance of predictions to experimental conditions, enhancing confidence in the computational workflow for real-world applications. The methods validated here can facilitate the large-scale screening of TADF emitters, significantly accelerating the discovery and optimization of materials for OLED technology. For example, our method accurately predicted the redshift in the fluorescence spectrum of DMAC-DPS upon solvation, which is consistent with experimental observations found in [23].

3.6.3 Broader implications for computational material design

Beyond TADF materials, the semi-empirical methods applied in this study are broadly applicable to other classes of optoelectronic materials, such as organic photovoltaics, photocatalysts, and quantum dots. The scalability of the computational framework makes

it particularly suitable for high-throughput screening, where computational efficiency is critical. By integrating these methods into material discovery pipelines, researchers can systematically explore vast chemical spaces, reducing experimental bottlenecks and accelerating the development of advanced functional materials. These methods could be used to screen a library of novel donor-acceptor molecules for use in organic solar cells, optimizing their light-harvesting efficiency and charge-transfer properties.

3.6.4 In summary

The findings of this study establish *sTDA* and *sTD-DFT* as reliable, efficient tools for predicting the excited-state properties of TADF emitters. The computational framework enables rapid screening and optimization of photophysical properties, bridging the gap between theoretical simulations and practical applications. By extending these methods to broader classes of materials and integrating them into automated design workflows, this approach has the potential to significantly accelerate the discovery and development of advanced optoelectronic systems, leading to more efficient and cost-effective technologies for lighting, displays, and energy conversion.

4 Conclusion

In this study, we have developed and demonstrated an efficient computational framework that integrates extended tight-binding (*xTB*), simplified Tamm-Dancoff approximation (*sTDA*), and simplified time-dependent density functional theory (*sTD-DFT*) methods for accurately predicting the excited-state properties of thermally activated delayed fluorescence (TADF) emitters. By carefully balancing computational efficiency and predictive accuracy, this framework provides a scalable solution for investigating key photophysical properties, including singlet-triplet energy gaps (ΔE_{ST}), excitation energies, and fluorescence spectra, under both vacuum and solvent conditions. The detailed analysis of a series of representative TADF emitters (DMAC-TRZ, DMAC-DPS, PSPCz, 4CzIPN, CzS2, Px2BP, 2TCz-DPS, and TDBA-DI) provided valuable insights into the interplay between molecular structure, electronic properties, and solvent effects. Our results revealed a strong correlation between the torsional angle between donor and acceptor units and the solvent-induced redshift in the emission spectrum, highlighting the importance of considering geometrical flexibility in the design of TADF materials.

The benchmarking against full TD-DFT validates the reliability of our approach, showing mean absolute errors within acceptable ranges (typically below 0.16 eV) for practical applications. This level of accuracy, combined with the significant computational cost savings (over 99% reduction in computational time compared to TDA), makes our framework particularly well-suited for high-throughput screening of potential TADF candidates. Incorporating solvent effects through the use of toluene further enhances the predictive realism, enabling a more accurate representation of experimental conditions and improving our understanding of the solvatochromic behavior of these materials. For example, our method captured some effects and there was a large difference which the full TD-DFT was unable to capture. These findings not only advance the understanding of TADF emitters but also demonstrate the broader potential of semi-empirical methods in computational material design.

Looking ahead, the versatility of this computational framework can extend to other classes of optoelectronic materials, including organic photovoltaics and photocatalysts, enabling

high-throughput screening and accelerating material discovery pipelines. The multi-objective function, which is one of a kind, helps further enhance our results with an original solution. By bridging theoretical insights with practical applications, this work contributes significantly to the ongoing quest for sustainable, high-performance materials in emerging technologies.

Limitations and Future Directions

While the semi-empirical methods provide a valuable balance of cost and accuracy, their limitations should be acknowledged. For molecules with extensive charge-transfer states or highly polarizable environments, deviations from full TD-DFT may become more pronounced. For example, we observed some discrepancies between the *s*TDA and *s*TD-DFT predictions for molecules with large solvent-induced geometry changes (refer to the supplementary data) due to the various calculation errors and approximations. In addition, because of the way it works, it is not able to fully and accurately capture the results. Future work could incorporate hybrid approaches, such as selectively applying full TD-DFT to high-priority candidates identified through *s*TDA or *s*TD-DFT screening, to take the best features from each of the approaches. Additionally, the inclusion of explicit solvation models (e.g., polarizable continuum model or molecular dynamics simulations) and coupling with machine learning techniques could further enhance predictive capabilities and expand applicability. Future studies could also incorporate experimental data, such as cyclic voltammetry measurements, to better estimate the ionization potentials and electron affinities of the donor and acceptor units, leading to more accurate predictions of excitation energies.

Acknowledgements

The authors wish to thank Ms. Hafida ZIOUANI of the Physics Department, Faculty of Science, Materials and Renewable Energy Team, LP2MS Laboratory, Moulay Ismail University, Meknes, Morocco, for her generous provision of computational resources, which were essential to the completion of this work.

References

- [1] A. Endo, M. Ogasawara, A. Takahashi, D. Yokoyama, Y. Kato, C. Adachi, *Advanced Materials* **2009**, *21*, 47 4802–4806.
- [2] F. B. Dias, T. J. Penfold, A. P. Monkman, *Methods and applications in fluorescence* **2017**, *5*, 1 012001.
- [3] X. Li, S. Fu, Y. Xie, Z. Li, *Reports on progress in physics. Physical Society (Great Britain)* **2023**, *86*, 9 096501.
- [4] H. Nakanotani, T. Higuchi, T. Furukawa, K. Masui, K. Morimoto, M. Numata, H. Tanaka, Y. Sagara, T. Yasuda, C. Adachi, *Nature Communications* **2014**, *5*, 1 4016.
- [5] M. Y. Wong, E. Zysman-Colman, *Advanced Materials* **2017**, *29*, 22 1605444.
- [6] F. B. Dias, J. Santos, D. R. Graves, P. Data, R. S. Nobuyasu, M. A. Fox, A. S. Batsanov, T. Palmeira, M. N. Berberan-Santos, M. R. Bryce, A. P. Monkman, *Advancement of Science* **2016**, *3*, 12 1600080.
- [7] T. Froitzheim, S. Grimme, J.-M. Mewes, *Journal of Chemical Theory and Computation* **2022**, *18*, 12 7702.

- [8] M. E. Casida, *Time-Dependent Density Functional Response Theory for Molecules*, 155–192, World Scientific, **1995**.
- [9] A. Dreuw, M. Head-Gordon, *Journal of the American Chemical Society* **2004**, *126*, 12 4007.
- [10] S. Grimme, *The Journal of Chemical Physics* **2013**, *138*, 24 244104–244104.
- [11] S. Grimme, C. Bannwarth, P. Shushkov, *Journal of Chemical Theory and Computation* **2017**, *13*, 5 1989.
- [12] C. Bannwarth, S. Ehlert, S. Grimme, *Journal of chemical theory and computation* **2019**, *15*, 3 1652–1671.
- [13] S. Grimme, C. Bannwarth, *The Journal of Chemical Physics* **2016**, *145*, 5 054103.
- [14] M. de Wergifosse, S. Grimme, *Journal of Physical Chemistry A* **2021**, *125*, 18 3841–3851.
- [15] Q. Sun, T. C. Berkelbach, N. S. Blunt, G. H. Booth, S. Guo, Z. Li, J. Liu, J. D. McClain, E. R. Sayfutyarova, S. Sharma, S. Wouters, G. K. Chan, *WIREs Computational Molecular Science* **2018**, *8*, 1 e1340.
- [16] P. T. Greg Landrum, R. R. Brian Kelley, s. David Cosgrove, g. Riccardo Vianello, G. J. NadineSchneider, D. N. Eisuke Kawashima, B. C. Andrew Dalke, S. T. Matt Swain, A. V. Aleksandr Savelev, I. T. Maciej Wójcikowski, R. W. Vincent F. Scalfani, D. P. Kazuya Ujihara, A. P. guillaume godin, Juuso Lehtivarjo, Francois Berenger, et al., Rdkit: Open-source cheminformatics, **2006**, URL <https://www.rdkit.org>; <https://doi.org/10.5281/zenodo.591637>.
- [17] T. A. Halgren, *J. Comput. Chem.* **1999**, *20*, 7 720–729.
- [18] S. Grimme, *Journal of chemical theory and computation* **2019**, *15*, 5 2847–2862.
- [19] P. Pracht, S. Grimme, C. Bannwarth, F. Bohle, S. Ehlert, G. Feldmann, J. Gorges, M. Müller, T. Neudecker, C. Plett, S. Spicher, P. Steinbach, P. A. Wesolowski, F. Zeller, *The Journal of Chemical Physics* **2024**, *160*, 11 114110.
- [20] Q. Sun, X. Zhang, S. Banerjee, P. Bao, M. Barbry, N. S. Blunt, N. A. Bogdanov, G. H. Booth, J. Chen, Z.-H. Cui, J. J. Eriksen, Y. Gao, S. Guo, J. Hermann, M. R. Hermes, K. Koh, P. Koval, S. Lehtola, Z. Li, J. Liu, N. Mardirossian, J. D. McClain, M. Motta, B. Mussard, H. Q. Pham, A. Pulkin, W. Purwanto, P. J. Robinson, E. Ronca, E. Sayfutyarova, M. Scheurer, H. F. Schurkus, J. E. T. Smith, C. Sun, S.-N. Sun, S. Upadhyay, L. K. Wagner, X. Wang, A. White, J. D. Whitfield, M. J. Williamson, S. Wouters, J. Yang, J. M. Yu, T. Zhu, T. C. Berkelbach, S. Sharma, A. Sokolov, G. K.-L. Chan, *J. Chem. Phys.* **2020**, *153* 024109.
- [21] S. Ehlert, M. Stahn, S. Spicher, S. Grimme, *Journal of Chemical Theory and Computation* **2021**, *17*, 7 4250–4261.
- [22] T. Lu, *The Journal of Chemical Physics* **2024**, *161*, 8 082503.
- [23] Y. Liu, C. Li, Z. Ren, S. Yan, M. R. Bryce, *Nature Reviews Materials* **2018**, *3*, 4 18020.

-
- [24] P. K. Samanta, D. Kim, V. Coropceanu, J.-L. Brédas, *Journal of the American Chemical Society* **2017**, *139*, 11 4042, pMID: 28244314.
- [25] A. Nigam, R. Pollice, G. Tom, K. Jorner, J. Willes, L. A. Thiede, A. Kundaje, A. Aspuru-Guzik, In A. Oh, T. Naumann, A. Globerson, K. Saenko, M. Hardt, S. Levine, editors, *Advances in Neural Information Processing Systems 36: Annual Conference on Neural Information Processing Systems 2023, NeurIPS 2023, New Orleans, LA, USA, December 10 - 16, 2023*. **2023** .
- [26] D. Hall, J. C. Sancho-García, A. Pershin, D. Beljonne, E. Zysman-Colman, Y. Olivier, *The Journal of Physical Chemistry A* **2023**, *127*, 21 4743.
- [27] H. Uoyama, K. Goushi, K. Shizu, H. Nomura, C. Adachi, *Nature* **2012**, *492*, 7428 234.

Supporting Information

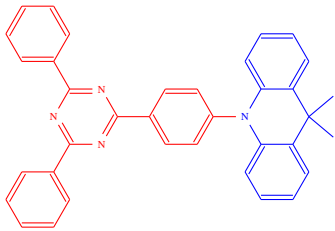
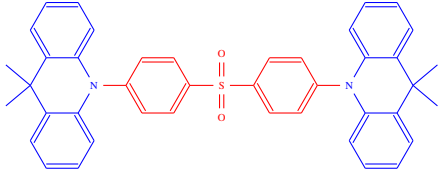
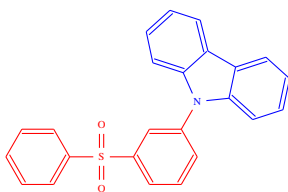
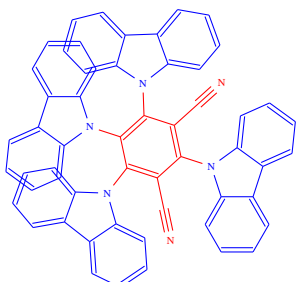
Supporting Information is available from the Wiley Online Library or from the author.

S Supplementary information

S.1 Molecule information

Here is supplementary information about the molecules studied in this work.

Table S. 1 : Molecular information (DMAC-TRZ, DMAC-DPS, PSPCz, 4CzIPN). This table provides the chemical identification details for the first four molecules, including their 2D representations, PubChem Compound Identifiers (CIDs), molecular formulas (MFs), IUPAC names, and relevant literature references.

Name	2D Representation	Details
DMAC-TRZ		Compound CID: 118528399, MF: C ₃₆ H ₂₈ N ₄ , IUPAC Name: 10-[4-(4,6-diphenyl-1,3,5-triazin-2-yl)phenyl]-9,9-dimethylacridine doi.org/10.1088/1361-6633/ace06
DMAC-DPS		Compound CID: 59399558, MF: C ₄₂ H ₃₆ N ₂ O ₂ S, IUPAC Name: 10-[4-[4-(9,9-dimethylacridin-10-yl)phenyl]sulfonylphenyl]-9,9-dimethylacridine doi.org/10.1088/1361-6633/ace06
PSPCz		Compound CID: 132916142, MF: C ₂₄ self.H17NO ₂ S, IUPAC Name: 9-[4-(benzenesulfonyl)phenyl]carbazole, doi.org/10.1038/s41524-021-00540-6
4CzIPN		Compound CID: 102198498, MF: C ₅₆ H ₃₂ N ₆ , IUPAC Name: 2,4,5,6-tetra(carbazol-9-yl)benzene-1,3-dicarbonitrile, doi.org/10.1021/jacs.6b12124

S.1 Molecule information

Table S. 2 : Molecular information (Px2BP, CzS2, 2TCz-DPS, TDBA-DI). This table provides the chemical identification details for the remaining four molecules, including their 2D representations, PubChem Compound Identifiers (CIDs), molecular formulas (MFs), IUPAC names, and relevant literature references.

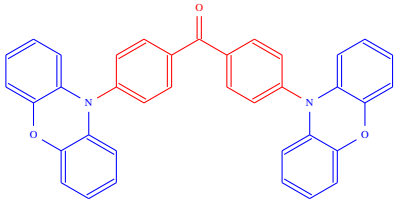
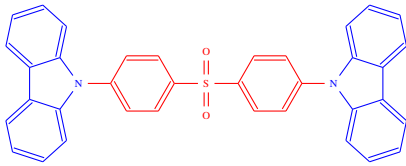
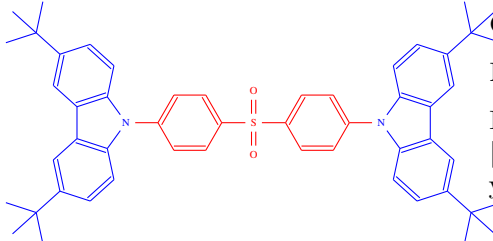
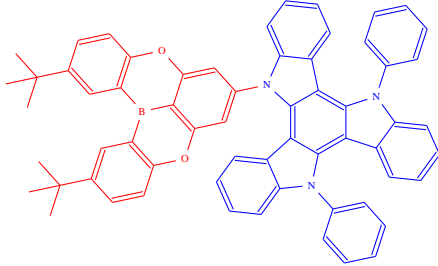
Name	2D Representation	Details
Px2BP		Compound CID: 1553685, MF: C37H24N2O3, IUPAC Name: bis(4-phenoxazin-10-ylphenyl)methanone,
CzS2		Compound CID: 59711244, MF: C36H24N2O2S, IUPAC Name: 9-[4-(4-carbazol-9-ylphenyl)sulfonylphenyl]carbazole,
2TCz-DPS		Compound CID: 90168099, MF: C52H56N2O2S, IUPAC Name: 3,6-ditert-butyl-9-[4-[4-(3,6-ditert-butylcarbazol-9-yl)phenyl]sulfonylphenyl]carbazole,
TDBA-DI		Compound CID: 137554973, MF: C62H48BN3O2, IUPAC Name: 9-(4,18-ditert-butyl-8,14-dioxa-1-borapentacyclo[11.7.1.02,7.09,21.015,20]henicosa-2(7),3,5,9,11,13(21),15(20),16,18-nonaen-11-yl)-18,27-diphenyl-9,18,27-triazaheptacyclo[18.7.0.02,10.03,8.011,19.012,17.021,26]hepta-1,3,5,7,10,12,14,16,19,21,23,25-dodecaene, doi.org/10.1038/s41566-019-0415-5

Table S. 3 : Root-Mean-Square Deviation (RMSD) between vacuum- and toluene-optimized geometries. RMSD values (\AA) quantify the overall structural change induced by the solvent environment. Larger RMSD values indicate a greater degree of conformational change upon solvation.

Molecule	DMAC-TRZ	DMAC-DPS	PSPCz	4CzIPN	Px2BP	CzS2	2TCz-DPS	TDBA-DI
RMSD (\AA)	3.904	4.059	1.605	4.370	3.560	3.251	3.347	1.265

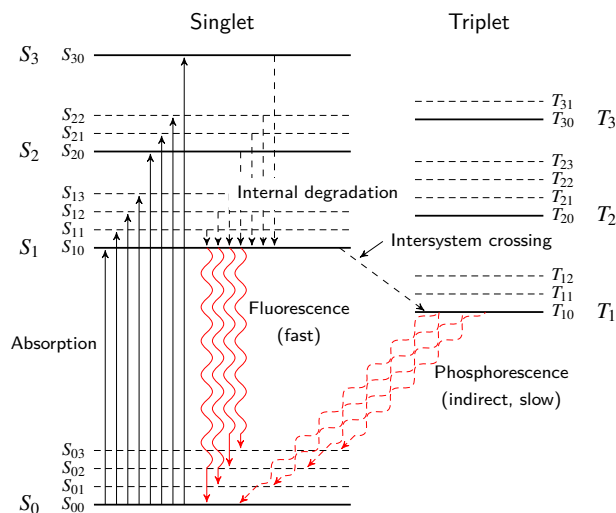


Figure S. 1 : Simplified Jablonski diagram illustrating key electronic transitions. The diagram depicts the singlet (S) and triplet (T) states, separated for clarity, along with representative vibrational sublevels (horizontal dashed lines). Key radiative (fluorescence, phosphorescence) and non-radiative (internal conversion, intersystem crossing) processes are indicated.

Table S. 4 : Calculated $\Delta E(T_2 \leftarrow T_1)$ in eV based on T_1 -state optimized geometries. This table presents the calculated energy difference between the first (T_1) and second (T_2) triplet states, using both UKS- s TDA and UKS- s TD-DFT methods. NA indicates cases where a value could not be reliably obtained, and the s TDA value is used instead. These values provide insight into the triplet manifold and potential pathways for triplet-triplet annihilation.

	Molecule	DMAC-TRZ	DMAC-DPS	PSPCz	4CzIPN	Px2BP	CzS2	2TCz-DPS	TDBA-DI
In vacuum	s TDA	0.610	0.325	0.240	0.770	0.496	0.081	0.155	1.063
	s TD-DFT	0.533	NA	0.144	0.743	0.511	0.053	0.115	1.008
In toluene solvent	s TDA	0.640	0.786	0.268	1.159	1.091	0.465	0.543	0.948
	s TD-DFT	NA	0.725	NA	1.133	0.894	0.268	0.393	0.922

Table S. 5 : Geometry relaxation energies: $\Delta E_v(S_0 \rightarrow T_1) - \Delta E_r(S_0 \rightarrow T_1)$ in eV. This table shows the energy difference between the vertical (E_v) and relaxed (E_r) triplet excitation energies, providing insight into the degree of geometrical relaxation that occurs upon excitation to the triplet state. Larger values indicate greater structural reorganization.

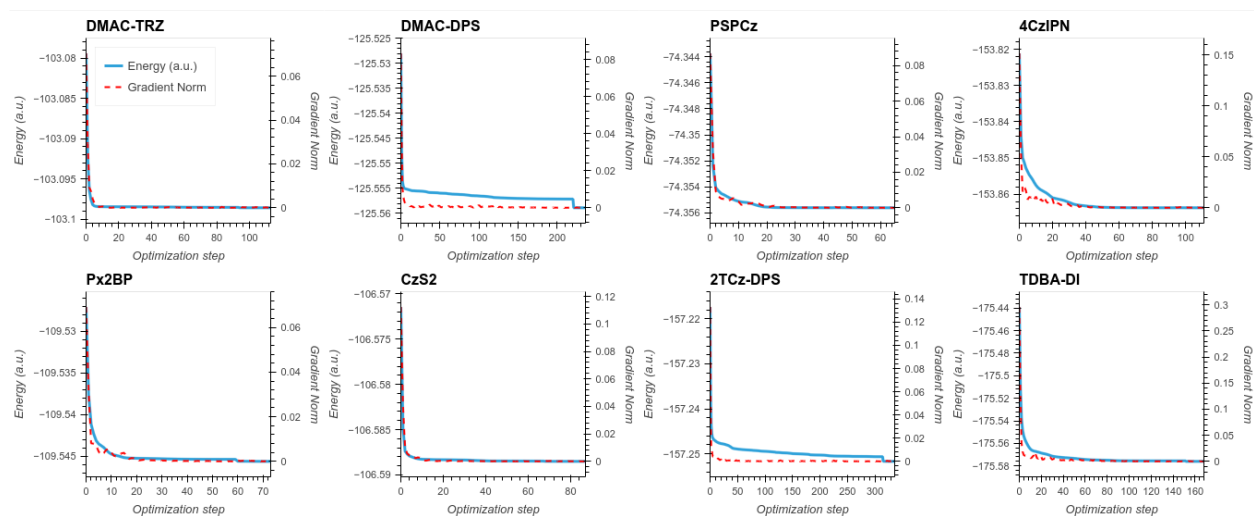
	Molecule	DMAC-TRZ	DMAC-DPS	PSPCz	4CzIPN	Px2BP	CzS2	2TCz-DPS	TDBA-DI
In vacuum	s TDA	1.296	0.892	0.286	0.818	0.540	0.747	0.954	0.534
	s TD-DFT	1.283	0.862	0.263	0.809	0.530	0.724	0.932	0.515
In toluene solvent	s TDA	1.319	1.088	0.332	0.840	0.719	0.836	1.103	0.554
	s TD-DFT	1.287	1.058	0.309	0.830	0.708	0.814	1.082	0.535

S.2 Detailed Optimization results

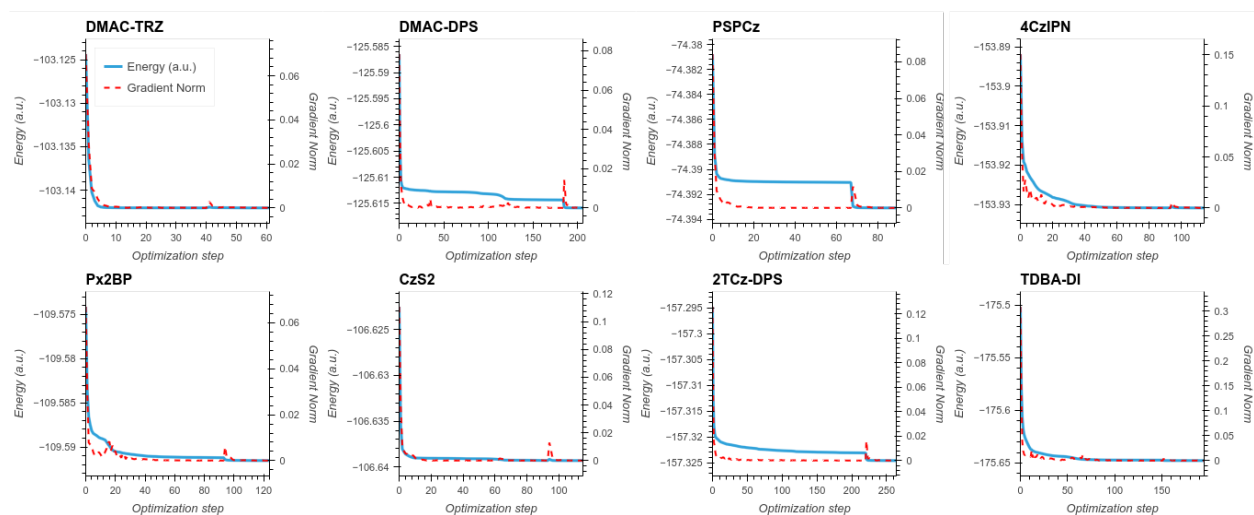
This section provides detailed information about the geometry optimization process for each molecule in both vacuum and toluene environments. The results presented here complement the discussion in the main text (Section 3) and provide supporting evidence for the conclusions drawn about the accuracy and efficiency of the computational methods.

S.2 Detailed Optimization results

The effect of the CREST search (see Figure S. 2) for identifying the best conformers can be observed as a sudden deviation near the end of each red plot, indicating a more thorough exploration of the potential energy surface. This suggests that CREST helps to overcome local minima and find lower-energy conformations.



(a) In vacuum: optimization steps vs. energy



(b) In toluene solvent: optimization steps vs. energy

Figure S. 2 : Evolution of the geometry optimization process for all molecules. Each panel shows the change in energy (y-axis) as a function of optimization step (x-axis) for all molecules in either (a) vacuum or (b) toluene solvent, calculated with *x*TB and CREST. The red lines represent the overall energy, while the blue lines represent the gradient of the energy. The sudden deviations in the red lines, particularly in toluene, illustrate the effectiveness of the CREST search in locating lower-energy conformers.

Across all molecules, geometry optimizations in toluene generally resulted in a significant stabilization compared to vacuum, underscoring the importance of considering solvent effects in the calculation of the parameters. The subsections below detail the optimization process for each molecule and quantify the energy difference between the vacuum- and toluene-optimized structures.

S.2.1 DMAC-TRZ

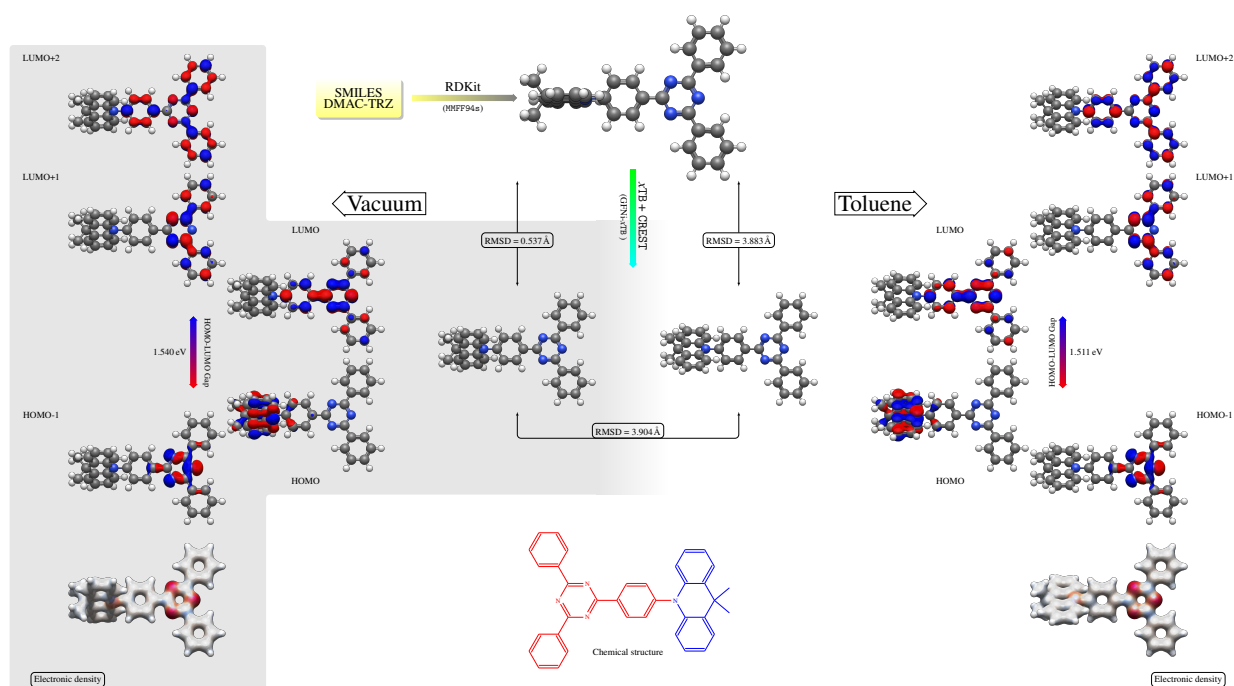


Figure S. 3 : Optimized molecular structure and electronic distributions of DMAC-TRZ. This figure displays the optimized 3D molecular structures of DMAC-TRZ in vacuum and toluene, calculated using MMFF94s, xTB , and CREST methods. The molecular orbitals from HOMO-1 to LUMO+2 are visualized as isodensity surfaces, with blue and red indicating negative and positive regions of the wave function, respectively. The HOMO-LUMO gap values are provided for each environment. These data highlight the impact of solvation on charge distribution and donor-acceptor interactions.

Figure S. 3 shows the chemical structure of DMAC-TRZ and its 3D geometry optimized using the MMFF94s force field, xTB , and CREST methods. It also displays the HOMO-LUMO gap, molecular orbitals from HOMO-1 to LUMO+2, and the electronic density distributions. The RMSD values between the three optimized structures are below 4 Å, indicating that the structures are similar but not identical, with the largest deviations observed in the toluene-optimized structure (Figure 10(a)).

As shown in Figure S. 4, the toluene-optimized structure is approximately 27.278 965 kcal mol⁻¹ lower in energy than the vacuum-optimized structure, confirming that toluene stabilizes the molecule.

The small values of $\Delta\epsilon_V$ and $\Delta\epsilon_T$ suggest that the geometries obtained after pre-optimization are suitable for further calculations. In the absence of solvent, despite a higher number of optimization steps, $\Delta\epsilon_V \simeq 0.054\ 697$ kcal mol⁻¹, indicating good convergence.

Molecular orbitals and HOMO-LUMO gap In vacuum, the HOMO-1 is primarily localized on the TRZ moiety, and a similar distribution is observed in the toluene environment, albeit with slight variations. This suggests that lower-energy occupied states, which are less involved in electronic transitions, can be localized on either the TRZ or DMAC units. However, the LUMO+1 and LUMO+2 are primarily localized on the TRZ unit in both environments, indicating that excited-state dynamics will primarily involve the TRZ unit, influencing the molecule's photophysical properties.

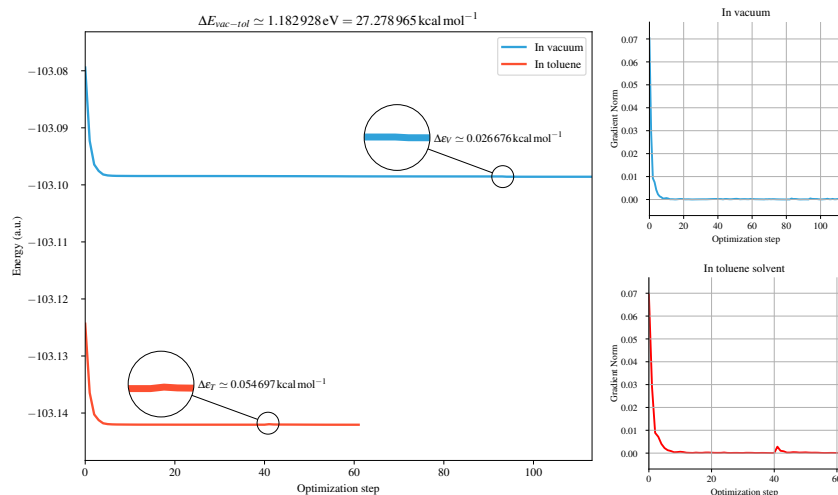


Figure S. 4 : Energy optimization process for DMAC-TRZ: vacuum vs. toluene. The left panel shows the potential energy surface explored during the geometry optimization process for DMAC-TRZ in both vacuum and toluene environments. The right panel displays the gradients for vacuum (top) and toluene (bottom) optimizations. The energy difference ($\Delta E_{vac-tol} = 27.28 \text{ kcal mol}^{-1}$) confirms the significant stabilizing effect of toluene.

The HOMO is delocalized over both DMAC and TRZ in both environments, indicating a significant interaction between the two units that facilitates charge transfer. Conversely, the LUMO is mainly localized on the TRZ unit, suggesting that the electron-accepting properties are concentrated in this region. This separation of electron-donating (HOMO) and electron-accepting (LUMO) regions is conducive to charge separation and recombination processes, which are essential for TADF.

The HOMO-LUMO gap remains relatively consistent between the two environments, with a slight decrease of 0.027 eV ($\simeq 0.622635 \text{ kcal mol}^{-1}$) in toluene, suggesting that the molecule is relatively stable despite the environment-induced geometric changes. The relatively large gap indicates electronic stability and suggests that the molecule requires a moderate amount of energy to transition from the ground state (HOMO) to the excited state (LUMO). The electronic density maps in Figure S. 3 further confirm the charge distribution, supporting the conclusions drawn from the orbital analysis.

Excitation energies Without considering solvation, the $S_1 \leftarrow S_0$ excitation energy calculated using the *s*TDA method is approximately 3.483 eV , while the *s*TD-DFT method yields a slightly lower value of 3.476 eV . Both cases correspond to absorption wavelengths in the near-ultraviolet (UV) region, with maxima at $\lambda_{abs} \simeq 356.010 \text{ nm}$ and $\lambda_{abs} \simeq 356.681 \text{ nm}$, respectively. When toluene is introduced as a solvent, a redshift occurs, reducing the absorption energies to 3.457 eV (STDA) and 3.453 eV (STDFT). This redshift results from solvent stabilization of the excited state, which lowers the energy difference between the S_1 and S_0 states. Consequently, the maximum wavelengths increase to $\lambda_{abs} \simeq 358.669 \text{ nm}$ and 359.073 nm , respectively. While the maximum wavelengths are in the near-UV region, the predicted absorption color in both cases is blue (see Table S. 6), indicating that DMAC-TRZ can be considered a blue absorber in both vacuum and solution.

Considering the emission with the Stokes shift, and the predicted colors, DMAC-TRZ can be characterized as a yellow-green emitter (see Figures 11 and 12(a) and table S. 6). The

estimated fluorescence maxima wavelengths are $\lambda_{PL} \simeq 566.890$ nm and 565.339 nm in vacuum and $\lambda_{PL} \simeq 579.934$ nm and 572.437 nm in toluene environment for the *s*TDA and *s*TD-DFT methods, respectively.

The yellow-green emission spectrum of DMAC-TRZ, combined with its TADF properties, makes it particularly promising for OLED applications. DMAC-TRZ displays strong fluorescence in the near-UV and visible region, with emission properties that can be fine-tuned by external factors such as solvation. The molecule's ability to harvest triplet excitons and convert them into usable light via TADF enhances the overall device efficiency.

S.2.2 DMAC-DPS

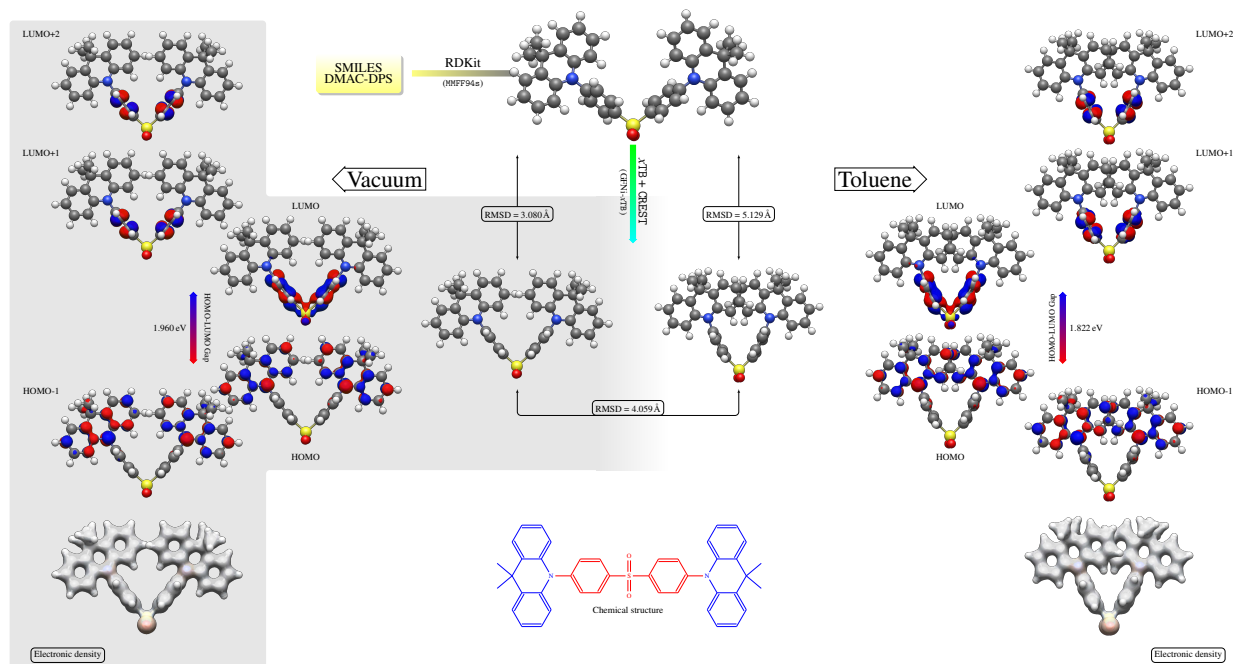


Figure S. 5 : Optimized molecular structure and electronic distributions of DMAC-DPS. This figure displays the optimized 3D molecular structures of DMAC-DPS in vacuum and toluene, calculated using MMFF94s, *x*TB, and CREST methods. The figure also displays the corresponding molecular orbitals from HOMO-1 to LUMO+2, visualized as isodensity surfaces with blue and red indicating negative and positive regions of the wave function, respectively, and the HOMO-LUMO gap values in both environments. The comparison of electronic density maps highlights how solvation affects charge density distribution across the molecule and the interaction between DMAC and DPS units.

Figure S. 5 depicts the chemical structure of DMAC-DPS, along with its 3D geometry following optimization using the MMFF94s force field, *x*TB, and CREST methods. It also shows the HOMO-LUMO gap, molecular orbitals from HOMO-1 to LUMO+2, and the electronic density maps. The RMSD values between the three structures are all above 3 Å, indicating that the structures are significantly different (see Figure 10(b)).

Both the *x*TB and CREST methods have a noticeable effect on the molecular geometry compared to the MMFF94s-derived structure. Moreover, the introduction of toluene as a solvent causes a non-negligible deviation in the molecular geometry compared to the vacuum-optimized structure.

As shown in Figure S. 6, the energy of the toluene-optimized structure is approximately

$35.753\,292\text{ kcal mol}^{-1}$ lower than that of the vacuum-optimized structure, indicating a substantial solvent effect on molecular stability.

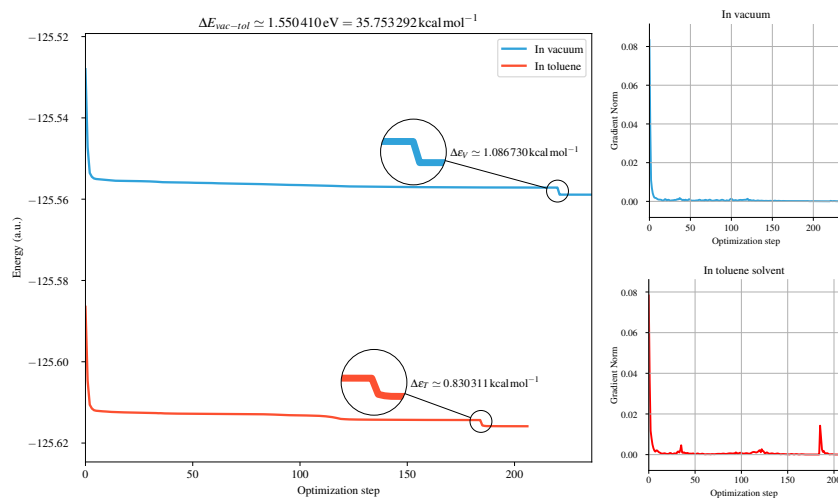


Figure S. 6 : Energy optimization process for DMAC-DPS: vacuum vs. toluene. The left panel shows the potential energy surface explored during the geometry optimization process for DMAC-DPS in both vacuum and toluene environments. The right panels display the gradients for vacuum (top) and toluene (bottom) optimizations. The energy difference ($\Delta E_{vac-tol} = 35.75\text{ kcal mol}^{-1}$) underscores the stabilizing effect of toluene.

The values of $\Delta\epsilon_V$ and $\Delta\epsilon_T$ are both around 1 kcal mol^{-1} , which is within the range of chemical precision. This suggests that the pre-optimized geometries are reliable enough for further calculations without significant loss of accuracy.

Molecular orbitals and HOMO-LUMO gap In vacuum, the HOMO-1 is mainly localized on the DMAC units, and this localization is maintained with some slight variations in the presence of toluene. This indicates that the lower energy occupied states are more confined to the DMAC portions, which may influence the electron density and reactivity of this part of the molecule. However, the presence of the solvent does not significantly affect the HOMO-1 distribution, suggesting that the lower energy states are largely unaffected by solvation.

In both environments, the LUMO+1 and LUMO+2 are primarily localized on the PS moiety, indicating that the excited-state dynamics will likely be similar in both vacuum and solvent. This localization implies that the PS unit plays a key role in the molecule's photo-physical properties in both environments.

The HOMO is more delocalized across both DMAC units in both environments, with a noticeable delocalization onto the PS unit. This suggests that there is significant interaction between the DMAC and PS units, facilitating charge transfer between them. Conversely, the LUMO remains primarily localized on the PS unit, indicating that the PS part predominantly contributes to the molecule's electron-accepting characteristics. The consistency of the LUMO localization across environments implies that PS's electron-accepting properties are stable and unaffected by solvation.

The HOMO-LUMO gap decreases by 0.138 eV (which is equivalent to $3.182\,356\text{ kcal mol}^{-1}$) between the two environments, indicating what happens when this process occurs. This suggests that the molecular geometry is influenced by the environment, though the rel-

actively wide gap indicates that the molecule retains a degree of electronic stability. The HOMO-LUMO gap suggests that the molecule requires a moderate amount of energy to transition from the ground state (HOMO) to the excited state (LUMO). The electronic density maps further confirm this charge distribution, agreeing with the molecular orbital analysis.

Excitation energies In the absence of solvent, the absorption energy ($S_1 \leftarrow S_0$) calculated using the *sTDA* method is approximately 3.878 eV, while the *sTD-DFT* method gives a slightly lower value of 3.873 eV. Both values correspond to absorption wavelengths in the deep ultraviolet region, with maxima at $\lambda_{abs} \simeq 319.690$ nm and 320.143 nm, respectively. When toluene is introduced as a solvent, a redshift is observed, reducing the absorption energies to 3.713 eV for the *sTDA* method and 3.708 eV for the *sTD-DFT* method. Consequently, the absorption wavelengths maxima shift to $\lambda_{abs} \simeq 333.937$ nm and 334.417 nm, respectively, though they remain within the ultraviolet range, but in the near region. Therefore, DMAC-DPS can still be classified as a UV absorber, regardless of solvation (see Table S. 7). So, in the both cases, there is no predicted color in the visible region.

When considering the emission and the Stokes shift, DMAC-DPS can be categorized as a *blue* in both environments. When solvated, while the fluorescence maxima are respectively $\lambda_{PL} \simeq 467.787$ nm and 484.417 nm for *sTDA* and *sTD-DFT* methods, the predicted color is *blue*. But, for the *sTDA* method this blue color is closer to the blue-green boundary, while for the *sTD-DFT* method this color is *blue-green* (because it falls within the blue-green region of the visible spectrum). In conclusion, DMAC-DPS can be categorized as a blue emitter. Without solvation, it exhibits characteristics of a pure *blue* emitter ($\lambda_{PL} \simeq 452.233$ nm for the both methods). Further details are shown in Figures 11 and 12(b) and table S. 7. In the CIE tables, we can connect the X, Y, and Z coordinates with the *UV-vis* with different coordinates for the color spectrum.

S.2.3 PSPCz

Figure S. 7 presents the chemical structure of PSPCz along with its 3D geometry following optimization using the *MMFF94s* force field, *xTB*, and *CREST* methods. It also shows the HOMO-LUMO gap, molecular orbitals from HOMO-1 to LUMO+2, and the electronic density maps.

The RMSD values between the three optimized structures are all below 1.7 Å, indicating that the geometries are structurally very similar (see Figure 10(c)).

Though the geometries are quite similar, it is important to note that the *xTB* and *CREST* methods do have a measurable impact on the molecular geometry derived from the *MMFF94s* method. Additionally, toluene causes a notable deviation in the molecular structure compared to the vacuum-optimized one.

As shown in Figure S. 8, the toluene-optimized structure is approximately 23.523 133 kcal mol⁻¹ lower in energy than the vacuum-optimized structure, despite their close similarity. This small structural change is sufficient to improve the energy greatly.

The values of $\Delta\epsilon_V$ and $\Delta\epsilon_T$ are both relatively small, with $\Delta\epsilon_T$ close to the threshold of chemical precision (1 kcal mol⁻¹). This indicates that the pre-optimized geometries are sufficiently accurate for further computational studies without significant loss of precision.

Molecular orbitals and HOMO-LUMO gap In both vacuum and toluene environments, the HOMO-1 is primarily localized on the Cz unit of the molecule, which implies that lower

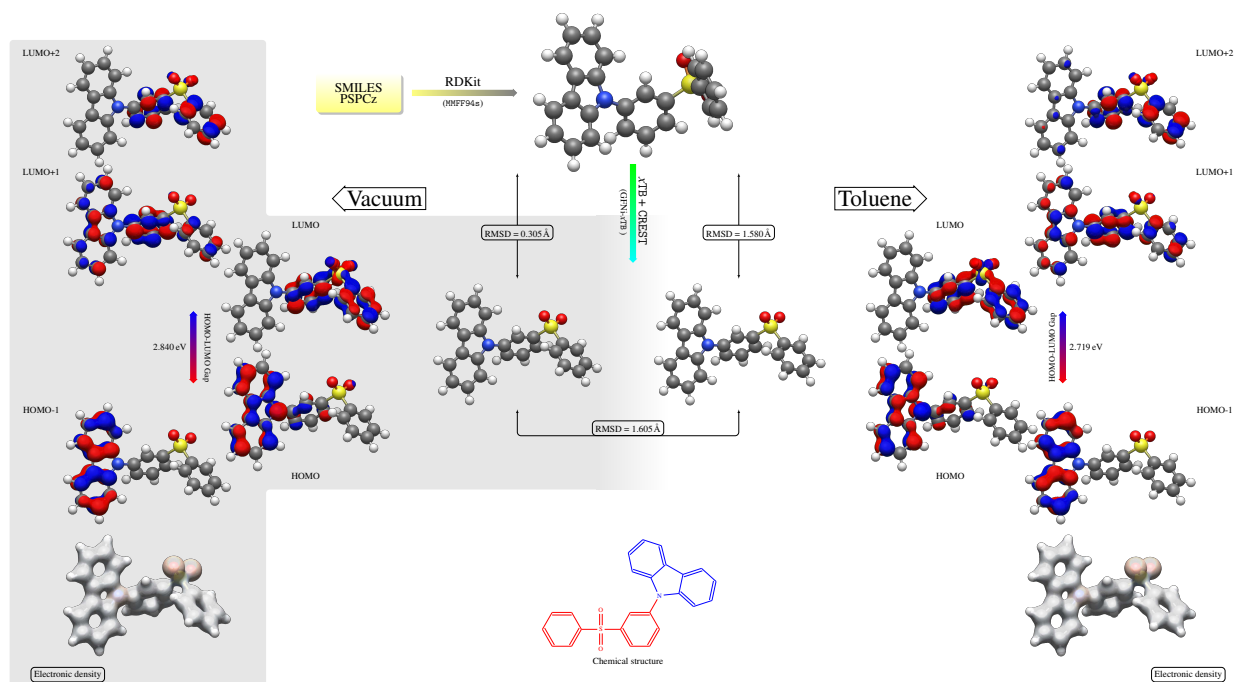


Figure S. 7 : Optimized molecular structure and electronic distributions of PSpCz. This figure displays the optimized 3D molecular structures of PSpCz in vacuum and toluene environments, calculated using the MMFF94s force field, xTB , and CREST methods. The figure also displays the corresponding molecular orbitals from HOMO-1 to LUMO+2, visualized as isodensity surfaces with blue and red indicating negative and positive regions of the wave function, respectively, and the HOMO-LUMO gap values in both environments. The comparison of electronic density maps highlights how solvation affects charge density distribution across the molecule and the interaction between PS and Cz units.

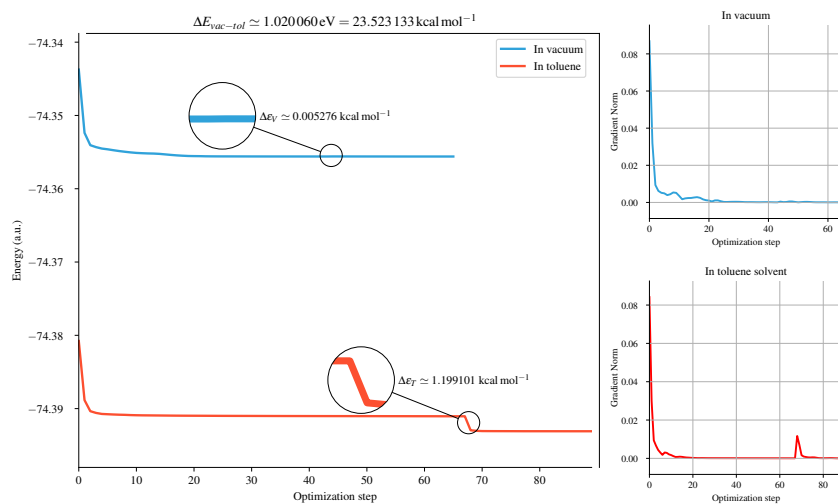


Figure S. 8 : Energy optimization process for PSpCz: vacuum vs. toluene. The left panel shows the potential energy surface explored during the geometry optimization process for PSpCz in both vacuum and toluene environments. The right panels display the gradients for vacuum (top) and toluene (bottom) optimizations. The energy difference ($\Delta E_{vac-tol} = 23.52 \text{ kcal mol}^{-1}$) highlights the significant solvent effect on the molecular stability.

energy occupied states are concentrated on the Cz part. This localization could influence the electron density and reactivity of this portion of the molecule. As with other systems,

the presence of the solvent does not significantly alter the localization of HOMO-1, suggesting that the lower energy states are relatively unaffected by the solvent environment. The LUMO+1 orbital is delocalized across both the Cz and PS units, while the LUMO+2 is largely localized on the PS unit in both environments. This indicates that the excited-state dynamics will involve both units and are expected to behave similarly in vacuum and solvent. The interaction between the Cz and PS units, suggested by this delocalization, may affect the photophysical properties of the molecule.

In both environments, the HOMO is predominantly delocalized over the Cz unit, with a significant contribution from the PS part. This delocalization suggests that there is charge transfer occurring between the Cz and PS units. Conversely, the LUMO is mainly concentrated on the PS unit, highlighting its role as the electron-accepting region. The stability of this LUMO localization across environments suggests that the electron-accepting properties of the PS unit are robust and not significantly altered by solvation.

The separation between the electron-donating (HOMO) and electron-accepting (LUMO) regions could be advantageous for processes like charge separation and recombination. The HOMO-LUMO gap varies slightly between environments, with a difference of 0.121 eV (or approximately 2.790 326 kcal mol⁻¹). This indicates that while the molecule’s geometry is relatively stable, its electronic properties are still influenced by the surrounding environment. However, the relatively large gap suggests that the molecule remains electronically stable and requires a moderate amount of energy to transition from the ground state (HOMO) to the excited state (LUMO). The electronic density maps confirm the charge distribution across the molecule, aligning with the orbital analysis.

Excitation energies In both environments, the absorption maxima wavelengths are located within the ultraviolet region. For the *s*TDA method, the absorption energy is 3.859 eV, corresponding to a wavelength of $\lambda_{abs} \simeq 322.084$ nm. For the *s*TD-DFT method, the energy is slightly lower at 3.789 eV, corresponding to a wavelength of $\lambda_{abs} \simeq 328.303$ nm. In both cases, solvation induces an anti-red shift, but the absorption wavelengths remain in the ultraviolet range, confirming PSpCz as a UV absorber (see Table S. 8).

Considering the emission and the Stokes shift, PSpCz can be classified as a *violet* emitter for both solvated and unsolvated conditions. Without solvation, PSpCz has a fluorescence wavelengths of $\lambda_{PL} \simeq 383.544$ nm and 389.325 nm for *s*TDA and *s*TD-DFT methods, respectively, but the predicted color is blue. A similar observation is made with solvation, where the wavelengths slightly shift to $\lambda_{PL} \simeq 385.613$ nm, respectively (see Figures 11 and 12(c) and table S. 8). Since there isn’t intense visible light, could this have value for other situations. Or is this a sign that it isn’t good.

S.2.4 4CzIPN

Figure S. 9 displays the chemical structure of 4CzIPN, along with the 3D structure optimized using the MMFF94s force field, *x*TB, and CREST methods. Additionally, the figure illustrates the *HOMO-LUMO* gap, the molecular orbitals from HOMO-1 to LUMO+2, and the electronic density distribution.

The RMSD between the structure optimized using the MMFF94s force field and the one obtained after optimization with *x*TB and CREST in the absence of solvent is approximately 0.7 Å. This indicates that the two structures are quite similar. However, when solvation is introduced, the RMSDs increase to values exceeding 4 Å, signifying a significant structural difference compared to both the vacuum-optimized structures (see Figure 10(d)).

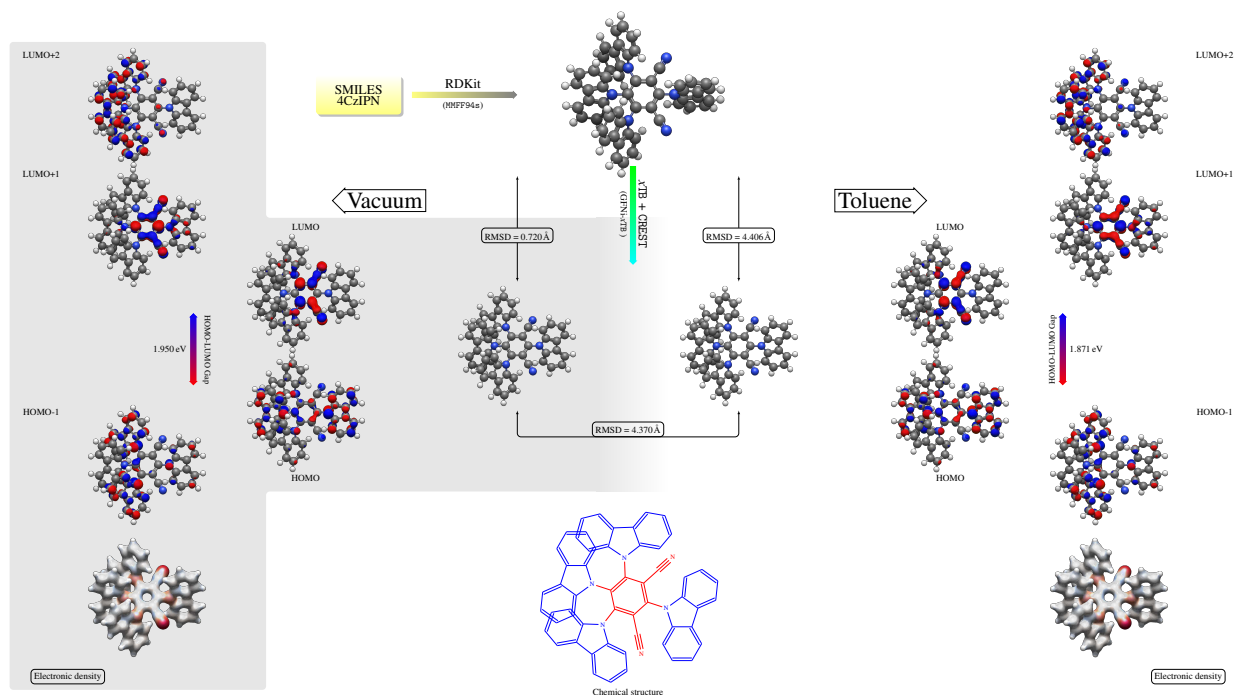


Figure S. 9 : Optimized molecular structure and electronic distributions of 4CzIPN. This figure displays the optimized 3D molecular structures of 4CzIPN in vacuum and toluene environments, calculated using the MMFF94s force field, xTB , and CREST methods. The figure also displays the corresponding molecular orbitals from HOMO-1 to LUMO+2, visualized as isodensity surfaces with blue and red indicating negative and positive regions of the wave function, respectively, and the HOMO-LUMO gap values in both environments. The comparison of electronic density maps highlights how solvation affects charge density distribution across the molecule and the interaction between IPN and Cz units. Note the delocalization of the HOMO across the four carbazole (Cz) units and the localization of the LUMO on the IPN core. Solvation appears to have a subtle effect on these distributions.

This shows there are some strong effects depending on what calculations you chose. The increase is evidence of a strong effect when toluene is present.

While the xTB and CREST methods exert a non-negligible effect on the molecular geometry derived from the MMFF94s method, the presence of toluene has an even more pronounced impact on the geometry. The most notable changes occur in the dihedral angles between the carbazole units and the central benzene ring, suggesting that the solvent promotes a more planar arrangement to maximize pi-stacking interactions.

As seen in Figure S. 10, the structure optimized in toluene is approximately $42.129\ 416\ \text{kcal mol}^{-1}$ lower in energy compared to the vacuum-optimized structure, indicating a large impact. The values of $\Delta\epsilon_V$ and $\Delta\epsilon_T$ are both very low, remaining below $0.2\ \text{kcal mol}^{-1}$. This suggests that the geometries obtained after pre-optimization are accurate enough to be used for further calculations without a significant loss of information.

Molecular orbitals and HOMO-LUMO gap In both vacuum and toluene environments, HOMO-1 is delocalized across the molecule but is more concentrated on the Cz units. This implies that the lower energy occupied states are predominantly localized on the Cz fragments, which can influence the electron density and reactivity of these regions. As shown in Figure S. 9, the solvent does not cause a significant shift in the localization of HOMO-1, indicating that the lower energy states are relatively solvent-independent.

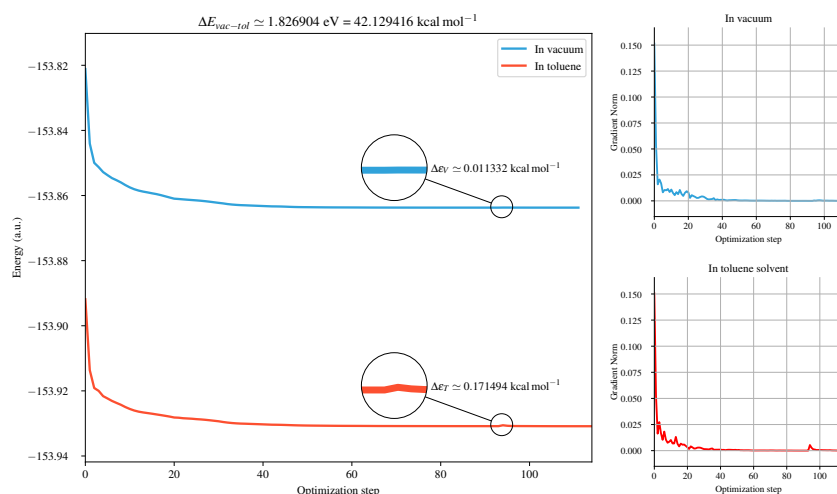


Figure S. 10 : Energy optimization process for 4CzIPN: vacuum vs. toluene. The left panel shows the potential energy surface explored during the geometry optimization process for 4CzIPN in both vacuum and toluene environments. The right panels display the gradients for vacuum (top) and toluene (bottom) optimizations. The energy difference ($\Delta E_{vac-tol} = 42.13 \text{ kcal mol}^{-1}$) highlights the significant solvent effect on the molecular stability. The smooth, rapid convergence of the toluene optimization suggests that the solvent promotes a more well-defined and stable conformation compared to the vacuum environment.

The LUMO+1 orbital is delocalized over both the Cz and IPN units, while LUMO+2 is primarily localized on the Cz fragments in both environments. This suggests that excited-state dynamics will involve both units, contributing to the photophysical properties of the molecule. Additionally, the interaction between the Cz and IPN units is evident. However, it is important to note that LUMO+1 shows a similar distribution to LUMO, with a higher delocalization over the IPN unit.

In both environments, the HOMO is delocalized across the Cz and IPN units, indicating a strong interaction between these two fragments, which can facilitate charge transfer processes. On the other hand, the LUMO is mainly localized on the IPN unit, suggesting that the electron-accepting characteristics are primarily associated with the IPN moiety. The consistent LUMO localization across environments suggests that the electron-accepting properties of IPN are stable and not significantly altered by solvation. The power is largely focused at one aspect.

The separation of electron-donating (HOMO) and electron-accepting (LUMO) regions is beneficial for charge separation and recombination, which is crucial for OLED performance. The HOMO-LUMO gap differs between environments, with a gap difference of 0.079 eV (approximately $1.821783 \text{ kcal mol}^{-1}$). This confirms that while the geometry is affected by the environment, the molecule retains a degree of electronic stability. The relatively large gap suggests that the molecule requires a moderate amount of energy to transition from the ground state (HOMO) to the excited state (LUMO). The electronic density maps corroborate the charge distribution, supporting the orbital analysis.

Excitation energies In vacuum, the maximum absorption wavelength occurs at $\lambda_{abs} \simeq 375.928 \text{ nm}$ (corresponding to 3.298 eV), placing the absorption in the near UV region for the *sTDA* method. For the *sTD-DFT* method, this maximum shifts slightly towards the visible region, with an energy of 3.268 eV and a wavelength of $\lambda_{abs} \simeq 379.335 \text{ nm}$. However, the predicted absorption color in both cases is the *blue* (see Table S. 9). Hence, in vac-

uum, 4CzIPN behaves as a blue absorber.

In the presence of toluene, the absorption wavelengths experience a red shift, moving into the visible region (see Table S. 9). The maximum absorption energies are 3.243 eV (382.367 nm) for the *sTDA* method and 3.214 eV (385.715 nm) for the *sTD-DFT* method. In this case, 4CzIPN can be classified as a *violet* absorber, but the predicted color remains blue.

Taking into account the emission and the Stokes shift, 4CzIPN is a *green* emitter in both solvated and unsolvated environments. Without solvation, the maxima are $\lambda_{PL} \simeq 499.967$ nm for the *sTDA* method and $\lambda_{PL} \simeq 504.236$ nm for the *sTD-DFT* method. In the presence of solvation, the maxima shift slightly to $\lambda_{PL} \simeq 515.994$ nm and 520.106 nm for the *sTDA* and *sTD-DFT* methods, respectively (see Figures 11 and 12(d) and table S. 9).

S.2.5 Px2BP

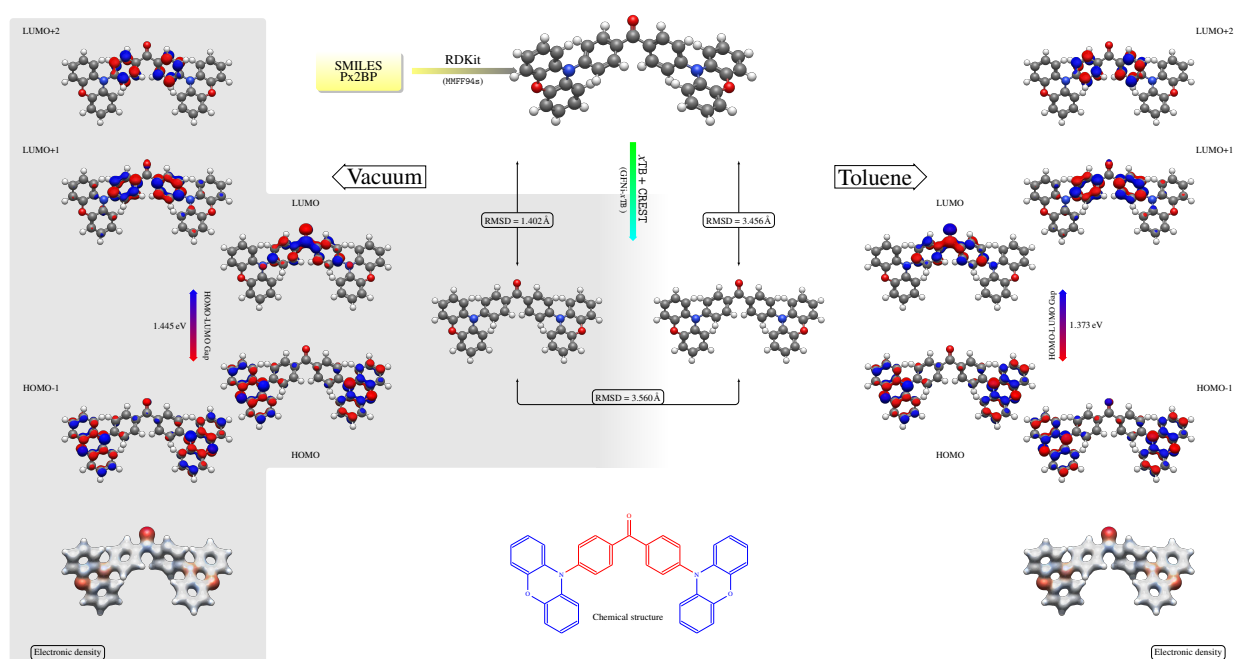


Figure S. 11 : Optimized 3D molecular structures and electronic distributions of Px2BP. This figure displays the optimized 3D molecular structures of Px2BP in vacuum and toluene environments, calculated using the MMFF94s force field, *xTB*, and CREST methods. The figure also displays the corresponding molecular orbitals from HOMO-1 to LUMO+2, visualized as isodensity surfaces with blue and red indicating negative and positive regions of the wave function, respectively, and the HOMO-LUMO gap values in both environments. The comparison of electronic density maps highlights how solvation affects charge density distribution across the molecule and the interaction between PXZ and BP units. Does this data suggest to what extent is there charge transfer from PXZ and BP.

Figure S. 11 illustrates the chemical structure of Px2BP, alongside its 3D optimized geometry obtained through the MMFF94s force field, *xTB*, and CREST methods. Additionally, the figure provides information on the HOMO-LUMO gap, molecular orbitals from HOMO-1 to LUMO+2, and electronic density distribution in vacuum and solvated conditions.

The RMSD between the vacuum-optimized structure using MMFF94s and those obtained with *xTB* and CREST methods is approximately 1.4 Å. This deviation indicates a measurable alteration in molecular geometry. However, the introduction of solvation leads to a signifi-

cant increase in RMSD values, exceeding 3 Å, as shown in Figure 10(e). This highlights a considerable impact of the solvent on the molecular structure.

The energy difference between the vacuum- and toluene-optimized structures further demonstrates the solvent’s stabilizing effect. The toluene-optimized structure is approximately 28.82 kcal mol⁻¹ lower in energy, as depicted in Figure S. 12 . This confirms that solvation significantly enhances the molecular stability.

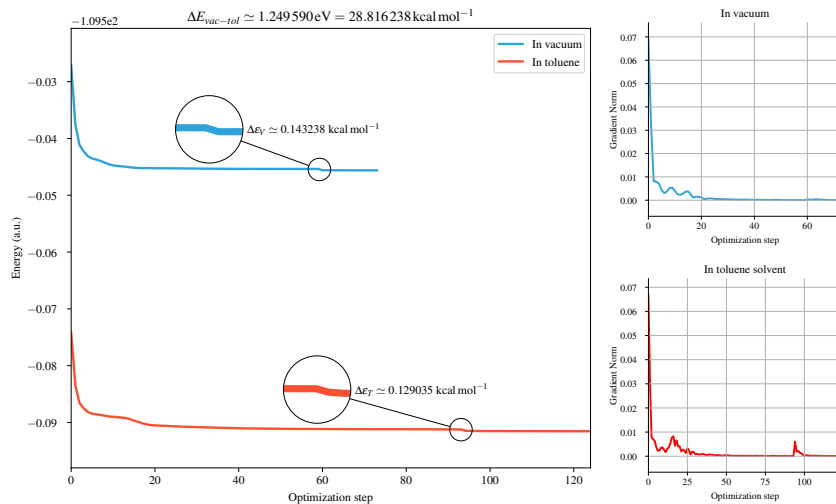


Figure S. 12 : Energy optimization process for Px2BP: vacuum vs. toluene. The left panel shows the potential energy surface explored during the geometry optimization process for Px2BP in both vacuum and toluene environments. The energy difference ($\Delta E_{vac-tol} = 28.82$ kcal mol⁻¹) between the vacuum- and toluene-optimized structures highlights the solvent’s significant impact on molecular stability.

The small values of $\Delta\epsilon_V$ and $\Delta\epsilon_T$, both below 0.15 kcal mol⁻¹, confirm that the pre-optimized geometries are sufficiently accurate for subsequent calculations with minimal loss of precision.

Molecular orbitals and HOMO-LUMO gap In both vacuum and toluene environments, the molecular orbitals of Px2BP display distinct localization patterns. The HOMO-1 is delocalized across the molecule, with a dominant concentration on the PXZ units, signifying that the lower-energy occupied states primarily reside on these fragments. The solvent environment does not significantly alter this localization, as shown in Figure S. 11 , suggesting that these states are relatively environment-independent.

The LUMO+1 and LUMO+2 orbitals exhibit delocalization over the BP component, indicating that excited-state dynamics involve both BP and PXZ units. This delocalization enhances the molecule’s photophysical properties. The HOMO is strongly delocalized across both PXZ and BP, facilitating charge transfer processes, while the LUMO is primarily localized on BP, consistent across environments. This separation of electron-donating and electron-accepting regions is advantageous for charge separation and recombination, which are critical for applications such as organic light-emitting diodes (OLEDs).

The HOMO-LUMO gap changes between environments, with a difference of 0.072 eV (approximately 1.660 359 kcal mol⁻¹). This indicates that solvation slightly affects the electronic properties but maintains the molecule’s electronic stability. The relatively large gap suggests a moderate energy requirement for electronic transitions from the ground state (HOMO) to the excited state (LUMO).

Excitation energies Px2BP demonstrates blue absorption characteristics in both environments, as predicted by absorption calculations. In vacuum, the maximum absorption wavelength is $\lambda_{abs} \simeq 425.93$ nm (2.91 eV) using the *sTDA* method, and $\lambda_{abs} \simeq 430.68$ nm (2.88 eV) with *sTD-DFT*. Solvation induces a minor anti-red shift, with the maximum absorption wavelength shifting to $\lambda_{abs} \simeq 415.89$ nm (2.98 eV) for *sTDA* and $\lambda_{abs} \simeq 419.98$ nm (2.95 eV) for *sTD-DFT*. These results confirm Px2BP as a blue absorber in both environments. The trend for the *sTDA* and *sTD-DFT* is that the wavelengths are very close. This is a trend for Px2BP.

Accounting for the emission with the Stokes shift, Px2BP is a blue emitter at the lower bound of the emission spectrum. However, at the upper bound, the fluorescence maxima shift into the yellow region, with wavelengths of $\lambda_{PL} \simeq 575.93$ nm and 580.68 nm for *sTDA* and *sTD-DFT*, respectively, in vacuum. In toluene solvent, these maxima slightly shift to $\lambda_{PL} \simeq 565.89$ nm and 569.98 nm (see Table S. 10). Therefore, we can classify Px2BP as an interesting molecule. What happens with it makes it unique and may be helpful.

S.2.6 CzS2

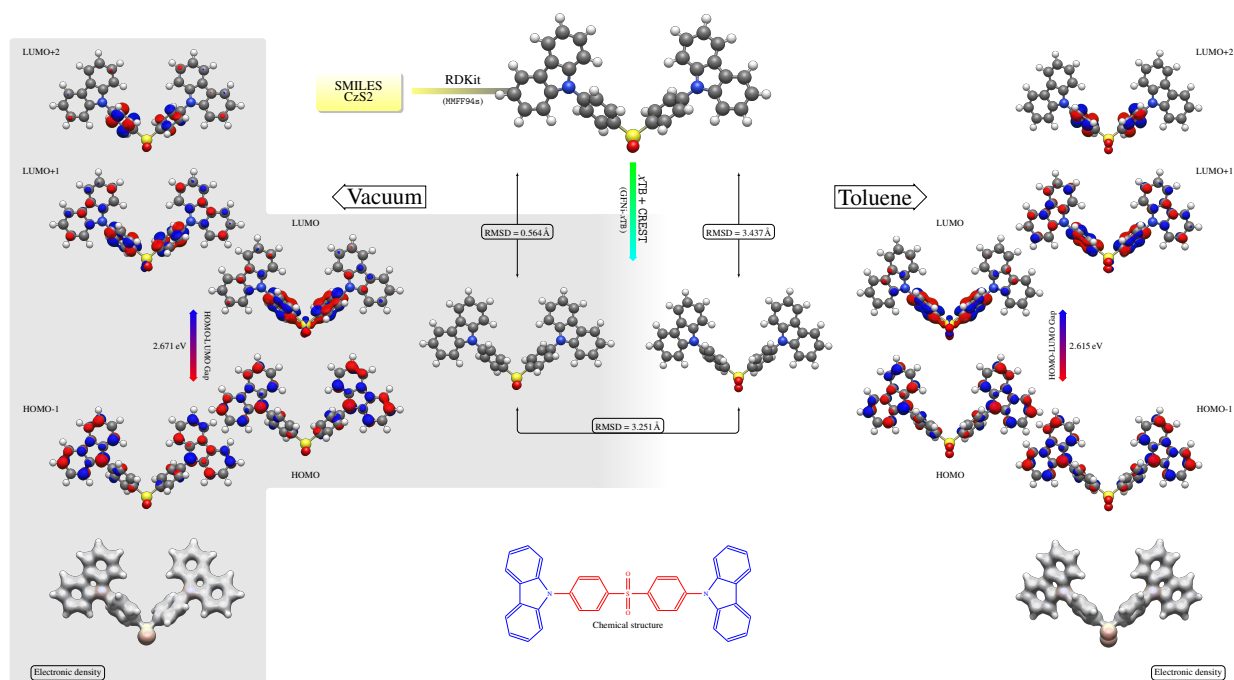


Figure S. 13 : Optimized 3D molecular structures and electronic distributions of CzS2. This figure displays the optimized 3D molecular structures of CzS2 in vacuum and toluene environments, calculated using the MMFF94s force field, *xTB*, and CREST methods. The figure also displays the corresponding molecular orbitals from HOMO-1 to LUMO+2, along with the HOMO-LUMO gap values in both environments. The electronic density maps illustrate the impact of solvation on charge density distribution across the molecule and the interaction between Cz and PS units.

Figure S. 13 provides a detailed visualization of the CzS2 molecule, including its 3D geometry optimized using the MMFF94s force field, *xTB*, and CREST methods. Additionally, it presents the calculated *HOMO-LUMO* gap, molecular orbitals (HOMO-1 to LUMO+2), and electronic density maps under both vacuum and solvated conditions. These results highlight the interplay between molecular structure and electronic properties in different

environments.

The RMSD between the vacuum-optimized CzS2 geometry obtained using the **MMFF94s** force field and those optimized with *xTB* and **CREST** is approximately 0.5 Å. This indicates a slight structural deviation between the methods in the absence of solvent. However, the introduction of solvation (toluene) leads to a more pronounced structural change, with RMSD values exceeding 3.2 Å, as shown in Figure 10(f). This significant difference highlights the solvent’s substantial influence on the molecular structure.

Despite these structural differences, the energy comparison between the vacuum- and toluene-optimized structures reveals that the solvent-stabilized geometry is approximately 31.88 kcal mol⁻¹ lower in energy (Figure S. 14). This energy difference underscores the stabilizing effect of solvation on CzS2, even though the geometries deviate significantly.

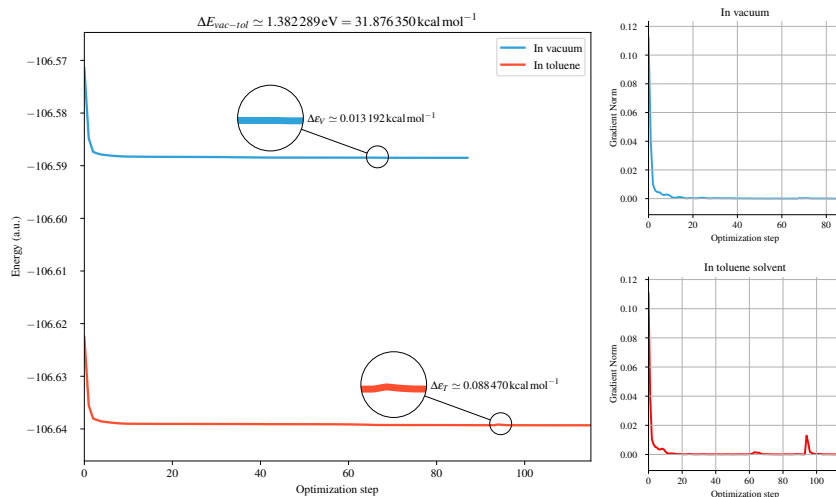


Figure S. 14 : Energy optimization process for CzS2: vacuum vs. toluene. The left panel shows the potential energy surface explored during the geometry optimization process for CzS2 in both vacuum and toluene environments. The right panels display the gradients for vacuum (top) and toluene (bottom) optimizations. The energy difference ($\Delta E_{vac-tol} = 31.88 \text{ kcal mol}^{-1}$) highlights the significant solvent effect on molecular stability. Here, a rapid initial drop in energy indicates that a few steps were needed before the molecule began to adjust.

The small values of $\Delta\epsilon_V$ and $\Delta\epsilon_T$, both below 0.09 kcal mol⁻¹, confirm that the pre-optimized geometries are sufficiently accurate for subsequent computations, preserving precision.

Molecular orbitals and HOMO-LUMO gap In both vacuum and toluene environments, the HOMO-1 orbital of CzS2 is delocalized across the molecule, with a strong localization on the Cz units. This suggests that the lower-energy occupied states are primarily associated with the Cz regions, influencing their electron density and reactivity. Solvation does not significantly alter this localization, indicating that these states are relatively environment-independent.

The LUMO+1 orbital is delocalized across both the Cz and PS units, while the LUMO+2 is localized predominantly on the DPS unit. This distribution suggests that excited-state dynamics involve contributions from both Cz and PS units, resulting in consistent behavior across environments. The interaction between these units may also play a role in the photophysical properties of CzS2.

The HOMO is predominantly delocalized over the Cz units, with a minor but notable contribution from the DPS units, indicating charge transfer between the two regions. Con-

versely, the LUMO is primarily localized on the DPS unit, establishing it as the primary electron-accepting region. This separation of the electron-donating (Cz) and electron-accepting (PS) regions is advantageous for applications requiring efficient charge separation and recombination.

The HOMO-LUMO gap exhibits a slight variation between environments, with a difference of 0.056 eV (approximately 1.29 kcal mol⁻¹). While this confirms that CzS2's geometry is stable, it also suggests that its electronic properties are subtly influenced by solvation. The relatively large gap signifies electronic stability and indicates a moderate energy requirement for electronic transitions from the ground state (HOMO) to the excited state (LUMO). Therefore, a lot of force is required.

Excitation energies CzS2 exhibits absorption maxima in the ultraviolet (UV) region under both vacuum and solvated conditions. Using the *s*TDA method, the absorption energy is calculated as 3.902 eV, corresponding to a wavelength of $\lambda_{abs} \simeq 317.7$ nm. The *s*TD-DFT method predicts a slightly lower energy of 3.839 eV, corresponding to a wavelength of $\lambda_{abs} \simeq 322.9$ nm. Solvation induces an anti-red shift, as observed in similar systems, while the wavelengths remain within the UV range, confirming CzS2 as a UV absorber (Table S. 11). There aren't a lot of changes for each of the environments. This is unlike the DMAC-TRZ where it shifts with the solvent.

When considering the emission with the Stokes shift, CzS2 can be classified as a UV emitter at the lower bound. At the upper bound, in the absence of solvation, CzS2 exhibits blue emission characteristics, with fluorescence maxima at $\lambda_{PL} \simeq 467.7$ nm and 472.9 nm for the *s*TDA and *s*TD-DFT methods, respectively. With solvation, these maxima shift slightly to $\lambda_{PL} \simeq 466.4$ nm and 471.4 nm. The wavelength difference between the two methods is approximately 5 nm, equivalent to 1.45 kcal mol⁻¹ (Figure 12(f)). Since, with solvation, the wavelength remains the same and consistent, then this configuration may not help promote a range of potential colors

S.2.7 2TCz-DPS

Figure S. 15 presents the chemical structure of 2TCz-DPS and its 3D geometry optimized using the MMFF94s force field, *x*TB, and CREST methods. Additionally, it includes the calculated *HOMO-LUMO* gap, molecular orbitals from HOMO-1 to LUMO+2, and electronic density maps under both vacuum and solvated conditions. These results demonstrate the influence of solvation on molecular geometry and electronic properties.

The RMSD values between the optimized geometries for 2TCz-DPS are all above 2 Å, indicating significant structural differences between the optimization methods and environments (see Figure 10(g)).

Both the *x*TB and CREST methods induce noticeable changes in the molecular geometry compared to the MMFF94s-optimized structure.

As shown in Figure S. 16, the toluene-optimized structure is approximately 45.75 kcal mol⁻¹ lower in energy than the vacuum-optimized structure. This substantial energy difference highlights the stabilizing effect of solvation.

The small values of $\Delta\epsilon_V$ and $\Delta\epsilon_T$, both below 0.8 kcal mol⁻¹, confirm that the pre-optimized geometries are sufficiently accurate for further computational studies without significant loss of precision.

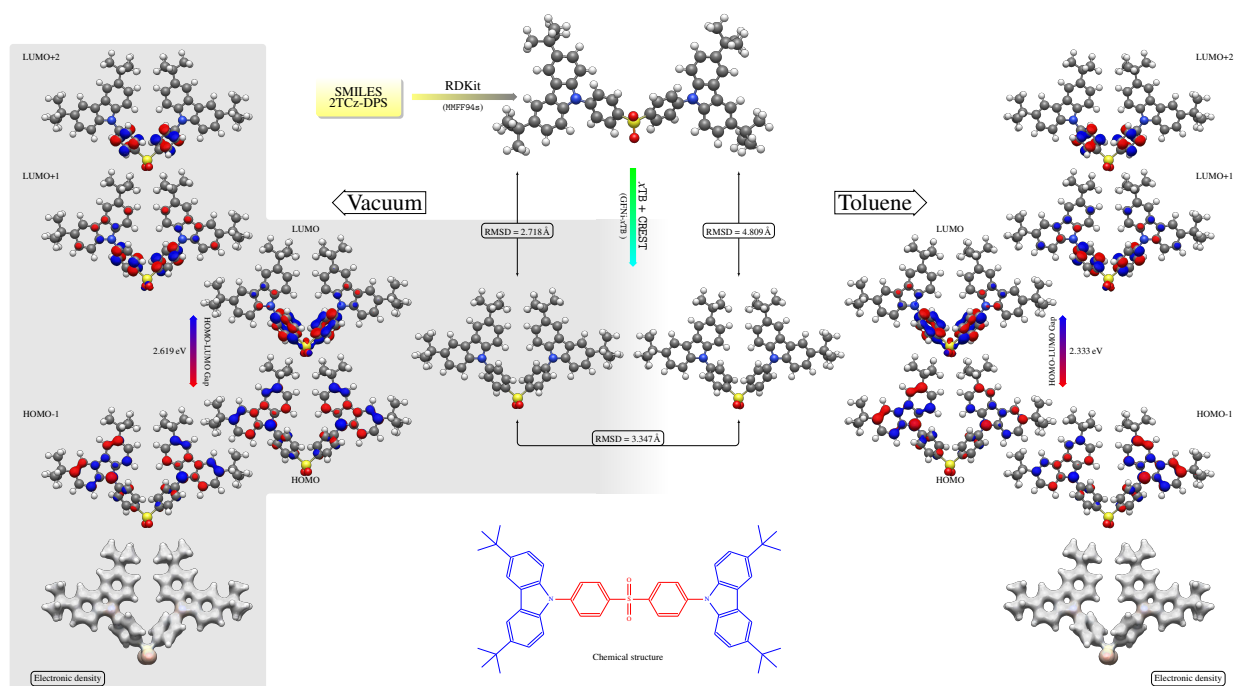


Figure S. 15 : Optimized 3D molecular structures and electronic distributions of 2TCz-DPS. This figure displays the optimized 3D molecular structures of 2TCz-DPS in vacuum and toluene environments, calculated using the MMFF94s force field, *xTB*, and CREST methods. The figure also displays the corresponding molecular orbitals from HOMO-1 to LUMO+2, along with the HOMO-LUMO gap values in both environments. The comparison of electronic density maps highlights how solvation affects charge density distribution across the molecule and the interaction between TCz and PS units.

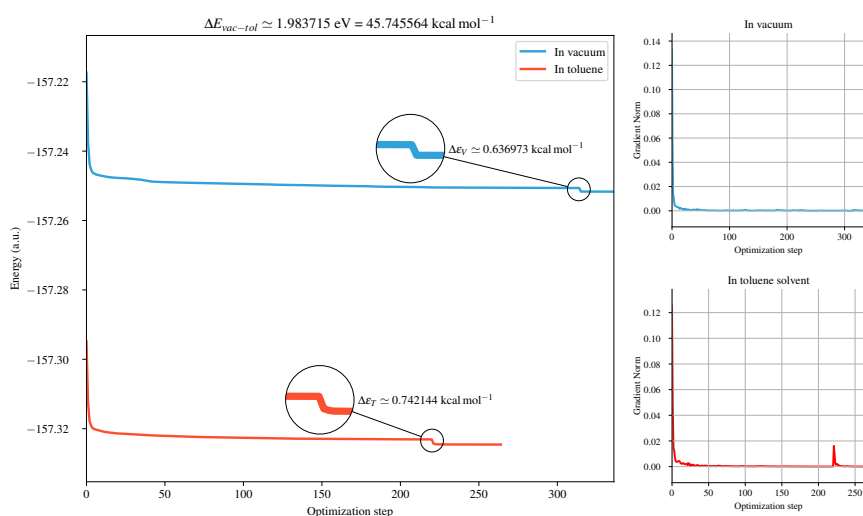


Figure S. 16 : Energy optimization process for 2TCz-DPS: vacuum vs. toluene. The left panel shows the potential energy surface explored during the geometry optimization process for 2TCz-DPS in both vacuum and toluene environments. The energy difference ($\Delta E_{vac-tol} = 45.75 \text{ kcal mol}^{-1}$) highlights the significant solvent effect on molecular stability. The gradient plots further illustrate the impact of the solvent on the optimization process.

Molecular orbitals and HOMO-LUMO gap In both vacuum and toluene environments, the HOMO-1 orbital of 2TCz-DPS is delocalized across the molecule, with strong localization

on the TCz units. This suggests that the lower-energy occupied states are primarily associated with the TCz regions, which could influence their electron density and reactivity. The presence of the solvent does not significantly alter the localization of HOMO-1, indicating that these states remain relatively unaffected by solvation.

The LUMO+1 orbital is delocalized across both the TCz and PS units, while the LUMO+2 is predominantly localized on the DPS unit in both environments. This distribution indicates that excited-state dynamics involve contributions from both TCz and PS units, with similar behavior expected in vacuum and solvated conditions. The interaction between these units, as suggested by the delocalization, may play a role in determining the photophysical properties of the molecule.

The HOMO is predominantly delocalized over the TCz units, with a minor but notable contribution from the DPS region. This delocalization suggests charge transfer between the TCz and PS units. Conversely, the LUMO is largely localized on the PS unit, establishing it as the primary electron-accepting region. The stability of this LUMO localization across environments indicates that the electron-accepting properties of the PS unit are robust and not significantly affected by solvation.

The separation between the electron-donating (HOMO) and electron-accepting (LUMO) regions could enable efficient charge transfer processes, such as charge separation and recombination. The HOMO-LUMO gap varies slightly between environments, with a difference of 0.079 eV (approximately 1.821 783 kcal mol⁻¹). This confirms that while the geometry is affected by the environment, the molecule retains a degree of electronic stability. However, the relatively large gap suggests that the molecule requires a moderate amount of energy for transitions from the ground state (HOMO) to the excited state (LUMO).

Excitation energies In both environments, 2TCz-DPS exhibits absorption maxima in the ultraviolet (UV) region. Solvation induces an anti-red shift, similar to what is observed in PSPCz and CzS2, while the absorption wavelengths remain in the UV range, confirming 2TCz-DPS as a UV absorber (see Tables 1, 2 and S. 12 for detailed data).

Considering the emission with the Stokes shift, 2TCz-DPS is classified as a UV emitter at the lower bound in both solvated and unsolvated conditions. At the upper bound, without solvation, 2TCz-DPS shows blue emission characteristics, with fluorescence maxima at $\lambda_{PL} \simeq 470.07$ nm and 475.53 nm for the *s*TDA and *s*TD-DFT methods, respectively. Under solvated conditions, the maxima shift slightly to $\lambda_{PL} \simeq 468.69$ nm and 473.68 nm. The wavelength difference between the two methods is approximately 5 nm, equivalent to 1.45 kcal mol⁻¹ (Figure 12(g)). This demonstrates there is a consistent result with the upper and lower bounds.

S.2.8 TDBA-DI

Figure S. 17 shows the chemical structure of TDBA-DI, along with the 3D structure optimized using the MMFF94s force field, *x*TB, and CREST methods. Additionally, the figure illustrates the *HOMO-LUMO* gap, the molecular orbitals from HOMO-1 to LUMO+2, and the electronic density distribution.

The RMSD between the structure optimized using the MMFF94s force field and the one obtained after optimization with *x*TB and CREST with the solvent is approximately 1.25 Å, which is the lowest among the three. This indicates that the structure obtained with solvent is quite similar to the one obtained using the MMFF94s force field. However, without

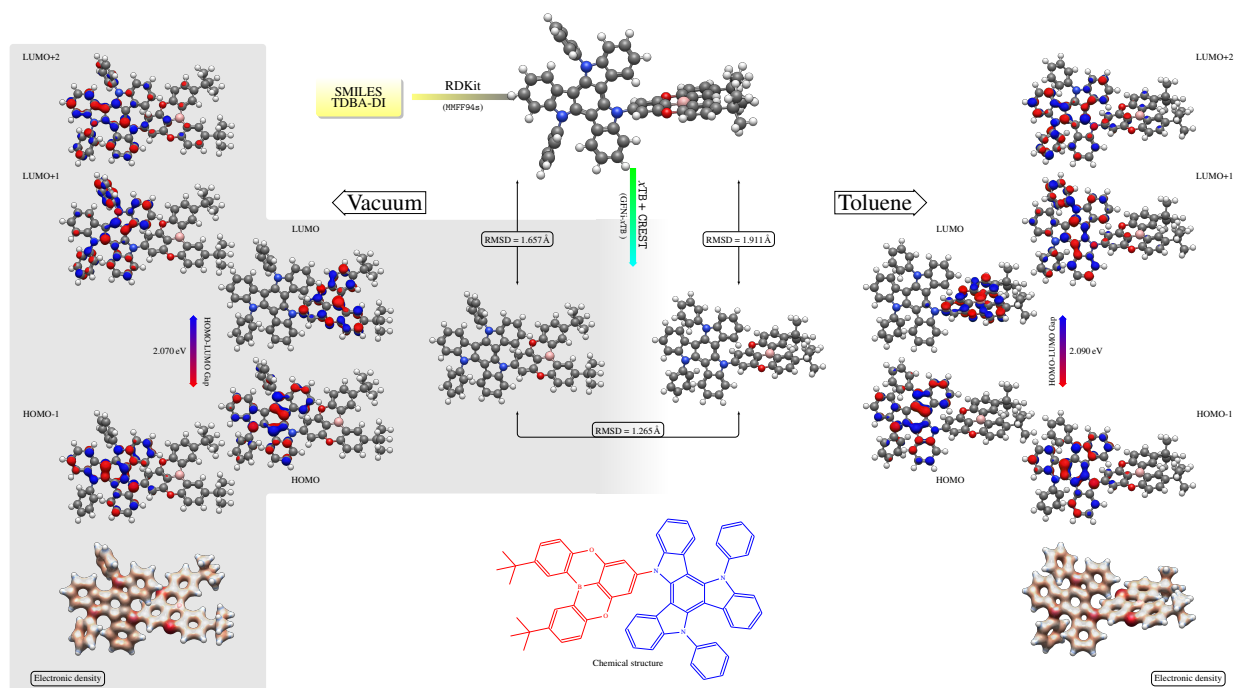


Figure S. 17 : Optimized 3D molecular structures of TDBA-DI in vacuum and toluene environments, calculated using the MMFF94s force field, *xTB*, and CREST. The figure also displays the corresponding molecular orbitals from HOMO-1 to LUMO+2, visualized as isodensity surfaces with blue and red indicating negative and positive regions of the wave function, respectively, and the HOMO-LUMO gap values in both environments. The comparison of electronic density maps highlights how solvation affects charge density distribution across the molecule and the interaction between TD and BA-DI units.

solvation, the RMSDs increase to values exceeding 1.5 Å but below 2 Å, signifying a significant structural difference compared to MMFF94s- and toluene-optimized structures (see Figure 10(h)).

While the *xTB* and CREST methods exert a non-negligible effect on the molecular geometry derived from the MMFF94s method, the absence of toluene has an even more pronounced impact on the geometry.

As seen in Figure S. 18, the structure optimized in toluene is approximately 45.002 901 1 kcal mol⁻¹ lower in energy compared to the vacuum-optimized structure. This is a very large difference, and the best.

The small values of $\Delta\epsilon_V$ and $\Delta\epsilon_T$ (both below 0.3 kcal mol⁻¹) indicate that the pre-optimized geometries are sufficiently accurate for subsequent calculations.

Molecular orbitals and HOMO-LUMO gap In both vacuum and toluene environments, HOMO-1 is delocalized across the molecule but is more concentrated on the BA-DI unit. This implies that the lower energy occupied states are predominantly localized on the BA-DI fragment, which can influence the electron density and reactivity of this region. As shown in Figure S. 17, the solvent does not cause a significant shift in the localization of HOMO-1, indicating that the lower energy states are relatively solvent-independent. The LUMO+1 and LUMO+2 orbitals are delocalized over both the BA-DI and TD units in both environments, but are more localized on the TD fragment. This suggests that excited-state dynamics will involve both units, contributing to the photophysical properties of the molecule. Additionally, the interaction between the BA-DI and TD units is

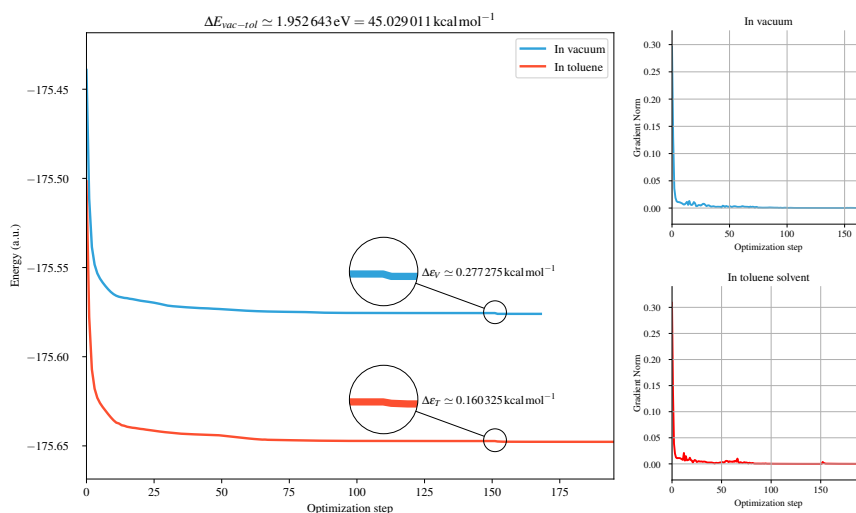


Figure S. 18 : Energy optimization process for TDBA-DI: vacuum vs. toluene. The left panel shows the potential energy surface explored during the geometry optimization process for TDBA-DI in both vacuum and toluene environments. The energy difference ($\Delta E_{vac-tol} = 42.13 \text{ kcal mol}^{-1}$) highlights the significant solvent effect on the molecular stability. The gradients of both optimizations emphasize the solvent's impact on the optimization process.

evident.

In both environments, the HOMO is primarily localized on the BA-DI unit, suggesting that the electron-donating characteristics are primarily associated with the BA-DI moiety. On the other hand, the LUMO is mainly localized on the TD unit, suggesting that the electron-accepting characteristics are primarily associated with the TD moiety. The consistent HOMO and LUMO localization across environments suggests that the electron-donating properties of BA-DI and electron-accepting properties of TD are stable and not significantly altered by solvation.

The separation of electron-donating (HOMO) and electron-accepting (LUMO) regions is beneficial for charge separation and recombination, which is crucial for OLED performance. The HOMO-LUMO gap exhibits a solvent-dependent variation of 0.020 eV (approximately $0.461211 \text{ kcal mol}^{-1}$). This confirms that while the geometry is affected by the environment, the molecule remains electronically stable. The relatively large gap suggests that the molecule requires a moderate amount of energy to transition from the ground state (HOMO) to the excited state (LUMO).

Excitation energies In vacuum, the maximum absorption wavelength occurs at $\lambda_{abs} \simeq 347.0120 \text{ nm}$ (corresponding to 3.573 eV), placing the absorption in the ultraviolet region for the *sTDA* method. For the *sTD-DFT* method, this maximum stays in the ultraviolet region, with an energy of 3.502 eV and a wavelength of $\lambda_{abs} \simeq 354.0573 \text{ nm}$. However, the predicted color in both cases is *blue* (see Table S. 13). Hence, in vacuum, TDBA-DI behaves as a blue absorber.

In the presence of toluene, the absorption wavelengths experience a red shift for the *sTDA* method and an anti-red shift for the *sTD-DFT* method, and stay in the ultraviolet region (see Table S. 13). The maximum absorption energies are 3.564 eV ($\lambda_{abs} \simeq 347.9288 \text{ nm}$) for the *sTDA* method and 3.508 eV ($\lambda_{abs} \simeq 353.4456 \text{ nm}$) for the *sTD-DFT* method. Based on the predicted color, TDBA-DI can be classified as a blue absorber in this case also.

Taking into account the emission with the Stokes shift, TDBA-DI is a blue emitter when considering the lower bound of the emission spectrum in both solvated and unsolvated environments, although the maxima stay in UV region. Without solvation, the maxima are $\lambda_{PL} \simeq 357.0120$ nm for the *s*TDA method and $\lambda_{PL} \simeq 364.0573$ nm for the *s*TD-DFT method. In the presence of solvation, the maxima shift slightly to $\lambda_{PL} \simeq 357.9288$ nm and 363.4456 nm for the *s*TDA and *s*TD-DFT methods, respectively.

At the upper bound of the spectrum, TDBA-DI exhibits green emission characteristics, confirmed by the predicted color, both with and without solvation. The fluorescence maxima at the upper bound are $\lambda_{PL} \simeq 497.0120$ nm and 504.0573 nm for the *s*TDA and *s*TD-DFT methods, respectively. With solvation, the maxima shift to $\lambda_{PL} \simeq 497.9288$ nm and 503.4456 nm for the *s*TDA and *s*TD-DFT methods, respectively. We see also here that, the difference in wavelengths obtained using the two methods is approximately 6 nm, which is equivalent to 1.61423837 kcal mol⁻¹ (see Figures 11 and 12(h) and table S. 13).

S.3 Detailed UV-Vis, ECD spectrum, and chromatogram results

This section provides detailed data supporting the analysis of UV-Vis absorption, Electronic Circular Dichroism (ECD), and color properties for each molecule.

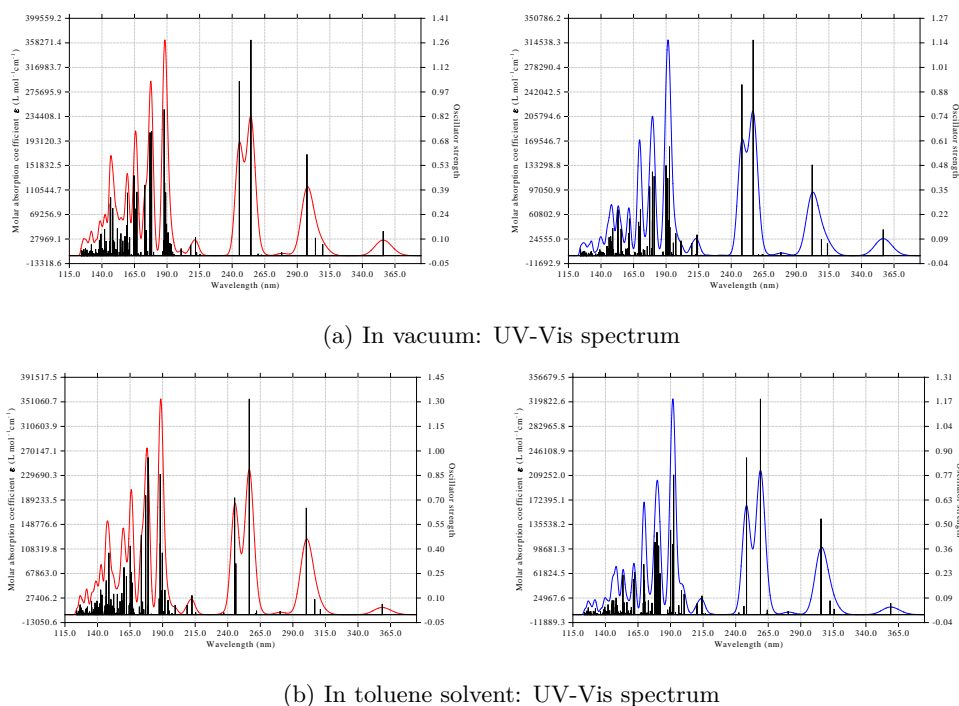


Figure S. 19 : UV-Vis absorption spectra of DMAC-TRZ: solvent and method dependence. Panels show the simulated UV-Vis absorption spectra in vacuum and toluene, calculated with *s*TDA (top) and *s*TD-DFT (bottom) methods. Note the slight redshift in the absorption maximum upon solvation, indicating a stabilization of the ground state in the polar solvent.

S.4 Approximation of the TADF efficiency

To calculate the TADF efficiency, we need to consider the radiative and non-radiative decay rates of the singlet and triplet states. The TADF efficiency (η_{TADF} derived from [27])

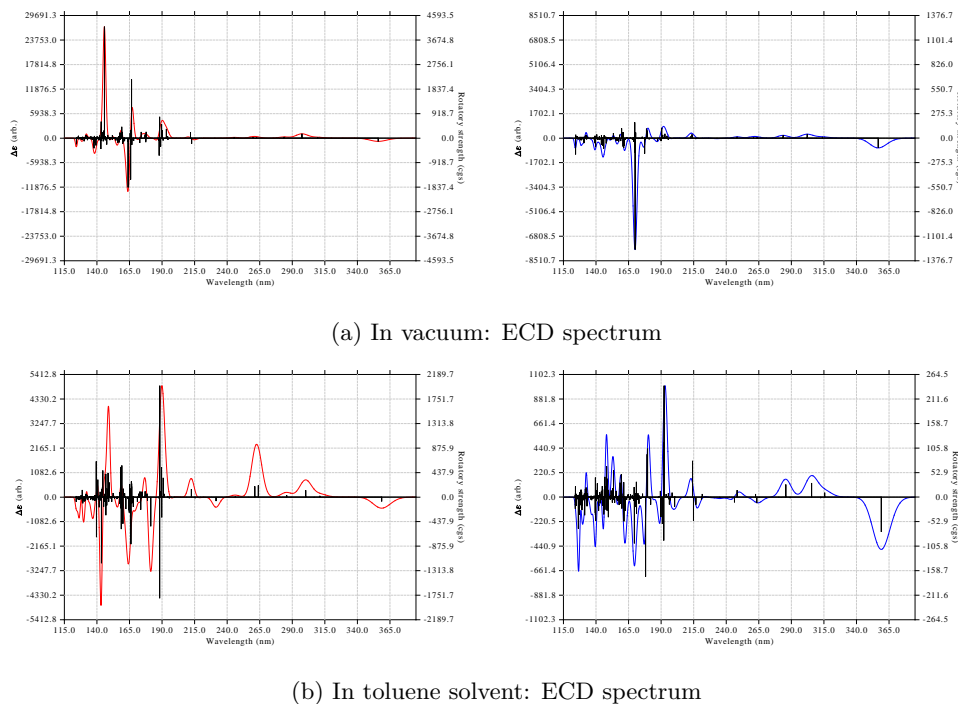


Figure S. 20 : Electronic Circular Dichroism (ECD) spectra of DMAC-TRZ: solvent and method dependence. Panels show the simulated ECD spectra in vacuum and toluene, calculated with *sTDA* (top) and *sTD-DFT* (bottom) methods. The ECD spectra indicate a lack of significant chiral character in DMAC-TRZ, with relatively weak signals observed across the UV-Vis region.

Table S. 6 : Colorimetric properties of DMAC-TRZ: wavelength maxima and CIE coordinates. This table summarizes the key colorimetric properties of DMAC-TRZ, including the wavelengths of maximum absorption and emission, CIE 1931 color space coordinates (*X*, *Y*, *Z* and *x*, *y*), and approximate sRGB color representation. The predicted emission color shifts from greenish-yellow to yellowish-green upon solvation, suggesting a potential for solvatochromic color tuning.

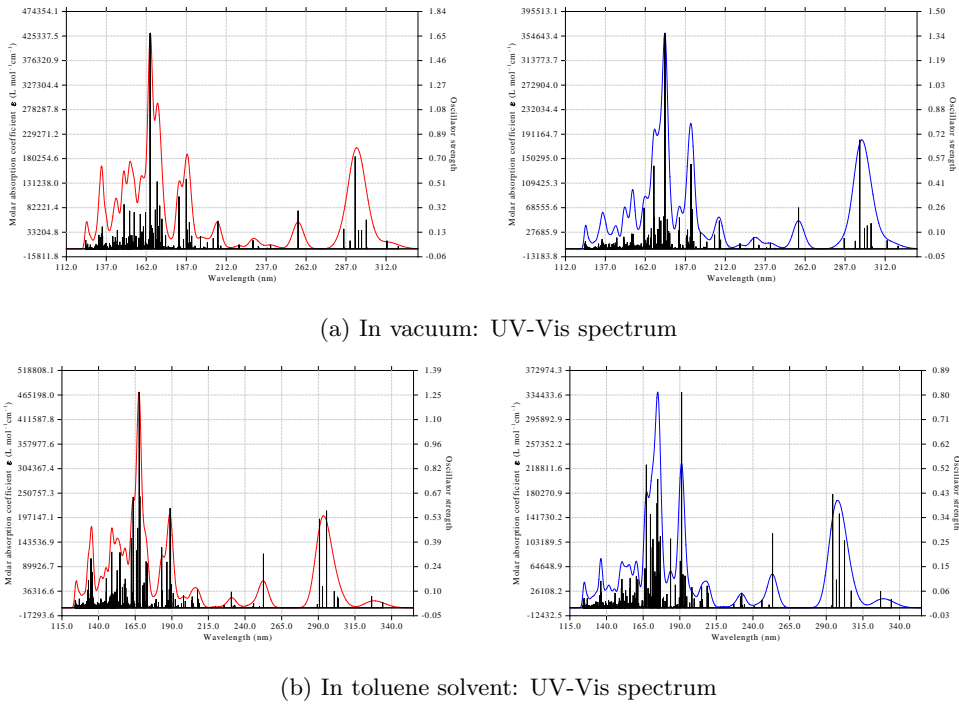
		Properties λ_{max} (nm)		(<i>X</i> , <i>Y</i> , <i>Z</i>)	(<i>x</i> , <i>y</i>)	(R,G,B)
In vacuum	<i>UV-vis</i> absorption	<i>sTDA</i>	356.0102	(29.989777, 0.898637, 140.361012)	(0.1751233707, 0.0052475336)	(47,0,255)
		<i>sTD-DFT</i>	356.6809	(33.599252, 1.006304, 157.281498)	(0.1750991105, 0.0052442520)	(47,0,255)
	Fluorescence	<i>sTDA</i>	566.8904	(306071.535496, 410870.815619, 1184.586455)	(0.4262081249, 0.5721423249)	(223,255,0)
		<i>sTD-DFT</i>	565.3394	(284799.849867, 399008.601886, 1254.693214)	(0.4157278814, 0.5824406185)	(197,255,0)
In toluene solvent	<i>UV-vis</i> absorption	<i>sTDA</i>	358.6689	(23.304646, 0.696829, 109.149006)	(0.1750248730, 0.0052333967)	(47,0,255)
		<i>sTD-DFT</i>	359.0723	(24.373392, 0.728489, 114.168213)	(0.1750080819, 0.0052307642)	(47,0,255)
	Fluorescence	<i>sTDA</i>	579.9337	(177983.977016, 168226.115675, 315.770987)	(0.5136239331, 0.4854648190)	(255,205,0)
		<i>sTD-DFT</i>	572.4365	(152547.983094, 175637.856871, 398.933337)	(0.4642576147, 0.5345282896)	(255,255,0)

is typically calculated using the following formula:

$$\eta_{\text{TADF}} = \frac{k_{\text{rISC}} \cdot \Phi_{\text{PF}}}{k_{\text{rISC}} + k_{\text{ISC}} + k_{\text{nr}}}, \quad (1)$$

where,

- k_{rISC} is the rate constant for reverse intersystem crossing (rISC) from the triplet state (T_1) to the singlet state (S_1);
- k_{ISC} is the rate constant for intersystem crossing (ISC) from the singlet state (S_1) to the triplet state (T_1);
- k_{nr} is the non-radiative decay rate;



(a) In vacuum: UV-Vis spectrum

(b) In toluene solvent: UV-Vis spectrum

Figure S. 21 : UV-Vis absorption spectra of DMAC-DPS: solvent and method dependence. Panels show the simulated UV-Vis absorption spectra in vacuum and toluene, calculated with *sTDA* (top) and *sTD-DFT* (bottom) methods. Note the significant broadening of the absorption band in toluene, suggesting increased vibronic coupling in the polar environment.

Table S. 7 : Colorimetric properties of DMAC-DPS: wavelength maxima and CIE coordinates. This table summarizes the key colorimetric properties of DMAC-DPS, including the wavelengths of maximum absorption and emission, CIE 1931 color space coordinates (X , Y , Z and x , y), and approximate sRGB color representation. The predicted emission color shifts significantly from blue to blue-green upon solvation, indicating a strong solvatochromic effect driven by its highly polar excited state.

		Properties λ_{max} (nm)		(X , Y , Z)	(x , y)	(R,G,B)
In vacuum	UV-vis absorption	<i>sTDA</i>	319.6899	NA	NA	NA
		<i>sTD-DFT</i>	320.1434	NA	NA	NA
	Fluorescence	<i>sTDA</i>	452.2331	(15819.013282, 2143.225893, 85161.533309)	(0.1533983184, 0.0207830439)	(17,0,255)
		<i>sTD-DFT</i>	452.2331	(15819.013282, 2143.225893, 85161.533309)	(0.1533983184, 0.0207830439)	(17,0,255)
In toluene solvent	UV-vis absorption	<i>sTDA</i>	333.9365	NA	NA	NA
		<i>sTD-DFT</i>	334.4166	NA	NA	NA
	Fluorescence	<i>sTDA</i>	467.7869	(14740.410006, 9032.887377, 100718.986812)	(0.1184042055, 0.0725578090)	(0,17,255)
		<i>sTD-DFT</i>	484.4166	(18425.190376, 7436.271551, 116742.366855)	(0.1292054395, 0.0521463667)	(0,2,255)

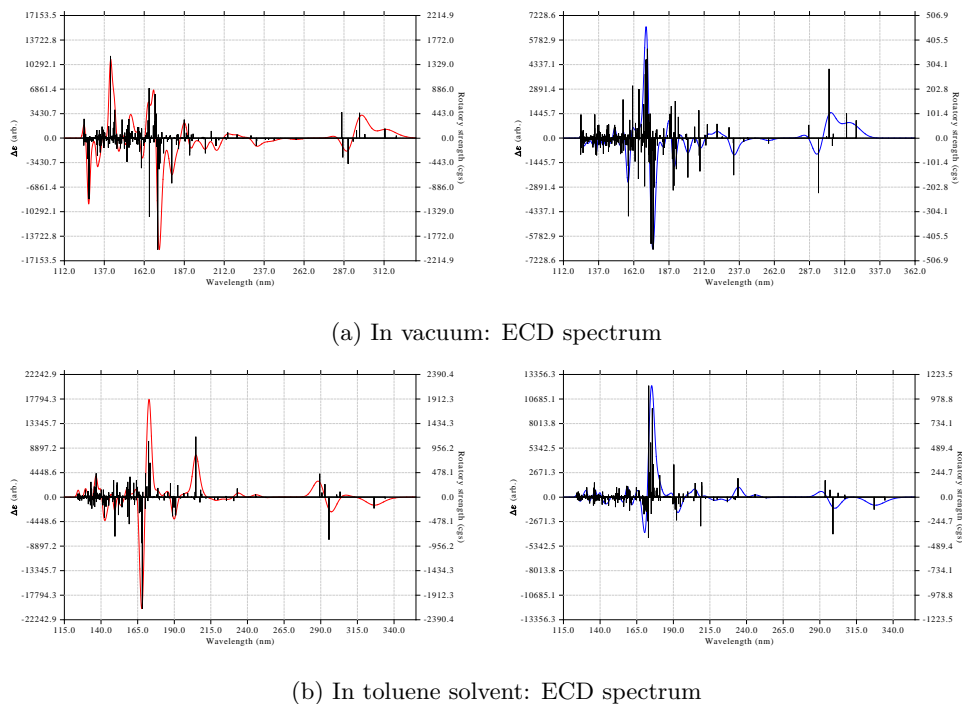
- Φ_{PF} is the prompt fluorescence quantum yield (efficiency of the singlet state emitting light).

The non-radiative decay rate (k_{nr}) can be calculated as:

$$k_{nr} = \frac{1 - f_{12}}{\tau}. \quad (2)$$

Because we don't have spin-orbit coupling (SOC) data, we can estimate k_{rISC} using the *energy gap law* and the *singlet-triplet energy gap* (ΔE_{ST}). A common approximation is:

$$k_{rISC} \approx A \cdot \exp\left(-\frac{\Delta E_{ST}}{k_B T}\right), \quad (3)$$



(a) In vacuum: ECD spectrum

(b) In toluene solvent: ECD spectrum

Figure S. 22 : Electronic Circular Dichroism (ECD) spectra of DMAC-DPS: solvent and method dependence. Panels show the simulated ECD spectra in vacuum and toluene, calculated with *sTDA* (top) and *sTD-DFT* (bottom) methods. The ECD spectra of DMAC-DPS exhibit a complex pattern of positive and negative bands, suggesting a non-trivial chiral contribution from the DMAC and DPS units.

Table S. 8 : Colorimetric properties of PSPCz: wavelength maxima and CIE coordinates. This table summarizes the key colorimetric properties of PSPCz, including the wavelengths of maximum absorption and emission, CIE 1931 color space coordinates (X, Y, Z and x, y), and approximate sRGB color representation. The calculated emission color of PSPCz is relatively stable upon solvation, remaining in the deep blue region, but its low Y value indicates non-visible emission.

		Properties λ_{max} (nm)		(X, Y, Z)	(x, y)	(R,G,B)
In vacuum	<i>UV-vis</i> absorption	<i>sTDA</i>	322.0837	NA	NA	NA
		<i>sTD-DFT</i>	328.3031	NA	NA	NA
	Fluorescence	<i>sTDA</i>	383.5435	(1128.692294, 32.129669, 5329.907469)	(0.1738929817, 0.0049500860)	(45,0,255)
		<i>sTD-DFT</i>	389.3245	(1999.605911, 56.421174, 9460.655116)	(0.1736269071, 0.0048990823)	(45,0,255)
In toluene solvent	<i>UV-vis</i> absorption	<i>sTDA</i>	321.2585	NA	NA	NA
		<i>sTD-DFT</i>	327.2637	NA	NA	NA
	Fluorescence	<i>sTDA</i>	385.6133	(1605.299604, 45.568603, 7585.211526)	(0.1738074649, 0.0049337602)	(45,0,255)
		<i>sTD-DFT</i>	385.6133	(1605.299604, 45.568603, 7585.211526)	(0.1738074649, 0.0049337602)	(45,0,255)

where,

- A is a pre-exponential factor (typically assumed to be $10^6 - 10^9 \text{ s}^{-1}$ for organic molecules);
- ΔE_{ST} is the singlet-triplet energy gap (in eV);
- k_B is the Boltzmann constant ($8.617 \times 10^{-5} \text{ eV K}^{-1}$);
- T is the temperature (in Kelvin, typically 300 K for room temperature).

For simplicity, we assume $A = 1 \times 10^7 \text{ s}^{-1}$ and $\Phi_{PF} \approx 1$ (100%).

We also assume that k_{ISC} is similar to k_{rISC} or slightly larger, depending on the molecule. For simplicity, we assume:

$$k_{ISC} \approx 10 \cdot k_{rISC}. \quad (4)$$

S.5 Details on the computational resources

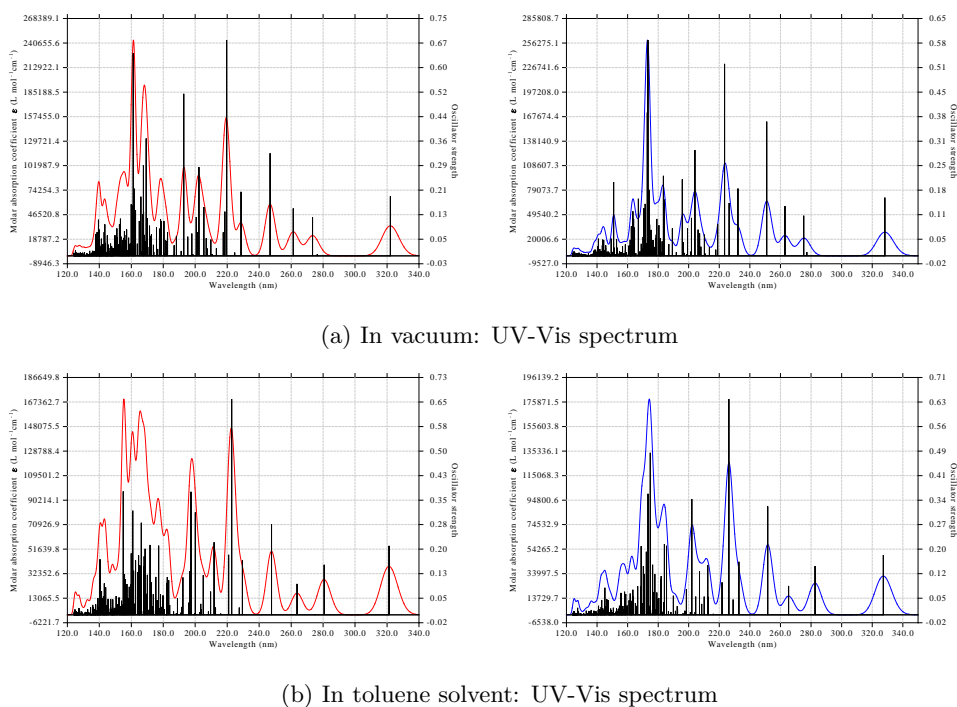


Figure S. 23 : UV-Vis absorption spectra of PSpCz: solvent and method dependence. Panels show the simulated UV-Vis absorption spectra in vacuum and toluene, calculated with *s*TDA (top) and *s*TD-DFT (bottom) methods. The absorption spectra of PSpCz show a relatively weak solvent dependence, suggesting that the ground state is not significantly affected by the surrounding environment.

Table S. 9 : Colorimetric properties of 4CzIPN: wavelength maxima and CIE coordinates. This table summarizes the key colorimetric properties of 4CzIPN, including the wavelengths of maximum absorption and emission, CIE 1931 color space coordinates (*X*, *Y*, *Z* and *x*, *y*), and approximate sRGB color representation. The predicted fluorescence color of 4CzIPN is blue-green, with a slight shift towards green in toluene, providing some indication of solvent-dependent color tunability.

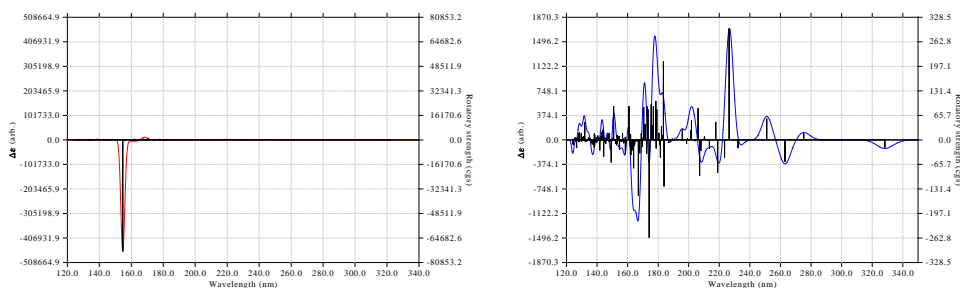
		Properties λ_{max} (nm)		(<i>X</i> , <i>Y</i> , <i>Z</i>)	(<i>x</i> , <i>y</i>)	(<i>R</i> , <i>G</i> , <i>B</i>)
In vacuum	UV-vis absorption	<i>s</i> TDA	375.9277	(622.080647, 17.897209, 2933.099378)	(0.1741022112, 0.0050089062)	(46,0,255)
		<i>s</i> TD-DFT	379.3349	(860.079598, 24.551477, 4060.359190)	(0.1739294825, 0.0049649192)	(46,0,255)
	Fluorescence	<i>s</i> TDA	499.9663	(6585.587764, 172561.782844, 143421.052287)	(0.0204160956, 0.5349617960)	(0,255,173)
		<i>s</i> TD-DFT	504.2363	(5962.020393, 189341.802208, 104255.474648)	(0.0199026385, 0.6320678542)	(0,255,97)
In toluene solvent	UV-vis absorption	<i>s</i> TDA	382.3646	(1268.308978, 35.989911, 5994.171115)	(0.1737773776, 0.0049311583)	(45,0,255)
		<i>s</i> TD-DFT	385.7148	(1761.979572, 49.710040, 8337.538430)	(0.1736072502, 0.0048979134)	(44,0,255)
	Fluorescence	<i>s</i> TDA	515.9937	(24222.155843, 293583.919714, 52882.972765)	(0.0653435972, 0.7919951265)	(0,255,0)
		<i>s</i> TD-DFT	520.1063	(34912.312986, 302858.762182, 37484.335818)	(0.0930361348, 0.8070736712)	(0,255,0)

This is a rough approximation, as k_{ISC} is often faster than k_{rISC} due to stronger spin-orbit coupling in the ISC process.

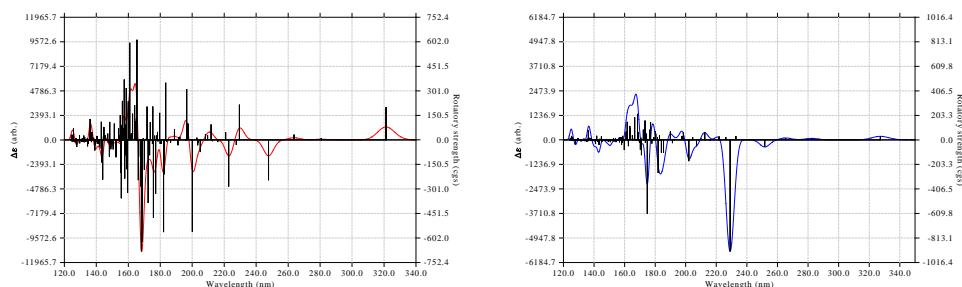
So Tables S. 14 and S. 15 give us the approximated TADF efficiency values.

S.5 Details on the computational resources

Calculations were performed on a high-performance computing cluster consisting of nodes with dual Intel Xeon Gold 6130 CPUs (2.10 GHz), providing a total of 64 physical cores and 128 threads. Each node was equipped with 92 GB of RAM. OpenMP parallelization was employed for the *x*TB, CREST, *s*TDA, and *s*TD-DFT calculations, utilizing 8 threads per job. The TDA calculations were performed with a single thread.



(a) In vacuum: ECD spectrum



(b) In toluene solvent: ECD spectrum

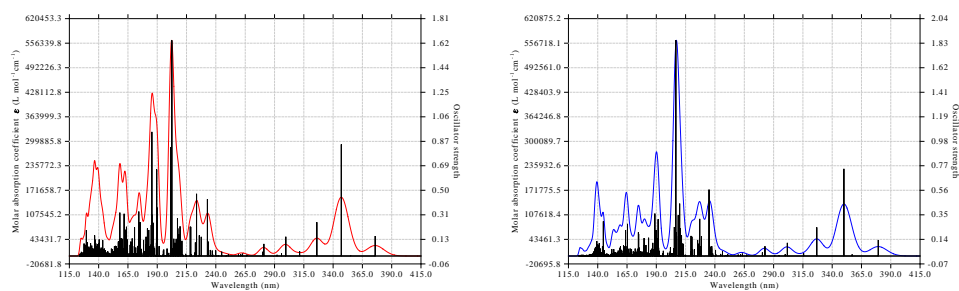
Figure S. 24 : Electronic Circular Dichroism (ECD) spectra of PSpCz: solvent and method dependence. Panels show the simulated ECD spectra in vacuum and toluene, calculated with *sTDA* (top) and *sTD-DFT* (bottom) methods. The ECD spectra of PSpCz exhibit more pronounced chiral features compared to DMAC-TRZ and DMAC-DPS, indicating a less symmetrical structure.

Table S. 10 : Colorimetric properties of Px2BP: wavelength maxima and CIE coordinates. This table summarizes the key colorimetric properties of Px2BP, including the wavelengths of maximum absorption and emission, CIE 1931 color space coordinates (X , Y , Z and x , y), and approximate sRGB color representation. The predicted emission color of Px2BP shifts from green to yellow-green upon solvation, indicating a potential for solvent-dependent color tuning.

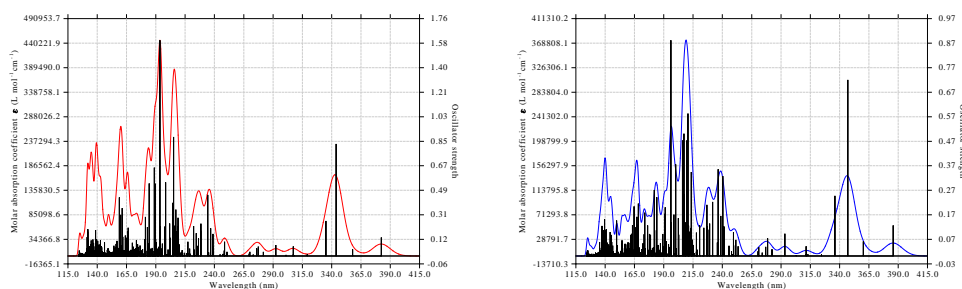
		Properties λ_{max} (nm)		(X, Y, Z)		(x, y)		(R, G, B)	
In vacuum	<i>UV-vis</i> absorption	<i>sTDA</i>	425.9260	(95818.465009, 4481.356426, 470347.964126)	(0.1679117442, 0.0078531040)		(37, 0, 255)		
		<i>sTD-DFT</i>	430.6768	(97190.744443, 5383.702553, 481807.676795)	(0.1663136850, 0.0092126407)		(35, 0, 255)		
	Fluorescence	<i>sTDA</i>	522.9441	(48648.024902, 324507.000941, 32903.858353)	(0.1198053455, 0.7991624209)		(0, 255, 0)		
		<i>sTD-DFT</i>	527.8421	(58938.771173, 299852.961542, 20277.384442)	(0.1554829146, 0.7910245071)		(0, 255, 0)		
In toluene solvent	<i>UV-vis</i> absorption	<i>sTDA</i>	415.8868	(46737.618980, 1647.272467, 226053.988430)	(0.1703024695, 0.0060023291)		(41, 0, 255)		
		<i>sTD-DFT</i>	419.9755	(54038.101184, 2108.192111, 262733.002632)	(0.1694625580, 0.0066112543)		(40, 0, 255)		
	Fluorescence	<i>sTDA</i>	548.1411	(168034.392880, 390818.813123, 1303.913773)	(0.2999772509, 0.6976949847)		(0, 255, 0)		
		<i>sTD-DFT</i>	552.5381	(167125.345717, 336556.849028, 2644.073115)	(0.3300744131, 0.6647035131)		(17, 255, 0)		

Table S. 11 : Colorimetric properties of CzS2: wavelength maxima and CIE coordinates. This table summarizes the key colorimetric properties of CzS2, including the wavelengths of maximum absorption and emission, CIE 1931 color space coordinates (X , Y , Z and x , y), and approximate sRGB color representation. The predicted emission color is deep-blue. The low Y values suggest very little visible emission. The color stays roughly the same, and is more intense when a vacuum is used.

		Properties λ_{max} (nm)		(X, Y, Z)		(x, y)		(R, G, B)	
In vacuum	<i>UV-vis</i> absorption	<i>sTDA</i>	317.7118	NA		NA		NA	
		<i>sTD-DFT</i>	322.9288	NA		NA		NA	
	Fluorescence	<i>sTDA</i>	454.4447	(258349.493337, 39781.120820, 1414339.462559)	(0.1503863654, 0.0232302575)		(13, 0, 255)		
		<i>sTD-DFT</i>	456.7887	(225964.230581, 40319.400005, 1262268.953105)	(0.1478288892, 0.0263775028)		(8, 0, 255)		
In toluene solvent	<i>UV-vis</i> absorption	<i>sTDA</i>	316.4086	NA		NA		NA	
		<i>sTD-DFT</i>	321.3936	NA		NA		NA	
	Fluorescence	<i>sTDA</i>	435.5921	(289686.055708, 16492.097125, 1439309.486008)	(0.1659628228, 0.0094484182)		(35, 0, 255)		
		<i>sTD-DFT</i>	451.2065	(266274.272154, 33986.335253, 1422808.541419)	(0.1545348730, 0.0197243014)		(18, 0, 255)		

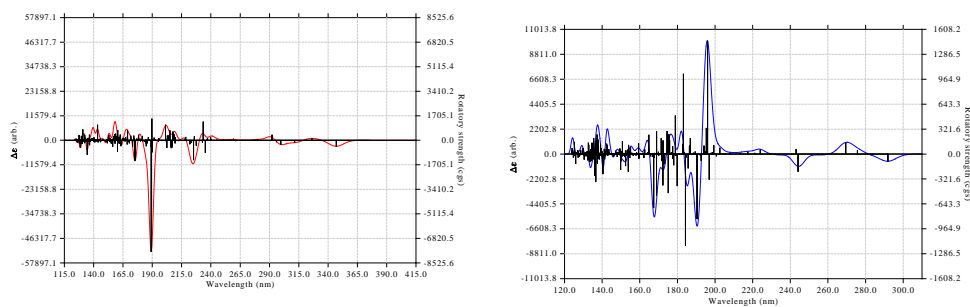


(a) In vacuum: UV-Vis spectrum

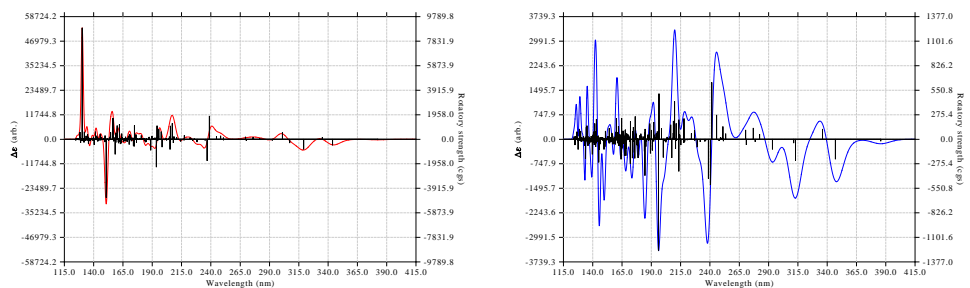


(b) In toluene solvent: UV-Vis spectrum

Figure S. 25 : UV-Vis absorption spectra of 4CzIPN: solvent and method dependence. Panels show the simulated UV-Vis absorption spectra in vacuum and toluene, calculated with *sTDA* (top) and *sTD-DFT* (bottom) methods. The 4CzIPN absorption spectra exhibit a broad absorption band, characteristic of delocalized electronic transitions across the four carbazole units and the IPN core.

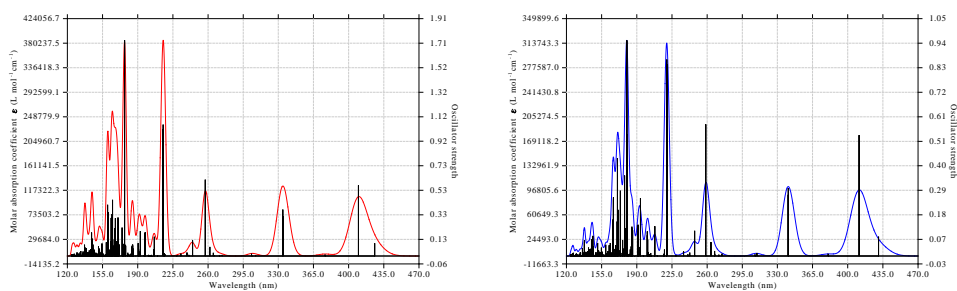


(a) In vacuum: ECD spectrum

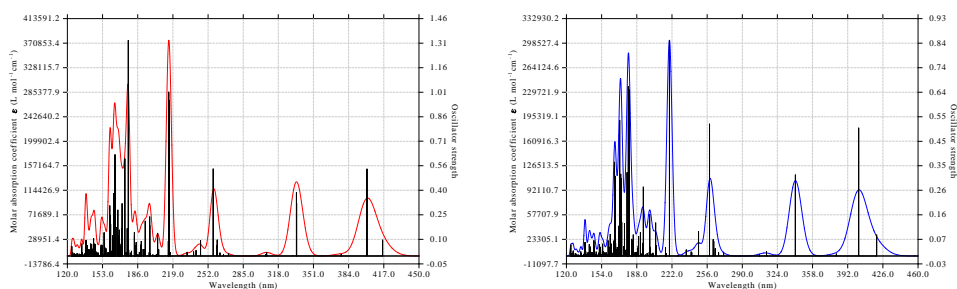


(b) In toluene solvent: ECD spectrum

Figure S. 26 : Electronic Circular Dichroism (ECD) spectra of 4CzIPN: solvent and method dependence. Panels show the simulated ECD spectra in vacuum and toluene, calculated with *sTDA* (top) and *sTD-DFT* (bottom) methods. The ECD spectra of 4CzIPN indicate a relatively symmetrical structure compared to the other molecules, with minimal ECD signals observed.

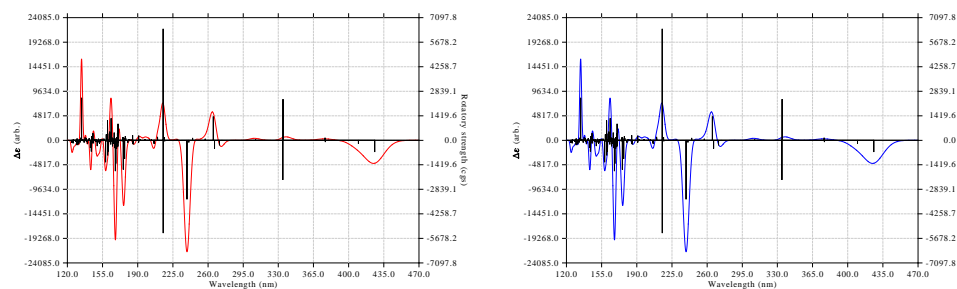


(a) In vacuum: UV-Vis spectrum

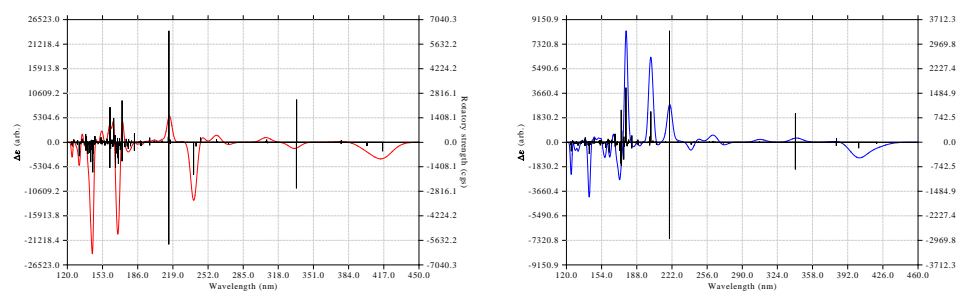


(b) In toluene solvent: UV-Vis spectrum

Figure S. 27 : UV-Vis absorption spectra of Px2BP: solvent and method dependence. Panels show the simulated UV-Vis absorption spectra in vacuum and toluene, calculated with *sTDA* (top) and *sTD-DFT* (bottom) methods. The absorption spectra of Px2BP exhibit a well-defined peak at around 420 nm, indicating a relatively strong absorption in the blue-violet region.

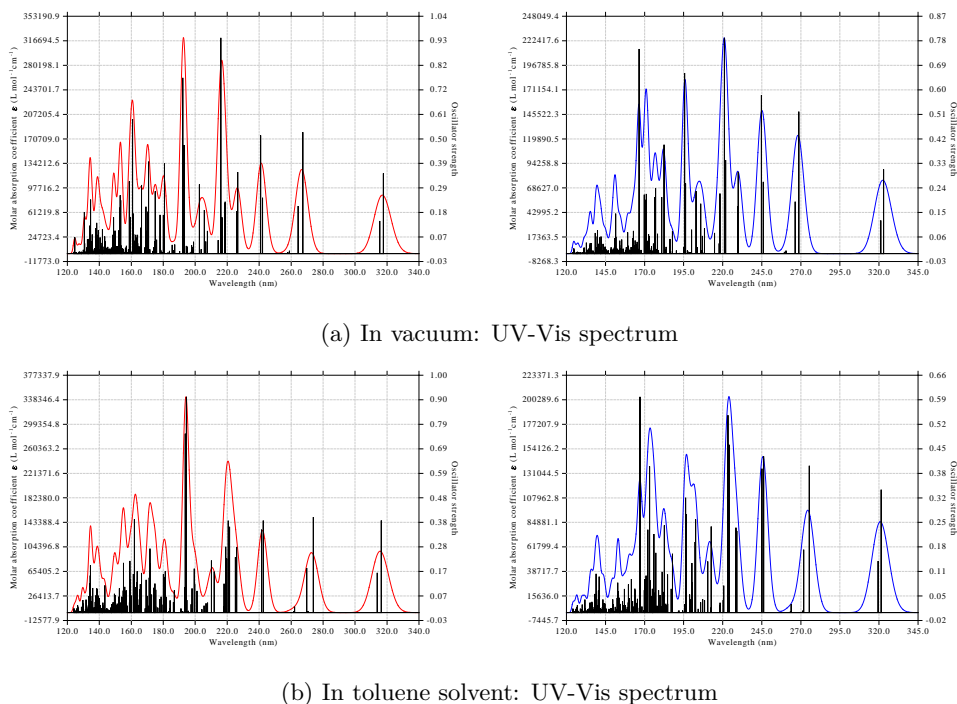


(a) In vacuum: ECD spectrum



(b) In toluene solvent: ECD spectrum

Figure S. 28 : Electronic Circular Dichroism (ECD) spectra of Px2BP: solvent and method dependence. Panels show the simulated ECD spectra in vacuum and toluene, calculated with *sTDA* (top) and *sTD-DFT* (bottom) methods. The ECD spectra of Px2BP display a clear pattern of alternating positive and negative bands, suggesting the presence of chiral conformations.



(a) In vacuum: UV-Vis spectrum

(b) In toluene solvent: UV-Vis spectrum

Figure S. 29 : UV-Vis absorption spectra of CzS2: solvent and method dependence. Panels show the simulated UV-Vis absorption spectra in vacuum and toluene, calculated with *sTDA* (top) and *sTD-DFT* (bottom) methods. The CzS2 absorption spectra exhibit a shoulder peak in the high-energy region, potentially indicating the presence of multiple electronic transitions.

Table S. 12 : Colorimetric properties of 2TCz-DPS: wavelength maxima and CIE coordinates. This table summarizes the key colorimetric properties of 2TCz-DPS, including the wavelengths of maximum absorption and emission, CIE 1931 color space coordinates (X , Y , Z and x , y), and approximate sRGB color representation. There does not appear to be a significant difference as a result of using toluene solvent. The low Y values suggest that 2TCz-DPS has a very minimal color output and weak light.

		Properties		λ_{max} (nm)	(X, Y, Z)	(x, y)	(R, G, B)
In vacuum	UV-vis absorption	<i>sTDA</i>		320.0697	NA	NA	NA
		<i>sTD-DFT</i>		325.5298	NA	NA	NA
	Fluorescence	<i>sTDA</i>		488.7999	(14840.653092, 74056.693543, 184126.398417)	(0.0543566388, 0.2712463472)	(0, 183, 250)
		<i>sTD-DFT</i>		492.6847	(8216.712948, 78345.868615, 133046.205790)	(0.0374152284, 0.3567519750)	(0, 255, 240)
In toluene solvent	UV-vis absorption	<i>sTDA</i>		318.6898	NA	NA	NA
		<i>sTD-DFT</i>		323.6764	NA	NA	NA
	Fluorescence	<i>sTDA</i>		444.8775	(125617.885782, 11316.842073, 646441.372508)	(0.1603545037, 0.0144462437)	(27, 0, 255)
		<i>sTD-DFT</i>		492.3077	(9740.380621, 87144.787118, 153567.584509)	(0.0388910904, 0.3479490097)	(0, 255, 241)

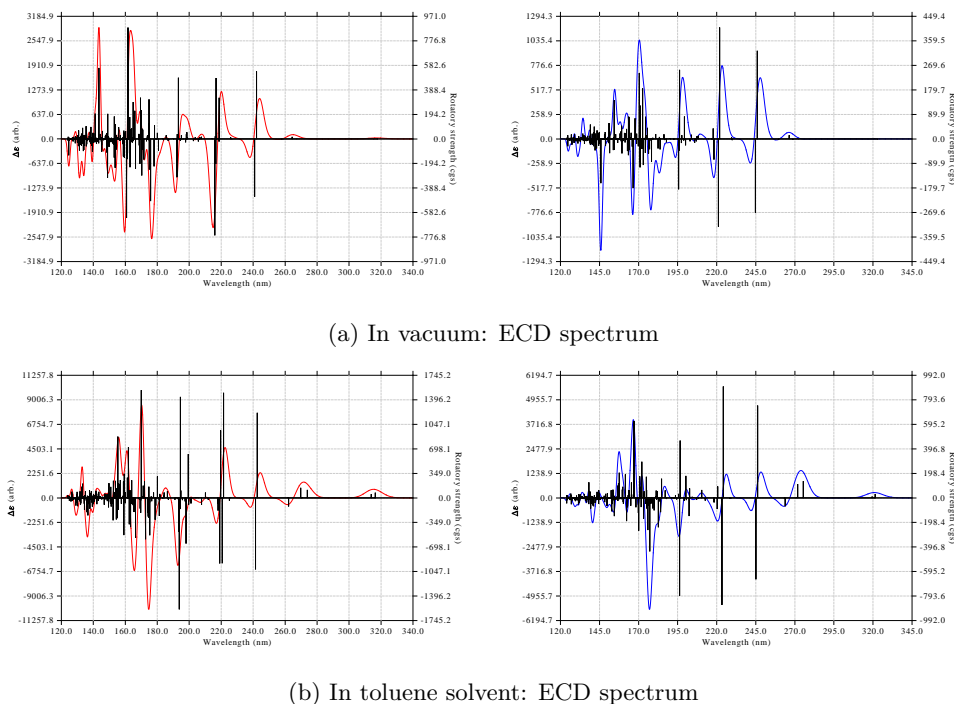
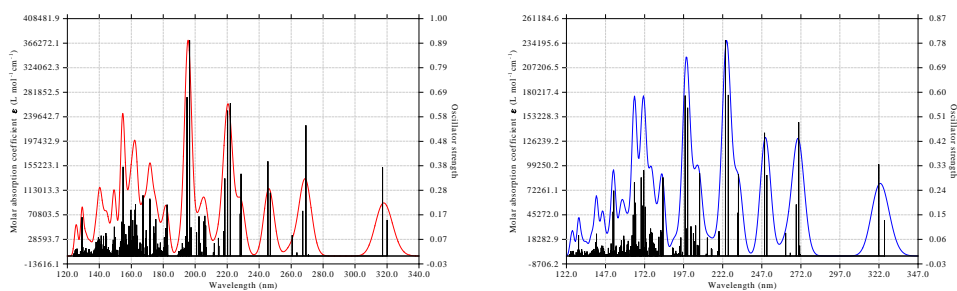


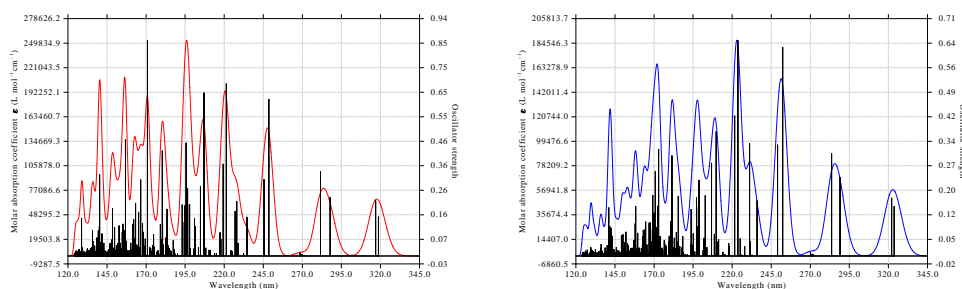
Figure S. 30 : Electronic Circular Dichroism (ECD) spectra of CzS2: solvent and method dependence. Panels show the simulated ECD spectra in vacuum and toluene, calculated with *sTDA* (top) and *sTD-DFT* (bottom) methods. The ECD spectra of CzS2 display a clear pattern of alternating positive and negative bands, suggesting the presence of chiral conformations and strong electronic coupling between the carbazole units.

Table S. 13 : Colorimetric properties of TDBA-DI: wavelength maxima and CIE coordinates. This table summarizes the key colorimetric properties of TDBA-DI, including the wavelengths of maximum absorption and emission, CIE 1931 color space coordinates (X , Y , Z and x , y), and approximate sRGB color representation. The table indicates that TDBA-DI does not have intense visible light in either a vacuum or with toluene solvent. The data suggests that it has a relatively stable spectra under different conditions.

		Properties λ_{max} (nm)		(X , Y , Z)	(x , y)	(R,G,B)
In vacuum	<i>UV-vis</i> absorption	<i>sTDA</i>	347.0120	(2.598548, 0.078137, 12.143628)	(0.1753368927, 0.0052722678)	(47,0,255)
		<i>sTD-DFT</i>	354.0573	(28.284089, 0.848486, 132.320941)	(0.1751841007, 0.0052552933)	(47,0,255)
	Fluorescence	<i>sTDA</i>	407.9651	(24649.659973, 704.505081, 117790.587971)	(0.1722009326, 0.0049216270)	(43,0,255)
		<i>sTD-DFT</i>	415.0671	(62255.917001, 1945.132272, 299424.739677)	(0.1712087506, 0.0053492693)	(42,0,255)
In toluene solvent	<i>UV-vis</i> absorption	<i>sTDA</i>	347.9288	(0.201153, 0.006048, 0.940124)	(0.1753234808, 0.0052709907)	(47,0,255)
		<i>sTD-DFT</i>	353.4456	(24.225603, 0.727063, 113.317577)	(0.1752047508, 0.0052582725)	(47,0,255)
	Fluorescence	<i>sTDA</i>	416.2007	(3197.424834, 101.075516, 15390.166478)	(0.1710889740, 0.0054083856)	(42,0,255)
		<i>sTD-DFT</i>	417.0407	(75059.780932, 2429.076930, 361728.702965)	(0.1708943076, 0.0055304640)	(42,0,255)

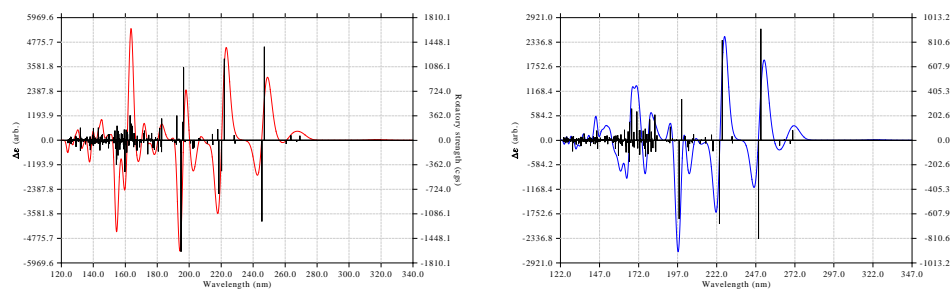


(a) In vacuum: UV-Vis spectrum

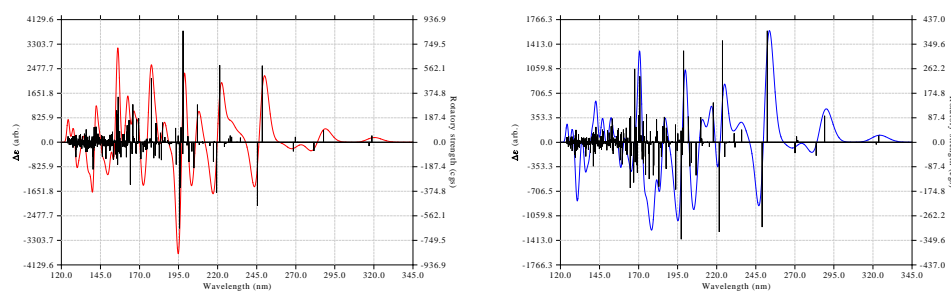


(b) In toluene solvent: UV-Vis spectrum

Figure S. 31 : UV-Vis absorption spectra of 2TCz-DPS: solvent and method dependence. Panels show the simulated UV-Vis absorption spectra in vacuum and toluene, calculated with *sTDA* (top) and *sTD-DFT* (bottom) methods. A redshift in the main peak upon solvation is observed using both *sTDA* and *sTD-DFT*.

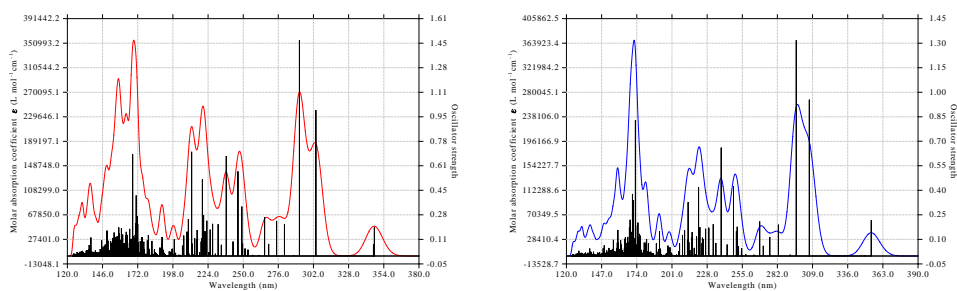


(a) In vacuum: ECD spectrum

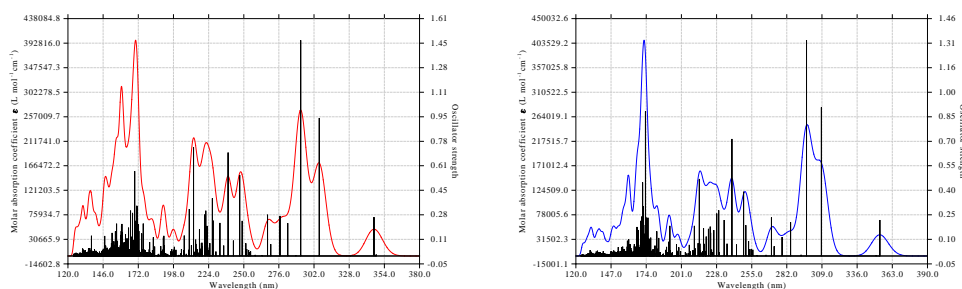


(b) In toluene solvent: ECD spectrum

Figure S. 32 : Electronic Circular Dichroism (ECD) spectra of 2TCz-DPS: solvent and method dependence. Panels show the simulated ECD spectra in vacuum and toluene, calculated with *sTDA* (top) and *sTD-DFT* (bottom) methods. The ECD spectra indicate some changes to planarity occur due to solvation effects.

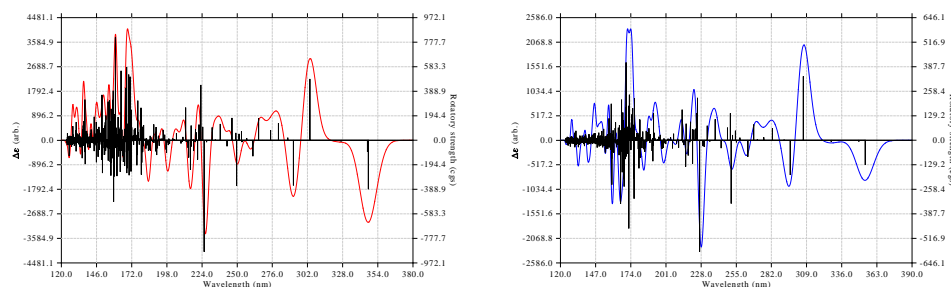


(a) In vacuum: UV-Vis spectrum

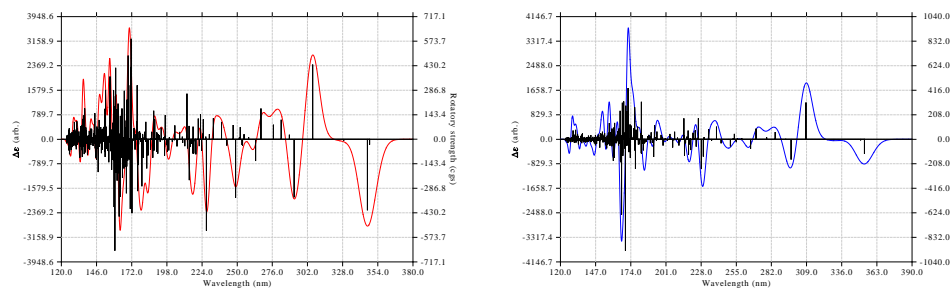


(b) In toluene solvent: UV-Vis spectrum

Figure S. 33 : UV-Vis absorption spectra of TDBA-DI: solvent and method dependence. Panels show the simulated UV-Vis absorption spectra in vacuum and toluene, calculated with *sTDA* (top) and *sTD-DFT* (bottom) methods. Note that there are no real changes when a solvent (toluene) is used to perform the computations. This shows that TDBA-DI is very robust.



(a) In vacuum: ECD spectrum



(b) In toluene solvent: ECD spectrum

Figure S. 34 : Electronic Circular Dichroism (ECD) spectra of TDBA-DI: solvent and method dependence. Panels show the simulated ECD spectra in vacuum and toluene, calculated with *sTDA* (top) and *sTD-DFT* (bottom) methods. The ECD spectra indicate that the optical activity of TDBA-DI is largely unaffected by the solvent environment.

Table S. 14 : Calculated TADF emitters efficiencies in vacuum. Energies are given in eV and radiative lifetimes in ns. Results are shown for both the Tamm-Dancoff Approximation (TDA) and Time Dependent Density Functional Theory (TD-DFT) within a simplified scheme (*s*TDA and *s*TD-DFT, respectively).

Molecule	DMAC-TRZ	DMAC-DPS	PSPCz	4CzIPN	Px2BP	CzS2	2TCz-DPS	TDBA-DI
ΔE_{ST} (<i>s</i> TDA)	0.097000	0.162500	0.120000	0.212000	0.338000	0.040500	0.077500	0.481000
$f_{12}(S_0 - S_1)$ (<i>s</i> TDA)	0.145800	0.020700	0.188900	0.152400	0.103300	0.351200	0.151400	0.194100
τ (ns) (<i>s</i> TDA)	33.044831	148.121242	11.675089	24.590050	39.689274	8.815978	23.659157	12.855337
k_{nr} (<i>s</i> TDA)	25.849731.395222	6.611475.736268	69.472703.817911	34.469226.053696	22.593005.642654	73.593650.710875	35.867719.374620	62.089915.585706
k_{rISC} (<i>s</i> TDA)	234.678.695522	18.626.163407	96.403.129521	2745.117895	20.982474	2.087520.539319	498.952.101859	0.083093
k_{ISC} (<i>s</i> TDA)	2.346786.955220	186.261.634068	964.031.295209	27.451.178949	209.824.738	20.875205.393190	4.989521.018594	0.830932
η_{TADF} (<i>s</i> TDA)	0.008254	0.002733	0.001367	0.000080	0.000001	0.021620	0.012065	0.000000
ΔE_{ST} (<i>s</i> TD-DFT)	0.103000	0.162500	0.072000	0.191000	0.316000	0.026500	0.057500	0.429000
$f_{12}(S_0 - S_1)$ (<i>s</i> TD-DFT)	0.140000	0.019200	0.159100	0.137100	0.085500	0.309500	0.130600	0.219100
τ (ns) (<i>s</i> TD-DFT)	36.015672	174.136364	14.011889	29.114825	52.684333	9.190989	22.719594	11.852942
k_{nr} (<i>s</i> TD-DFT)	23.878493.455873	5.632367.519303	60.013320.674868	29.637822.211727	17.358101.366097	75.127928.690406	38.266528.452045	65.882376.071604
k_{rISC} (<i>s</i> TD-DFT)	186.070.798829	18.626.163407	617.240.876844	6.185.076174	49.140547	3.587733.081291	1.081542.693405	0.621049
k_{ISC} (<i>s</i> TD-DFT)	1.860707.988290	186.261.634068	6.172408.768436	61.850.761741	491.405465	35.877330.812907	10.815426.934046	6.210489
η_{TADF} (<i>s</i> TD-DFT)	0.007177	0.003191	0.009240	0.000208	0.000003	0.031308	0.021560	0.000000

Table S. 15 : Calculated TADF emitters efficiencies in toluene solvent. Energies are given in eV and radiative lifetimes in ns. Results are shown for both the Tamm-Dancoff Approximation (TDA) and Time Dependent Density Functional Theory (TD-DFT) within a simplified scheme (sTDA and sTD-DFT, respectively).

Molecule	DMAC-TRZ	DMAC-DPS	PSPCz	4CzIPN	Px2BP	CzS2	2TCz-DPS	TDBA-DI
ΔE_{ST} (sTDA)	0.080 000	0.242 000	0.134 000	0.217 000	0.320 000	0.232 500	0.465 000	0.458 000
$f_{12}(S_0 - S_1)$ (sTDA)	0.065 600	0.033 500	0.212 100	0.137 500	0.100 000	0.389 000	0.156 400	0.010 600
τ (ns) (sTDA)	73.042 835	91.525 663	10.713 852	27.722 247	41.770 622	8.041 629	23.268 278	243.665 284
k_{nr} (sTDA)	12 792 493.618 432	10 559 879.778 070	73 540 308.516 424	31 112 196.221 094	21 546 243.829 253	75 979 632.232 784	36 255 368.363 384	4 060 488.156 321
k_{rISC} (sTDA)	452 960.941 838	860.168 995	56 092.108 407	2 262.376 068	42.096 212	1 242.157 224	0.154 295	0.202 278
k_{ISC} (sTDA)	4 529 609.418 382	8 601.689 945	560 921.084 065	22 623.760 680	420.962 122	12 421.572 238	1.542 955	2.022 776
η_{TADF} (sTDA)	0.025 483	0.000 081	0.000 756	0.000 073	0.000 002	0.000 016	0.000 000	0.000 000
ΔE_{ST} (sTD-DFT)	0.108 000	0.267 000	0.134 000	0.198 000	0.302 000	0.134 000	0.196 500	0.421 000
$f_{12}(S_0 - S_1)$ (sTD-DFT)	0.063 600	0.033 100	0.178 100	0.124 800	0.083 800	0.339 900	0.149 500	0.220 800
τ (ns) (sTD-DFT)	77.243 232	99.113 076	12.517 078	32.486 201	54.618 954	8.979 713	24.304 962	11.809 206
k_{nr} (sTD-DFT)	12 122 744.968 175	9 755 524.104 466	65 662 290.130 933	26 932 378.701 461	16 774 396.600 655	73 510 144.072 858	34 992 854.935 097	65 982 421.544 256
k_{rISC} (sTD-DFT)	153 349.378 188	327.041 428	56 092.108 407	4 717.917 787	84.455 775	56 092.108 407	4 999.760 828	0.846 291
k_{ISC} (sTD-DFT)	1 533 493.781 879	3 270.414 276	560 921.084 065	47 179.177 871	844.557 748	560 921.084 065	49 997.608 276	8.462 910
η_{TADF} (sTD-DFT)	0.011 105	0.000 034	0.000 846	0.000 175	0.000 005	0.000 757	0.000 143	0.000 000